

Synchrotrons and accumulators for high-intensity proton beams

Jie Wei*

*Collider-Accelerator Department, Brookhaven National Laboratory,
Upton, New York 11973, USA
and Spallation Neutron Source Project, Oak Ridge National Laboratory,
Oak Ridge, Tennessee 37831, USA*

(Published 4 November 2003)

During the past five decades, the development of accelerator science and technology sustained exponential growth in the energy and intensity of proton beams. Combined with an increasing repetition rate, the use of high-powered proton beams has extended from nuclear and high-energy physics to modern applications, including spallation-neutron production, kaon factories, nuclear transmutation, neutrino-factory drivers, and, in future, energy amplification and muon-collider drivers. This paper surveys the design and operational experience of existing and proposed proton facilities, summarizes physical and engineering issues limiting the efficiency of high-intensity synchrotrons and accumulators, reviews beam-dynamics topics pertaining to high-intensity performance, and discusses future applications and outlook.

CONTENTS

I. Introduction	1383	3. Kinematic tune shift	1408
II. Low-Loss Design Philosophy	1386	4. Magnetic imperfections	1409
III. Accelerator System: Design and Technical Issues	1387	5. Magnetic fringe field	1409
A. Lattice	1388	6. Electron cloud	1409
1. Layout and function	1388	7. Resonance effects and correction	1410
2. FODO arc	1388	B. Beam-loss mechanisms	1410
3. Dispersion suppressor	1389	1. Controlled beam loss	1410
4. Transition-energy manipulation	1389	2. Uncontrolled beam loss	1411
5. Working point	1390	3. Resonance-loss model	1411
6. Acceptance	1391	C. Collective effects	1412
B. Beam scraping and collimation	1393	1. Space charge and beam halo	1412
1. Scraping, collimation, and collection	1393	2. Coupling impedance	1413
2. Scrapers and collimators	1394	3. Instabilities	1415
C. Injection	1395	D. Electron-cloud effects	1416
1. Single-turn injection	1395	1. Electron generation	1416
2. Multiturn proton injection	1395	2. Electron neutralization and the Pacman effect	1419
3. Multiturn charge-exchange injection	1396	3. Electron-proton instabilities	1419
4. Phase-space painting	1397	4. Preventive measures	1420
D. Acceleration	1398	E. Intrabeam scattering	1421
1. Radio-frequency capture	1398	F. Computer simulation codes	1422
2. Ramping, power supply, and rf system	1399	V. Future Applications and Developments	1422
3. Transition crossing	1399	VI. Conclusions and Discussion	1423
E. Extraction	1400	Acknowledgments	1424
F. Transport lines	1401	Abbreviations and Acronyms	1425
G. Magnet system and field-error compensation	1402	List of Symbols	1426
1. Magnet system	1402	References	1427
2. Magnet transfer function	1402		
3. Imperfections in the magnetic field	1403		
4. Magnetic fringe field	1403		
5. Magnetic interference	1404		
6. Correction system	1404		
H. Vacuum chamber and shielding	1404		
I. Beam diagnostics and machine protection	1405		
IV. Beam Dynamics: Intensity-Limiting Mechanisms	1406		
A. Transverse tune shifts and resonances	1407		
1. Space-charge tune shift	1407		
2. Chromatic tune shift	1408		

I. INTRODUCTION

Synchrotrons are circular accelerators in which charged particles are constrained to move in fixed orbits by magnets whose fields vary in time such that the radius of curvature remains constant as the particles gain energy. The particles are successively accelerated by alternating electric fields produced by resonating radio-frequency (rf) cavities (Oliphant, 1943; Oliphant *et al.*, 1947). The particle's motion is stabilized longitudinally by the rf electric field, so that particles oscillate around the synchronous phase (McMillan, 1945; Veksler, 1945). In the original, weak-focusing (also known as constant-gradient) machines, transverse stability is provided by a

*Electronic address: jwei@bnl.gov

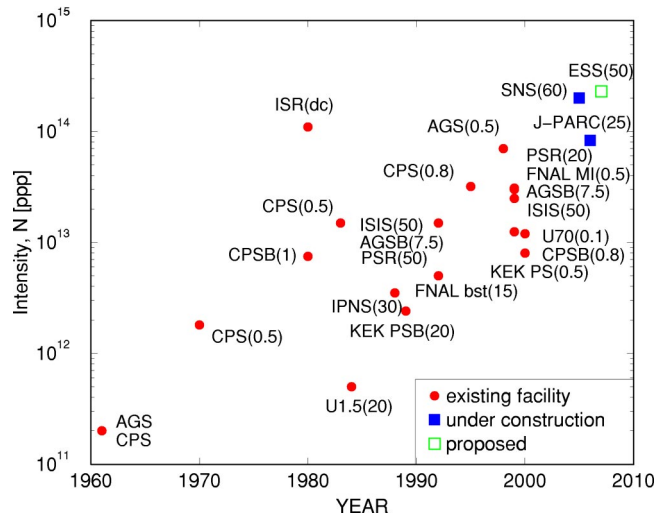


FIG. 1. (Color in online edition) Evolution of proton-beam intensity (particles per pulse) in some synchrotrons and accumulators (Sec. I). The parentheses indicate repetition rate in Hz.

magnetic field that is vertically focusing and by natural centrifugal forces, which provide radial stability. Modern synchrotrons use alternating-gradient quadrupole magnets to ensure strong focusing in both transverse directions (Christofilos, 1950; Courant *et al.*, 1952).

During the five decades since the invention of the synchrotron and the discovery of the principle of alternating-gradient focusing, the development of accelerator science and technology has sustained exponential growth in the energy and intensity of the proton beam. Similar to the “Livingston chart” that records the energy evolution achieved with accelerators at the high-energy frontier (Livingston and Blewett, 1962; Chao and Tigner, 1998), Fig. 1 shows the intensity evolution attained with accelerators at the high-intensity frontier. With the increasing repetition rate of the acceleration cycle, the use of high-powered proton beams has extended from nuclear and high-energy physics to modern applications, including spallation-neutron production, kaon factories, nuclear transmutation, neutrino-factory drivers, and, in future, to energy amplification and muon-collider drivers.

Several factors have facilitated the use of synchrotrons and accumulators for high-intensity beams. One is the development of intense, high-duty-factor, low-emittance sources of H^- and H^+ ions (Hiskes *et al.*, 1976; Allan and Wong, 1978; Leung, 1998). H^- beams, stripped of their electrons upon injection into the synchrotron, allow protons to accumulate, thereby increasing the beam’s intensity up to several thousand fold in the synchrotron ring. A second factor is the invention of the radio-frequency quadrupole (RFQ) linear accelerator, replacing the Cockcroft-Walton accelerator as the preaccelerator. The RFQ combines focusing and acceleration while preserving emittance at a low energy where repulsive intraparticle space-charge forces tend to cause filamentation and dilution of the phase space (Kapchinskii and Teplyakov, 1970). A third factor is the

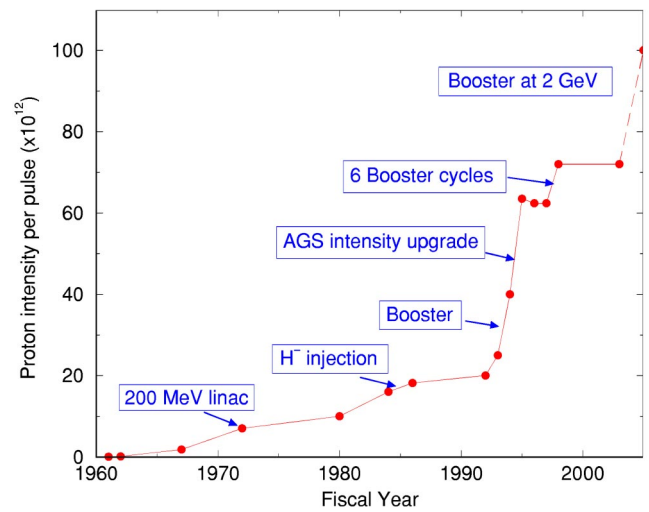


FIG. 2. (Color in online edition) Evolution of proton-beam intensity (particles per pulse) in the Alternating Gradient Synchrotron at the Brookhaven National Laboratory (Sec. I). Figure courtesy T. Roser.

development of linear-accelerator technology. One example is the use of permanent magnet quadrupoles that reduce the dimension of drift-tube accelerators, thereby increasing the accelerating gradient and efficiency. Another example is the advent of superconducting technology for accelerating cavities, which lowers operational costs while increasing the machine’s reliability (Bardeen, Cooper, and Schrieffer, 1957; Proch, 1998).

To illustrate the continuous effort towards attaining high-intensity beams, Fig. 2 shows the evolution of proton intensity in the Alternating Gradient Synchrotron at the Brookhaven National Laboratory (Sluyters, 1990; Roser, 2001). A major increase in intensity was achieved when (1) the injection energy was increased by upgrading the linear accelerator (linac) from 50 to 200 MeV; (2) H^- injection replaced proton injection; (3) the AGS booster was constructed to raise the injection energy to 1.9 GeV; (4) up to six booster pulses were transferred to a single AGS pulse; (5) upgrades were made to increase the linac’s current, the ring acceleration rate, and the repetition rate; (6) nonlinear resonances were corrected in the booster; and, (7) feedback systems and dilution cavities were installed to suppress instabilities (Prelec, 1989; Weng, 1990; Alessi and Prelec, 1991).

Traditionally, protons are preaccelerated by linear accelerators (linacs) at low energies to accommodate large variations in velocity and frequency and to overcome space-charge effects. At higher energies protons are accelerated by circular accelerators (rings). In high-intensity proton applications, the ring also accumulates the beam until it attains a high peak intensity with a pulsed time structure. Particles accelerated in the ring encounter resonances and instabilities that limit the beam’s intensity and power. An accumulator is a simplified synchrotron with neither particle acceleration nor magnet ramping. Thus it shortens the time that the beam spends in the ring, eliminates variations in the beam’s orbit caused by mismatches in synchronization,

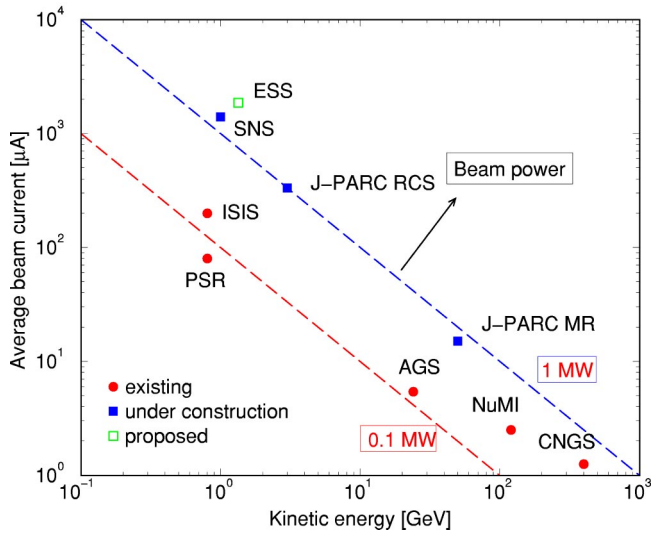


FIG. 3. (Color in online edition) Beam energy, current, and power of some of the world’s high-intensity proton synchrotrons (Sec. V). Beam power in existing high-intensity rings is near 0.1 MW. Beam power designed for new-generation facilities is near 1 MW.

avoids reductions in the stable longitudinal phase-space area during acceleration, and lowers the power needed for the magnet system. Depending on the application, a high-intensity accelerator facility usually consists of either a full-energy linac followed by an accumulator ring (AR) or a partial-energy linac followed by rapid-cycling synchrotrons (RCS’s), both starting with an intense ion source and connected by transport lines. If ultrahigh beam power is needed at relatively low energy with no

restrictions on the beam’s time structure, then the beam must be accelerated by a linear accelerator only.

Figure 3 shows the beam energy, current, and power of some of the world’s high-intensity proton synchrotrons. At present, two major high-intensity proton facilities are under construction: the Spallation Neutron Source (SNS) in the United States, and the Japan Proton Accelerator Research Complex (J-PARC) in Japan. The SNS accelerator complex is based on the concept of an AR. As shown in Fig. 4, it consists of an H^- ion source, an RFQ, a drift-tube linac, a coupled-cavity linac, a superconducting rf linac, and an accumulator ring along with their transport lines. The J-PARC accelerator complex is based on the concept of RCS’s; it consists of a 400-MeV linac, a 3-GeV synchrotron, and a 50-GeV synchrotron along with their transport lines (Fig. 5). The proposed European Spallation Source facility (ESS) uses two vertically stacked accumulator rings to achieve a combined 5-MW beam power (Fig. 6).

This paper summarizes the development of synchrotrons and accumulators for high-intensity protons, emphasizing experiences gained in recent years, current issues in their design and operation, and the outlook for the future. Section II outlines the design philosophy of modern proton synchrotrons and accumulators. Section III discusses physical and technical issues in lattice design, acceptance choice, beam collimation and cleaning, beam injection, ramping and transition crossing, beam extraction, magnet and correction systems, transport lines, and diagnostics. Topics in beam dynamics pertaining to high-intensity performance are reviewed in Sec. IV, including tune spread and resonances, beam-loss mechanisms, space charge, halo development, imped-

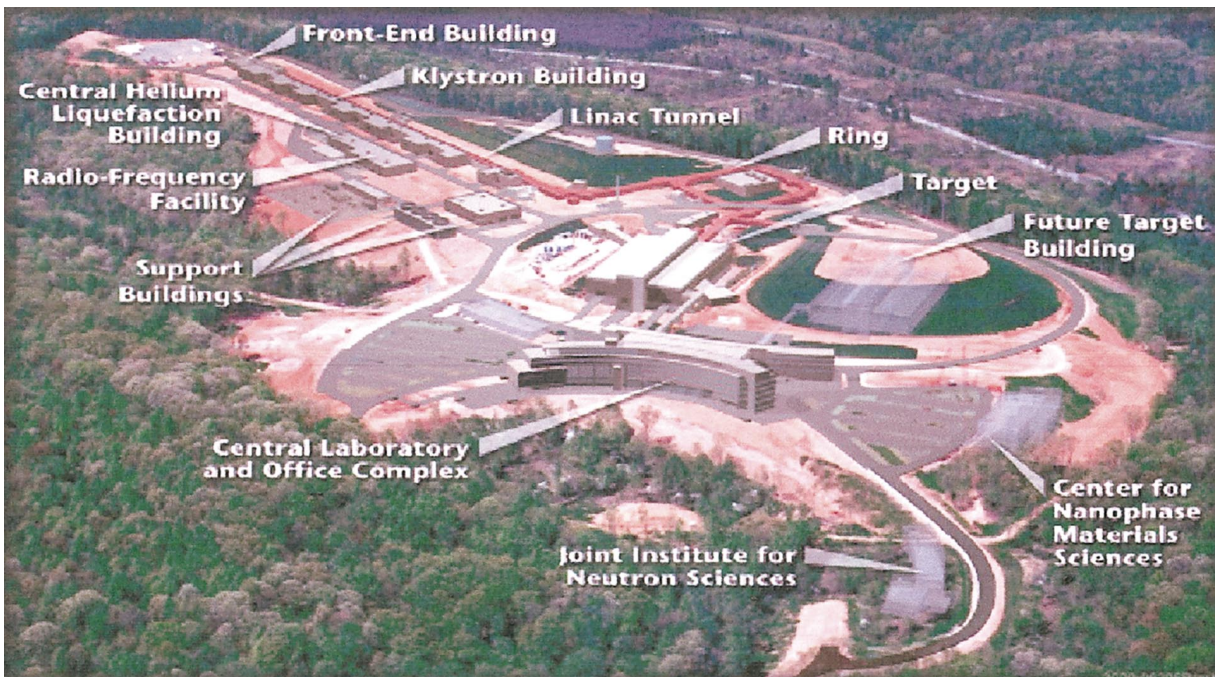


FIG. 4. (Color) Layout of the Spallation Neutron Source. The SNS accelerator complex consists of an H^- ion source, an RFQ, a drift-tube linac, a coupled-cavity linac, a superconducting rf linac, and an accumulator ring, along with their transport lines. The construction began in 1999 (Sec. I). Figure courtesy SNS Project.

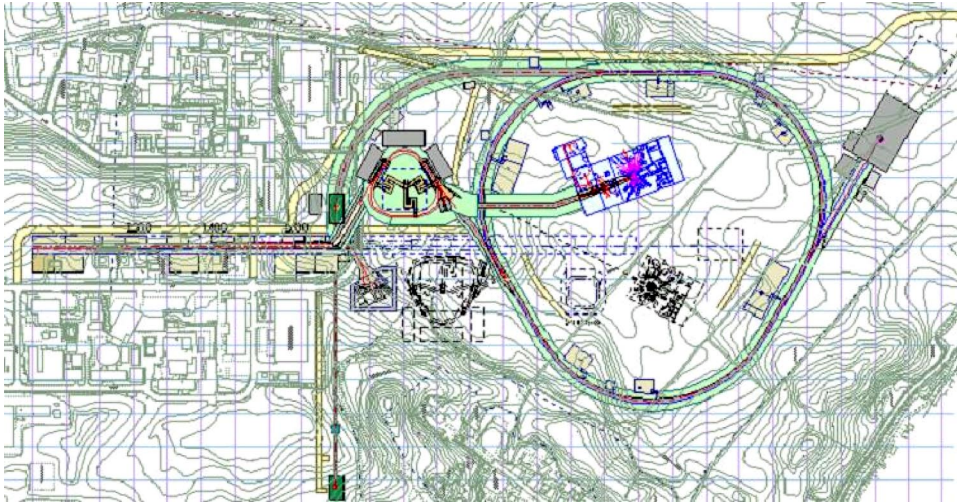


FIG. 5. (Color in online edition) Schematic layout of the J-PARC Project. The J-PARC accelerator complex consists of a 400-MeV linac, a 3-GeV synchrotron, and a 50-GeV synchrotron, along with their transport lines. The construction began in 2001 (Sec. I). Figure courtesy J-PARC Project.

ance and instabilities, electron-cloud effects, and intra-beam scattering. A short survey is given of computer simulation codes used in studying beam dynamics. Section V describes high-intensity applications, as well as accelerator projects, both planned and under construction. The author's conclusions are given in Sec. VI. Note that many of the citations are not to seminal sources, but rather drawn from the author's immediate personal experience. SI (Système International, MKSA) units are used throughout this article.

II. LOW-LOSS DESIGN PHILOSOPHY

The primary concern in designing high-intensity proton facilities is that radioactivation caused by uncon-

trolled beam loss can limit a machine's availability and maintainability. Based on past operational experience, hands-on maintenance (1–2 mSv/h or 100–200 mrem/h at 30 cm from the surface, 4 h after shutdown) demands an average uncontrolled beam loss not exceeding about one watt of beam power per tunnel meter (Wangler, 1998; Mokhov and Chou, 1999). For example, for a ring of 200-m circumference handling a 2-MW beam power, this corresponds to a fractional uncontrolled beam loss of 10^{-4} .

Existing proton synchrotrons have beam losses as high as several tens of percent, mostly occurring when the beam is injected, during its initial capture by the accelerating system, at the start of acceleration ramping, and at the time of transition-energy crossing when the mo-

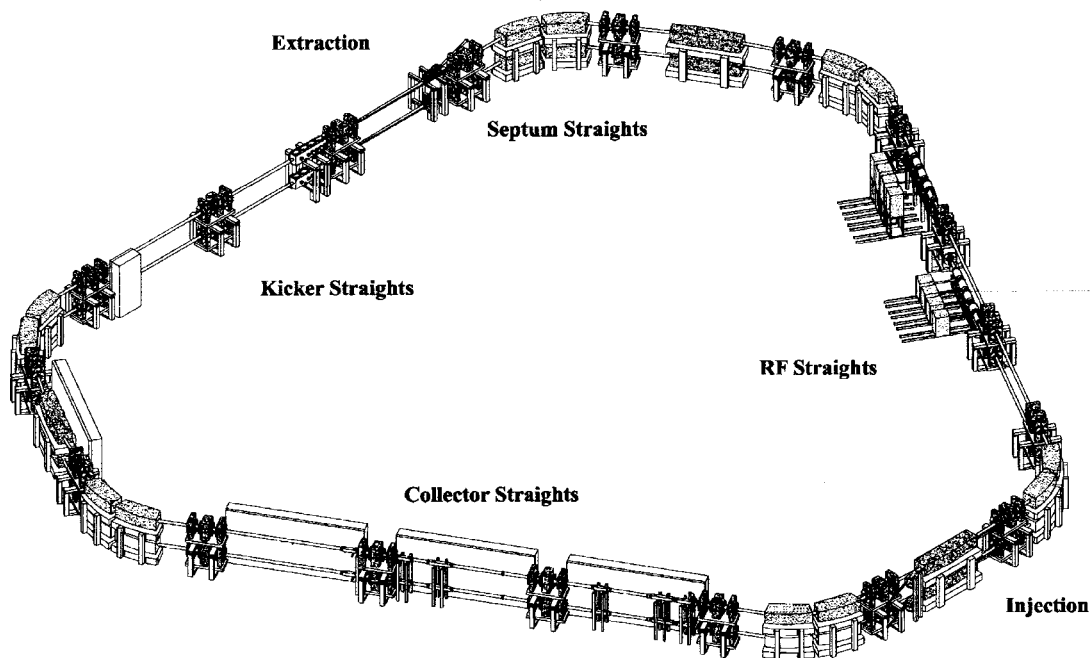


FIG. 6. Schematic layout of the proposed European Spallation Source ring. The ESS accelerator complex consists of two H^- ion sources, a 1.334-GeV linac, and two accumulator rings, along with their transport lines. The rings are vertically stacked to achieve a combined 5-MW beam power (Sec. I). Figure courtesy ESS Council.

tion of longitudinal particles is nonadiabatic. Losses also take place through the development of instabilities in either the transverse or longitudinal motion of the particles. Thus far, the lowest fractional beam loss attained was about 3×10^{-3} , achieved at a beam intensity of about 5×10^{13} protons per pulse at the Proton Storage Ring (PSR) accumulator at the Los Alamos National Laboratory (Macek, 1999; Plum *et al.*, 1999). Uncontrolled beam losses usually are attributed to (1) a high space-charge tune shift (0.25 or larger) at injection, resulting in resonance crossing; (2) limited geometric and momentum acceptance; (3) premature H^- and H^0 stripping and injection-foil scattering; (4) large errors in the magnetic field and alignment, and dipole-quadrupole tracking errors during acceleration ramping; (5) instabilities (e.g., head-tail instability, coupled-bunch instability, negative mass and microwave instability, electron-cloud instability); (6) accidental beam loss (such as malfunction of the ion source and linac or misfiring of the extraction kickers); and (7) beam-halo loss during fast extraction.

A low-loss design or upgrade attempts to rectify these problems. The following lists some examples:

- (1) The beam is “painted” in the transverse phase space to keep the space-charge tune shift low (below 0.15), and “painted” in the longitudinal phase space to reduce the peak current and to damp instabilities (Sec. III.C.4).
- (2) A large transverse aperture is designed to contain not only the circulating beam but also the beam halo at the cost of increased magnet size and power supplies, and a large longitudinal acceptance is realized to contain the beam momentum’s halo and tail by optimizing the lattice’s chromatic properties and by using multiharmonic rf systems with large voltages (Secs. III.A and III.A.6).
- (3) The beam’s orbit in the injection region is programmed to avoid hitting the foil excessively, and the magnetic fields at injection are designed to prevent premature stripping of H^- and H^0 (Sec. III.C).
- (4) A moderate main magnet field avoids saturation effects, and shimmed pole tip in both the dipole and quadrupole magnets help compensate for the effects of fringe fields (Sec. III.G).
- (5) To avoid instabilities in the particles’ motion, efforts are made to reduce the coupling impedance caused by the beam environment: vacuum-pipe steps are tapered; the connecting bellows, vacuum ports, and instrumentation ports are shielded; and, the inner surface of the vacuum chamber is coated with material having a low secondary emission rate of electrons to limit the production of an electron cloud (Secs. IV.C.2, IV.C.3, and IV.D).
- (6) The preinjection transport is designed with beam-collimation systems to prevent accidental malfunction of the ion source and linac, and redundancy is built into the extraction system to prevent beam loss upon the accidental misfiring of the extraction kick-

ers (Sec. III.F). Subsequent sections will discuss these design and upgrade issues in detail.

In addition to these measures to minimize beam losses, modern accelerator facilities are designed to localize beam loss to specific shielded regions and are equipped with cleaning and collection capabilities. With a large transverse and momentum aperture, multistage collimation and momentum cleaning can be incorporated. A clean gap between subsequent beam bunches, key to a low-loss beam extraction, is ensured by multistage beam cleaning that includes multistep chopping at low energies and beam-in-gap sweeping with collimator collection at the top energy.

Flexibility and reliability are important aspects that must be addressed early in the design stage. For example, both synchrotrons and accumulators are designed with electromagnets to accommodate variations in the beam’s injection energy; separate dipole and quadrupole magnets are preferred, instead of combined-function magnets, to allow independent orbit steering and focusing adjustment; multifamily power supplies are employed for quadrupole magnets, permitting wide adjustment of the tunes of the transverse motion; programmable orbit bumps are designed to realize different particle distributions via painting; beam scraping and collimation systems are contrived to adjust for the change in beam tail and halo; and, finally, engineering design considers redundancy, radiation resistance, “active maintenance” capability (e.g., use of quick-release flanges, quick-release water fittings, movable shielding, kinematic mounts for prealignment of machine components, and miniature fiber-optic cameras for viewing vacuum-component damage in a machine maintenance period), and “hot” spares (spare devices that can be used without reinstallation), especially for areas of high radiation and activation.

III. ACCELERATOR SYSTEM: DESIGN AND TECHNICAL ISSUES

Synchrotrons and accumulators may be divided into various systems according to their beam-handling functions: injection, capture and acceleration, extraction, collimation, and transport. These systems are integrated by the “lattice” magnets, usually symmetrically arranged to alleviate the lower-order resonances.

Figure 7 illustrates the layout of the Spallation Neutron Source accumulator—a typical ring for high-intensity applications (Wei, Abell, *et al.*, 2000). Along the 248-m machine’s circumference, the guiding dipole and focusing quadrupole magnets are arranged to form a fourfold symmetric lattice. The four straight sections are designed, in turn, for injection, collimation, the radio-frequency (rf) system, and extraction. Beam diagnostics and correction systems are distributed along the machine. The transport lines connect the accumulator ring with the injecting linac and the target for neutron-spallation experiments and applications.

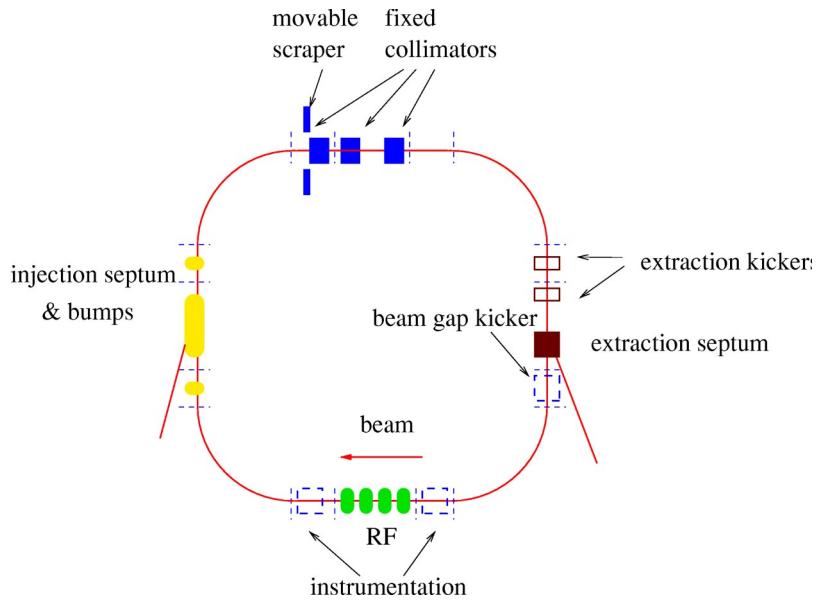


FIG. 7. (Color in online edition) Schematic layout of the Spallation Neutron Source (SNS) accumulator ring. The ring circumference is 248 m. The four straight sections are designed for injection, collimation, the rf system, and extraction (Sec. II).

Most of the contents in this section apply to both synchrotrons and accumulators. Exceptions are subsections on ramping and transition crossing that apply only to synchrotrons where the beam is accelerated.

A. Lattice

1. Layout and function

The backbone of a synchrotron is its lattice, the periodic magnetic structure encountered by the circulating beam. Lattices of high periodicity are preferred to reduce the impact of lower-order resonances on the transverse motion of particles excited by magnetic imperfections. On the other hand, for a ring of moderate circumference (typically several hundred meters), high-periodicity lattices also imply a lack of long, uninterrupted straight sections to accommodate dedicated functions. As a compromise, modern synchrotrons for high-intensity protons often have a lattice periodicity from 2 to 4.

The machine's circumference largely is determined by the space required to accommodate injection, collimation, rf, extraction, diagnostics, and possible upgrades. A large circumference also entails fewer injection turns, reduced foil scattering for H^- injection, and a lower particle density for better beam stability. The details of the lattice design are directly linked to the choice of injection, cleaning, and extraction schemes, to be discussed in Secs. III.C, III.B, and III.E.

The traditional choice is the focusing-drift-defocusing-drift (FODO) structure and its variations. FODO structures require modest quadrupole gradients, and the alternating amplitudes of the transverse beam easily accommodate magnetic-correction systems acting selectively on the two transverse directions. A FODO lattice also is relatively insensitive to errors in quadrupole tuning. Figure 8 shows one superperiod of the J-PARC 3-GeV synchrotron consisting of FODO structures (Machida, 1999; J-PARC, 2002). The lattice superperi-

odicity is 3. The split quadrupole creates a high-dispersion drift section for scraping the momentum halo and for chromatic adjustments.

A lattice consisting of doublets/triplets has the advantage of encompassing long, uninterrupted straight sections for flexible injection and optimal collimation. Synchrotrons of this structure also have vacuum chambers with fewer segments and joints (Boardman, 1982; ESS, 2002). Figure 9 shows one superperiod of the European Spallation Source's (ESS's) accumulator ring consisting of triplet structures. The lattice superperiodicity is 3 (ESS, 2002).

The Spallation Neutron Source's accumulator ring adopts a hybrid structure with FODO arcs and doublet straights. It combines the FODO structure's robustness and ease of correction with the flexibility of the doublet structure's long drift (12.5 m; Wei, Abell, *et al.*, 2000). The arcs and straights are optically matched to ensure maximum transverse acceptance. Each dipole is centered between two quadrupoles to maximize the vertical acceptance of the dipoles. Figure 10 shows one superperiod of the SNS ring consisting of the hybrid structure. The lattice superperiodicity is 4 (Wei, Abell, *et al.*, 2000).

2. FODO arc

The commonest arc section is a separated-function FODO structure. The minimum cell length L_c usually is determined by the drift space needed to accommodate the magnets (dipole, quadrupole, sextupole, and correctors) and the services and instruments (vacuum ports, bellows, joints, and beam-position monitors). The bending angle ϕ_c per FODO cell usually is determined by the ring's geometry and is often a compromise between the minimum number of arc cells and the maximum tolerable dispersion. As a design guideline, a low β_{\perp}^+ generally is preferred to maximize betatron acceptance, a low dispersion to maximize momentum acceptance, and a low $\beta_{\perp}^+/\beta_{\perp}^-$ ratio to reduce the possibility of generating

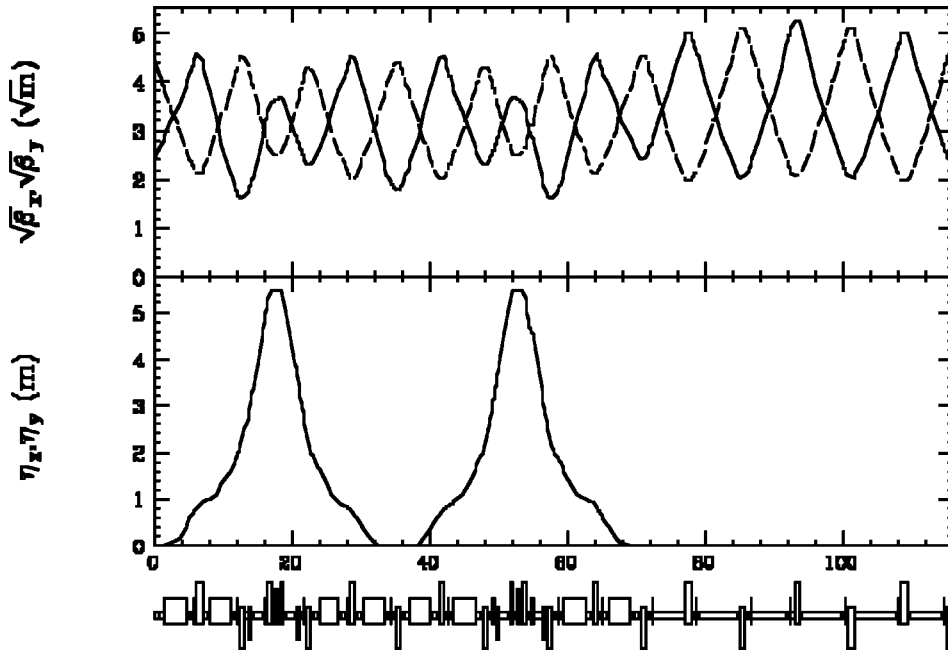


FIG. 8. J-PARC Project 3-GeV ring lattice superperiod of FODO structure. The lattice periodicity is 3. The split quadrupole creates a high-dispersion drift for momentum halo scraping and chromatic adjustment. Along the indicated beam line are dipoles (centered square boxes), focusing quadrupoles (upper bars), and defocusing quadrupoles (lower bars) (Sec. III.A.1). Figure courtesy S. Machida.

a beam halo (Wei, Fedotov, and Papaphilippou, 2001). In the thin-lens approximation, these quantities are expressed as

$$\frac{\beta_{\perp}^{+}}{L_c} = \frac{1 + \sin \frac{\mu_c}{2}}{\sin \mu_c}, \quad (1)$$

$$\frac{\beta_{\perp}^{-}}{\beta_{\perp}^{+}} = \frac{1 + \sin \frac{\mu_c}{2}}{1 - \sin \frac{\mu_c}{2}}, \quad (2)$$

$$\frac{D^{+}}{L_c} = \frac{\phi_c \left(1 + \frac{1}{2} \sin \frac{\mu_c}{2} \right)}{4 \sin^2 \frac{\mu_c}{2}}. \quad (3)$$

Figures 11 and 12 show their dependence on the phase advance per cell, μ_c . The maximum β function (β_{\perp}^{+}/L_c) reaches a minimum at $\mu_c/2\pi = 0.21$. Typically, a phase advance ($\mu_c/2\pi$) between 0.16 and 0.25 (60° – 90° per cell) is selected.

3. Dispersion suppressor

Dispersion-free regions often are created to simplify beam injection, extraction, rf acceleration, and transverse collimation. In such regions, the particles' horizontal and longitudinal motions are decoupled. The goal of suppressing dispersion is to eliminate dispersion in the straight section without affecting the lattice functions in the arc section.

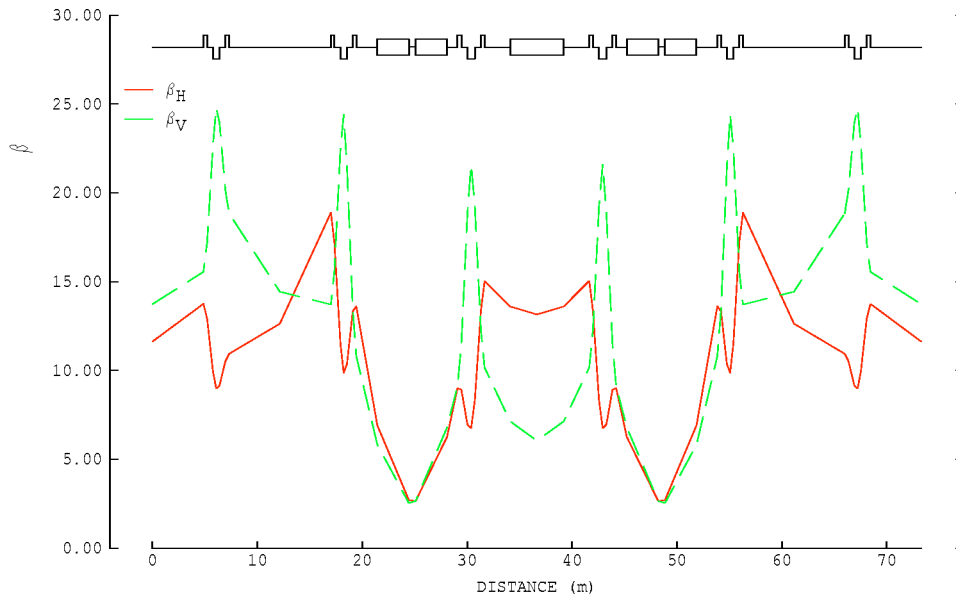
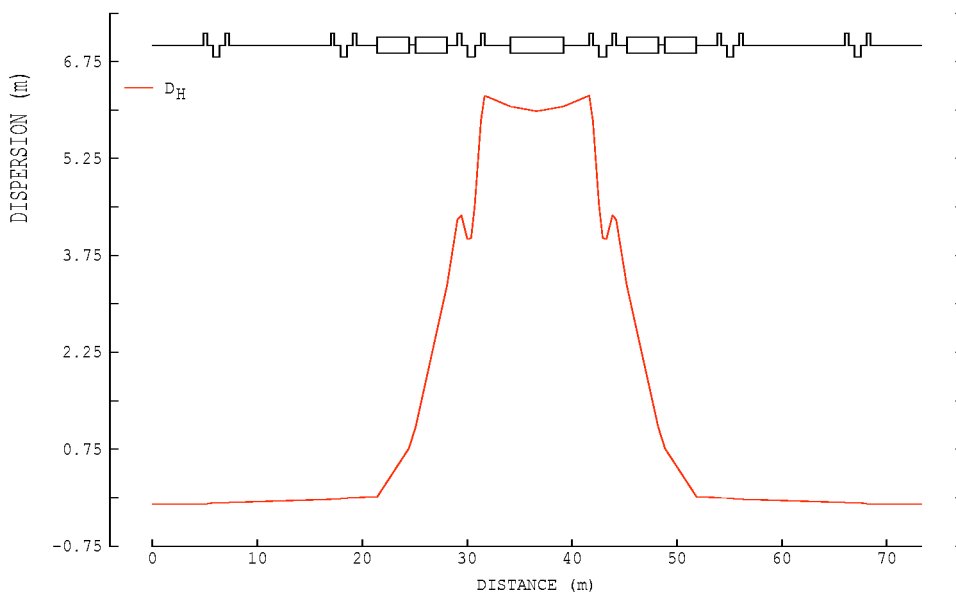
Dispersion in the straight section can be suppressed either by judiciously choosing the horizontal phase advance in the arc or by dedicated dispersion-suppression insertions. By simply making the total horizontal-phase advance across each arc an integer multiple of 2π , dis-

persion outside the arc becomes zero. The advantage of this scheme is that the arc is compact and does not contain any dispersive half-cells. Its disadvantage is that the peak dispersion in the arc is higher than the matched value (Fig. 10).

Common methods of suppressing dispersion using a dedicated insertion are the so-called half-field scheme and its variations. By halving the bending strength, a forced dispersion oscillation is launched around half of the matched value. For a FODO arc structure of horizontal phase advance μ_c per cell, dispersion can be suppressed by π/μ_c FODO cells. If the phase advance per FODO cell in the arc is $\mu_c = \pi/2$, then two FODO cells are needed (Fig. 13). A half-field kick can be realized either by using half-field dipole magnets for bending or by simply omitting the dipole magnet in one of the two FODO half cells. The latter arrangement maximizes the usable dispersion-free drift space and avoids the need for different types of dipole magnets in the arc (Cho *et al.*, 1996).

4. Transition-energy manipulation

With high-intensity synchrotrons, an important issue is to avoid crossing transition during acceleration (Wei, 1990; Sec. III.D.3). A typical approach is to manipulate the lattice to achieve a small or negative momentum compaction α_0 , by either enhancing a higher-order Fourier component of the momentum compaction (the harmonic approach) or introducing bends in a negative-dispersion region (the modular approach Courant, and Snyder, 1958; Teng, 1972; Gupta *et al.*, 1985; Trbojevic *et al.*, 1990; Courant *et al.*, 1991). In designing some proton drivers for neutrino factories and muon colliders, a short bunch length can be realized by operating near transition. Then, control of nonlinear momentum compaction (e.g., α_1) is extremely important.

(a) β -functions

(b) Dispersion function

FIG. 9. (Color in online edition) European Spallation Source (ESS) ring lattice superperiod of triplet structure. The lattice superperiodicity is 3. Along the indicated beam line are dipoles (centered square boxes), focusing quadrupoles (upper bars), and defocusing quadrupoles (lower bars) (Sec. III.A.1). Figure courtesy G. H. Rees and C. R. Prior.

The five rings of the proposed KAON factory were all designed with their transition energies far above the operating range of the machines (KAON, 1990). In each ring, the horizontal tune chosen was just below the number of lattice superperiods (Gupta *et al.*, 1985). Problems associated with this harmonic approach are the large dispersion oscillations and lack of dispersion-free sections. Later, alternative lattices were proposed with the arcs consisting of “supercells” containing the missing bending dipoles (Servranckx *et al.*, 1989; Iliev and Servranckx, 1993). Such a modular approach usually requires many quadrupole magnet families. Figure 14 shows a supercell module containing three FODO cells

with missing dipoles for the 50-GeV ring of the J-PARC project (J-PARC, 2002).

5. Working point

The working point (ν_x, ν_y) , i.e., the horizontal and vertical tunes (or betatron tunes) of the synchrotron, is chosen largely to avoid major linear and nonlinear resonances (Sec. IV.A.7). The selection of the fractional part of the tunes also affects the threshold of transverse instability (Sec. IV.C.3). When the horizontal and vertical motion are to be decoupled, a split-tune working point is usually adopted, with the tunes differing by at least half

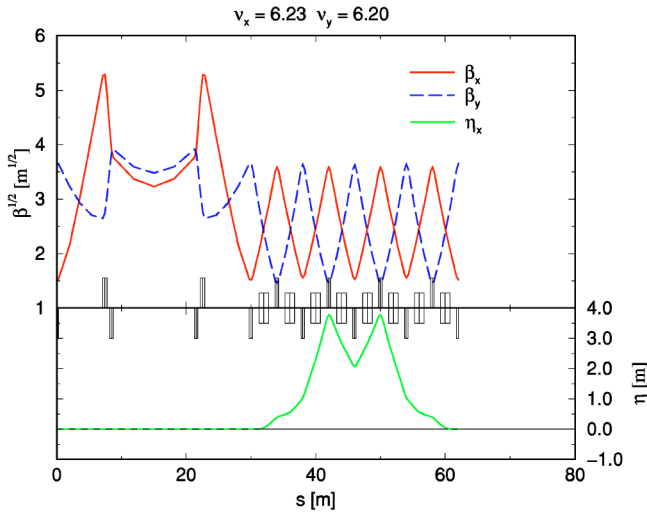


FIG. 10. (Color in online edition) SNS ring lattice superperiod of FODO/doublet structure. The lattice periodicity is 4. Along the indicated beam line are dipoles (centered square boxes), focusing quadrupoles (upper bars), and defocusing quadrupoles (lower bars) (Sec. III.A.1). An alternative lattice is to reverse the polarity of the quadrupoles, in which case the peak dispersion is increased by about 10%.

a unit. At the design stage, it is most important to retain a wide tuning range (one unit or more) in both directions for operational flexibility. Table I lists favorable working points in some existing or designed synchrotrons.

Transverse tunes are often dynamically varied during the beam cycle in synchrotrons to optimize a ring's performance. Figure 15 shows the variation of the horizontal and vertical tunes during the 10-ms cycle in the ISIS synchrotron (Warsop, 1998). The cycle may be divided into four regions where the tune values are adjusted with trim quadrupole magnets to (1) compensate for the natural chromaticity and the varying magnet field at injection, (2) ramp up tunes to minimize effects of space-charge depressions during beam capture, (3) reduce tunes during the time from 2 to 4 ms after injection to

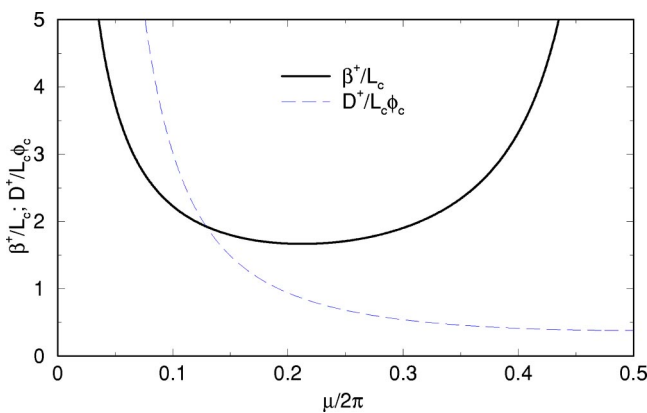


FIG. 11. (Color in online edition) Dependence of maximum amplitude and dispersion functions on the phase advance per FODO cell (Sec. III.A.2).

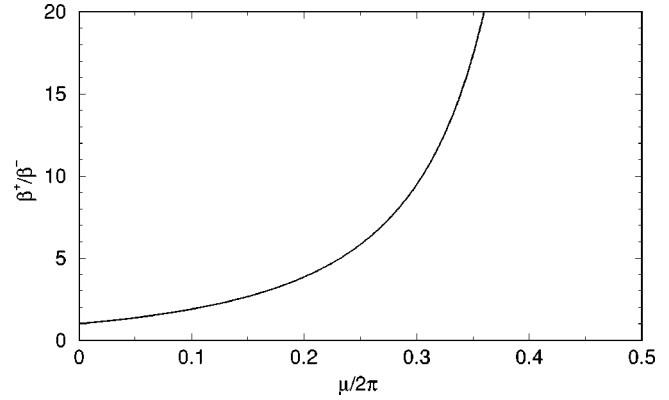


FIG. 12. Dependence of maximum-to-minimum amplitude function ratio on the phase advance per FODO cell (Sec. III.A.2).

avoid transverse resistive wall instability, and (4) lower tunes to avoid coupling resonances at extraction. In the J-PARC's 3-GeV synchrotron, such dynamic tuning is not planned. Instead, chromatic sextupoles will be used to compensate for the natural chromaticity.

Dynamic tuning is usually not used in accumulators due to the relatively short beam cycle. In the SNS accumulator, drift spaces are reserved at symmetric locations of the ring for future pulsed, trim quadrupoles and special vacuum chambers.

6. Acceptance

Acceptance refers to the phase-space area within which particles oscillate stably. A large acceptance is essential to achieving a low-loss operation. Traditionally, the transverse acceptance is designed to accommodate (1) betatron oscillations; (2) the off-momentum closed orbit due to dispersion; (3) design orbit bumps (injection, extraction, diagnostics); (4) closed-orbit deviation due to dipole field errors, beam coupling impedance, and coherent image charge effects; (5) the increase in the beam's amplitude function (β beating) due to quad-

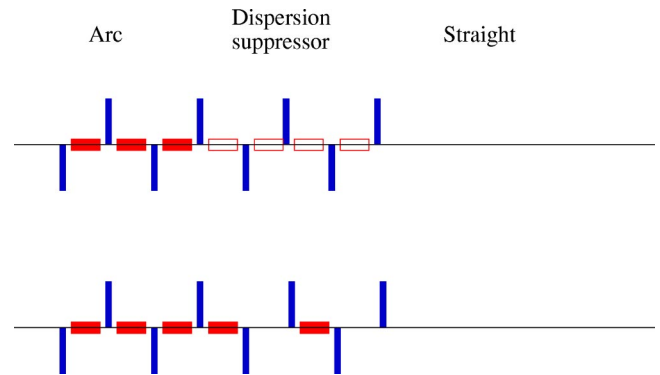


FIG. 13. (Color in online edition) Schematic layout of half-field dispersion suppressors when the betatron phase advance per FODO cell is $\pi/2$ (Sec. III.A.3). Along the indicated beam line are dipoles (centered square boxes), focusing quadrupoles (upper bars), and defocusing quadrupoles (lower bars).

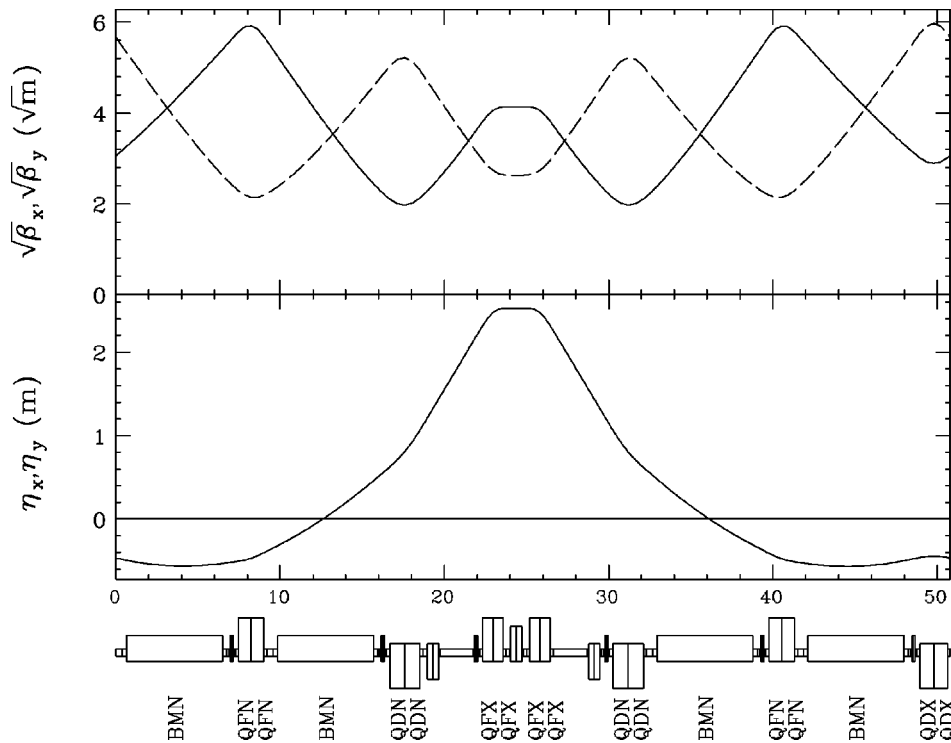


FIG. 14. A supercell lattice module containing three FODO cells with missing dipoles for the J-PARC Project 50-GeV Ring arc section. Along the indicated beam line are dipoles (centered square boxes), focusing quadrupoles (upper bars), and defocusing quadrupoles (lower bars) (Sec. III.A.4). Figure courtesy S. Machida.

rupole gradient errors; (6) degradation in dynamic acceptance due to nonlinear field errors; and (7) possible diffusion due to intrabeam scattering. Longitudinal acceptance is designed to accommodate (1) synchrotron oscillation; (2) rf manipulation; and (3) possible diffusion due to noise and intrabeam scattering (Bryant and Johnsen, 1993; Edwards and Syphers, 1993; Wei, Fedotov, and Papaphilippou, 2001). In recently designed

high-intensity synchrotrons, extra clearance is reserved for multiturn beam-halo collimation and to prevent accidental beam loss due to malfunction of injection and misfiring of the extraction kickers (Wei, Abell, *et al.*, 2000).

Figure 16 illustrates the transverse cross section of the dipole section of an early proposed RCS version of the SNS ring. (Compared with the present AR design, the

TABLE I. Examples of favorable working points in the transverse tune space for some existing and designed rings for high-intensity operations (Sec. III.A.5).

Machine	Superperiodicity	Horizontal tune	Vertical tune	Proton per pulse
Operating:				
AGS	12	8.8	8.9	7×10^{13}
AGS Booster	6	4.8	4.9	2.3×10^{13}
CERN's PSB	16	4.28	5.56	1.3×10^{13}
CERN's PS	10	6.25	6.30	3.2×10^{13}
CERN's SPS	6	26.62	26.58	4.6×10^{13}
FNAL's Booster	24	6.7	6.8	5×10^{12}
FNAL's MI	2	26.425	25.415	3×10^{13}
IPNS	6	2.20	2.32	3.5×10^{12}
ISIS	10	4.31	3.83	2.5×10^{13}
KEK's PSB	8	2.17–2.10	2.30–2.40	2.4×10^{12}
KEK's PS	4	7.14–7.16	5.24	8×10^{12}
PSR	10	3.19	2.19	5×10^{13}
U1.5	12	3.92	3.75	5×10^{11}
U70	12	9.92	9.85	1.2×10^{13}
Designed:				
ESS	3	4.19	4.31	2.3×10^{14}
J-PARC 3-GeV	3	6.72	6.35	8.3×10^{13}
J-PARC 50-GeV	3	22.4	22.25	3.3×10^{14}
SNS	4	6.23	6.20	2×10^{14}

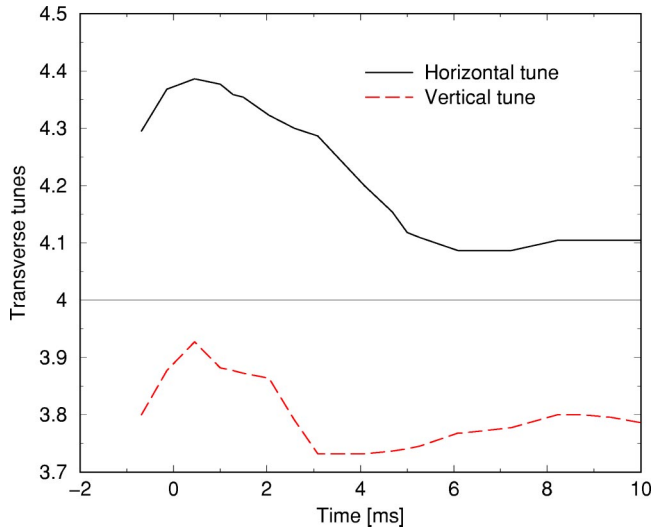


FIG. 15. (Color in online edition) Variation of the transverse tunes during the beam cycle in the ISIS synchrotron when the beam is accelerated from 70 to 800 MeV in about 10 ms. The beam current is 0.2 mA. The maximum incoherent tune depression occurs at about 1 ms (Sec. III.A.5). Figure courtesy C. M. Warsaw.

physical dimension of the vacuum chamber is larger in the RCS design due to the lower injection energy.) The full (unnormalized) beam emittance at the end of injection painting is about $260\pi \mu\text{m}$. The acceptance of the vacuum pipe is above $520\pi \mu\text{m}$ for particles with momentum deviation $\Delta p/p_0 = \pm 1\%$ at all working tunes. This acceptance allows particles scattered by the collimators to return to them without becoming lost elsewhere in the ring. In a dispersive region, the vacuum chamber also accommodates a momentum acceptance of $\Delta p/p_0 = \pm 2\%$ for the $260\pi \mu\text{m}$ beam emittance. The acceptances of the adjustable scraper and fixed collima-

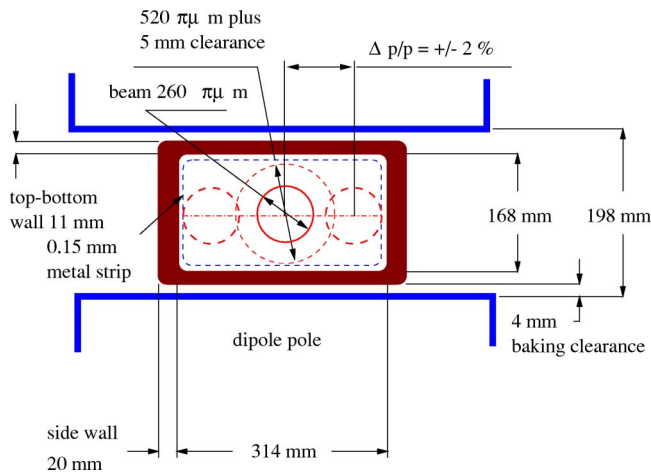


FIG. 16. (Color in online edition) Schematic drawing of the ceramic vacuum-chamber cross section in the dipole region of the proposed RCS version of SNS (Sec. III.A.6). The horizontal acceptance accommodates a momentum deviation of $\Delta p/p_0 = \pm 2\%$. Beam is collimated between 300π and $400\pi \mu\text{m}$ in dispersion-free regions.

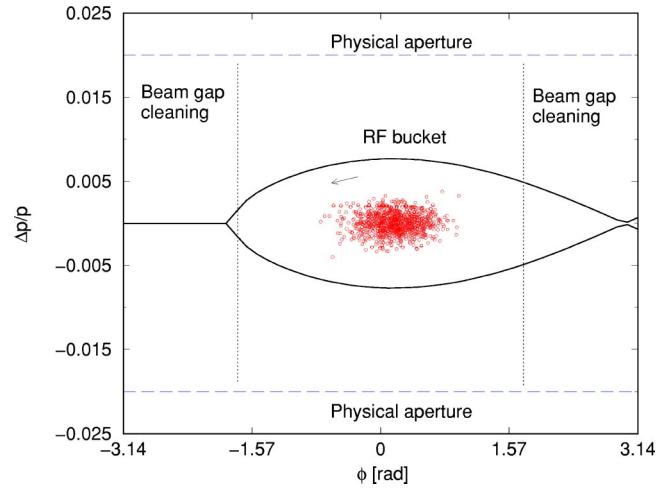


FIG. 17. (Color in online edition) Schematics of the longitudinal rf bucket admittance and accelerator momentum acceptance (Sec. III.A.6). The particles circulate in the phase space counterclockwise below transition energy. Extra longitudinal acceptance is reserved for momentum collimation using the beam-in-gap cleaning system (Sec. III.B.1).

tors are set between 300π and $400\pi \mu\text{m}$ in dispersion-free regions. The difference in acceptance between the collimators and the rest of the ring's vacuum pipe ensures that collimation is highly efficient.

Figure 17 illustrates the longitudinal phase space of the beam contained by an accelerating rf bucket. The vacuum chamber has extra clearance to facilitate longitudinal collimation and beam-in-gap cleaning (Sec. III.B). It also leaves room for future upgrades to the rf system for faster ramping and for damping of instabilities (Sec. IV.C).

B. Beam scraping and collimation

1. Scraping, collimation, and collection

The purpose of beam scraping, collimation, and collection is to localize beam loss to controlled, shielded areas, and thus to reduce uncontrolled radioactivity. The H^- beam is usually cleaned with a stripping foil, and then a magnetic field separates the stripped beam from the original H^- beam. The proton beam generally is cleaned with a two-stage system, wherein the primary scraper scatters the beam and enhances its impact distance in the secondary collector, so achieving a high cleaning efficiency (Teng, 1969).

For a new facility, the linac-to-ring transport frequently is contrived to clean the incoming beam halo from the linac, to mitigate the effects of source and linac malfunction, and to reduce injection activation (Sec. III.F). Transversely, scrapers are located with a chosen phase-advance between them to clean the beam halo in phase space (Bryant and Klein, 1992; Trenkler, 1992). Longitudinally, an achromatic bend creates dispersion for cleaning the momentum halo (Raparia *et al.*, 1998; ESS, 2002).

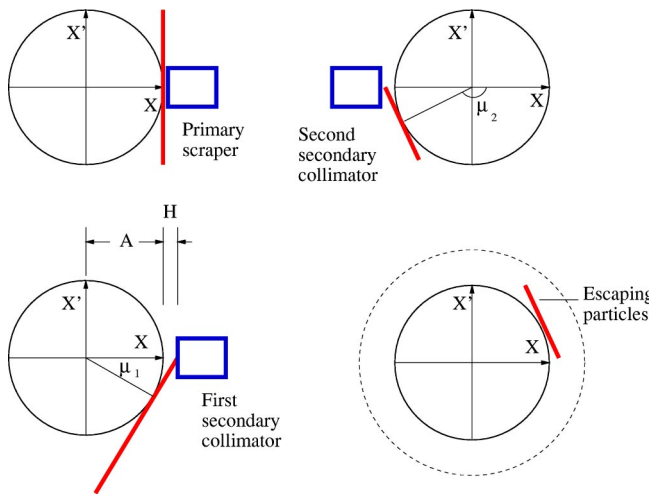


FIG. 18. (Color in online edition) Schematics in normalized phase space of a two-stage collimation with one primary scraper and two secondary collimators located at chosen phase advance (Sec. III.B.1).

The beam halo generated in the ring can be cleaned both in the transverse and the longitudinal phase space (Catalan-Lasheras, Lee, *et al.*, 2001). For transverse collimation, scrapers and collimators are arranged in dispersion-free regions. Optimization of the relative phase advance and the acceptance of the primary scraper and secondary collimators maximizes the efficiency of collimation and minimizes beam loss on unprotected elements (Bryant and Klein, 1992; Trenkler, 1992). Efficient collimation requires an adequate acceptance ratio between the scraper and collimators, and the rest of the vacuum pipe (Fig. 18).

Longitudinal cleaning can be accomplished in the momentum and in the azimuthal phase space. The momentum halo can be cleaned in several ways: (1) injecting in a high-dispersion region and collecting at 180° phase advance downstream (ISIS, ESS), as shown in Fig. 19 (ESS, 2002); (2) scraping at a high-dispersion lattice location (J-PARC) as shown in Fig. 20 (J-PARC, 2002); and, (3) using a beam-in-gap kicker (SNS) (Witcover *et al.*, 1999; Catalan-Lasheras, Lee, *et al.*, 2001; Cousineau *et al.*, 2001). The latter method requires an adequate momentum clearance so that particles can reach the gap without loss. Azimuthal-phase cleaning, or cleaning of the “beam gap,” can be done with a wide-

band stripline kicker to resonantly excite coherent betatron oscillations, driving the residual beam in the gap into the transverse collimators.

To reduce activation at ring extraction, the beam in the gap must be cleaned either during the initial ramping for synchrotrons, or with beam-in-gap kickers for accumulators. Additional collimators are placed in the postextraction transport to protect experimental and application targets.

2. Scrapers and collimators

Primary scrapers are usually adjustable, thin blades, the material and thickness of which are optimized for scattering, heating, and other engineering properties. The primary scraper of the SNS ring consists of four tantalum blades, each 5 mm thick. They are spaced in 45° angles, adjustable to the varying needs of collimation aperture. The scraper assembly is shielded for containing radioactivity. Although channeling crystals are considered possible candidates for primary scrapers, their channeling acceptance and resistance to heat and radiation need to be tested for high-intensity proton beams at relatively low energies (Carrigan, 1987; Maslov *et al.*, 1991; Biryukov *et al.*, 1997).

Secondary collimator and collector units designed for high-intensity synchrotrons typically are nonadjustable, complex elements, unlike collimators meant for high-energy accelerators that often consist of adjustable solid-metal jaws (Kaltchev *et al.*, 1997). Anticipating a relatively high beam power (typically 10 kW) and a high radioactivation level, these units are cooled by closed-loop circulating water. These units are long enough to stop the primary beam. Because they consist of layers of stainless-steel blocks, stainless-steel balls, borated water, and the like, they can also contain secondary charged and uncharged particles as well as radioactivity (Ludewig *et al.*, 1999).

Figure 21 shows the collimator design for the SNS accumulator ring. The vacuum chamber is made of double-layered stainless steel filled with helium gas between the layers to detect leaks (Simos *et al.*, 2001). Due to stringent engineering requirements for stress and heat tolerance, thermal contraction, and shielding, for operational reliability these units are not adjustable in collimation cross section (Ludewig *et al.*, 2000).

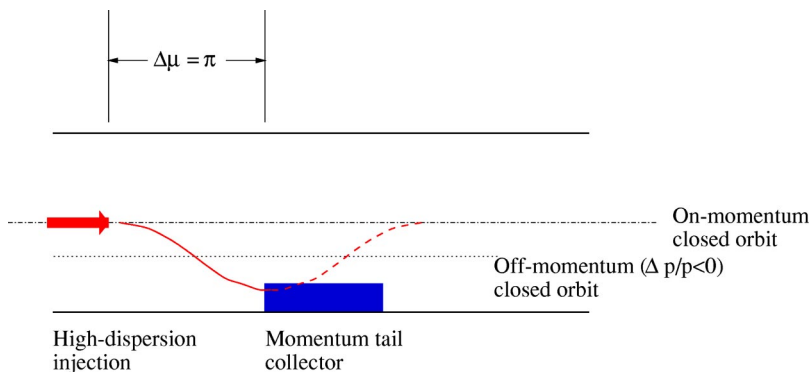


FIG. 19. (Color in online edition) Collection of injection off-momentum tail by injecting at a high-dispersion region, as at the ISIS and the proposed ESS (Sec. III.B.1).

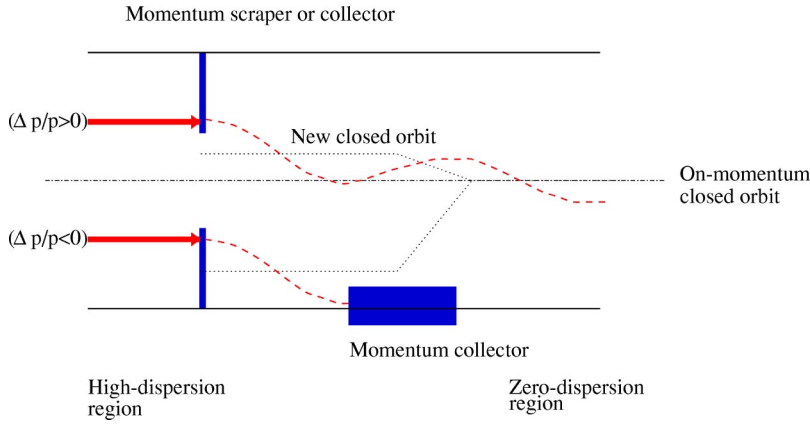


FIG. 20. (Color in online edition) Momentum collimation or collection at high-dispersion region, as at the J-PARC synchrotrons (Sec. III.B.1).

C. Injection

During the acceleration of protons, the transverse amplitudes of oscillation fall according to the adiabatic damping of the phase space (Bryant and Johnsen, 1993). Thus the beam size usually is largest at the injection energy. At low energies, space-charge forces produce large shifts in transverse tunes because there is little cancellation between electric and magnetic forces at nonrelativistic energies. The combination of these two effects makes injection one of the most challenging periods for preserving beam emittance and minimizing beam loss during the synchrotron’s acceleration cycle.

Beams can be injected into synchrotrons in several ways: single-turn injection with septum and kicker magnets; multiturn proton injection with septum and orbit bump; and, multiturn charge-exchange injection using a stripping foil. A successful injection requires a high-quality injecting beam with little centroid jitter and a controlled emittance, an adequate uniformity in the magnetic field along the path of the beam in the septum and subsequent magnets, an adequately fast rise time and flat wave form in the kicker or bump magnets and their power supplies, and an rf system able to contain the transient beam-induced field (“beam loading”; Rees, 1994, 1998).

1. Single-turn injection

Single-turn injection generally is used to transfer a bunched beam from one ring to another. Transversely, the injecting beam’s profile must be matched to the accelerator lattice to preserve the emittance. Longitudinally, the frequency of the rf system must be synchronized, and the aspect ratio between the momentum and phase spread needs to be matched to the contours of stable synchrotron oscillations.

2. Multiturn proton injection

Multiturn proton injection can accommodate a long pulse of beam from the injecting linac or cyclotron. The efficiency of injection can be optimized by a specific mismatch. Let the horizontal Courant-Snyder parameters and emittance for the injected beam be $(\beta_{x,i}, \alpha_{x,i}, \epsilon_{x,i})$ and for the ring $(\beta_x, \alpha_x, \epsilon_x)$, and let the input beam’s

center relative to the instantaneous injection orbit bump be (x, x') . Then, the injection conditions are (Rees, 1994; Prior and Rees, 1998)

$$\frac{\beta_x}{\beta_{x,i}} = \left(\frac{\epsilon_x}{\epsilon_{x,i}} \right)^{1/3}; \quad \frac{\alpha_x}{\beta_x} = \frac{\alpha_{x,i}}{\beta_{x,i}} = - \frac{x'}{x}. \tag{4}$$

With Eq. (4), the curvature of the injecting beam matches that of the circulating beam (Fig. 22). The maximum number of injection turns, typically several tens, depends on the ratio of ring acceptance to the injecting-beam emittance and on the ring lattice’s properties, such as tunes. The efficiency of multiturn injection can be increased by a transverse coupling using skew quadrupole magnets (as in the CERN PSB and the AGS Booster).

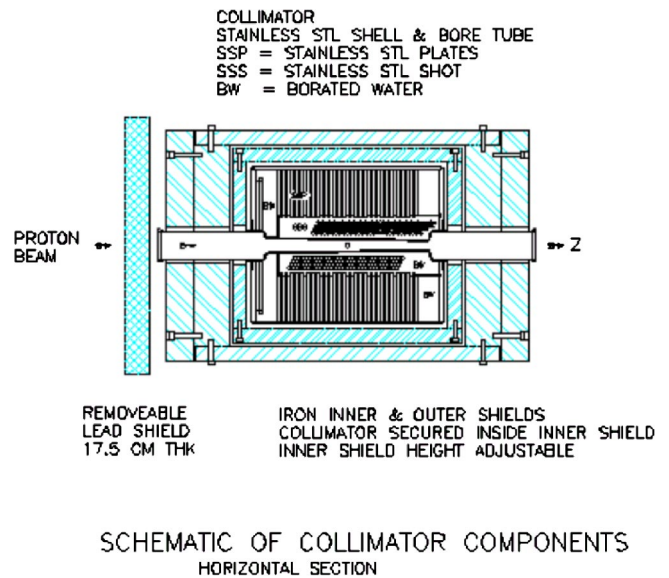


FIG. 21. (Color in online edition) Schematics of one of the SNS ring’s secondary collimators, showing layers of material for radioactivation containment. The effective length is about 1.5 m. The collimator is designed to withstand an average beam power of up to 10 kW at 1 GeV kinetic energy (Sec. III.B.2). Figure courtesy H. Ludwig and N. Simos.

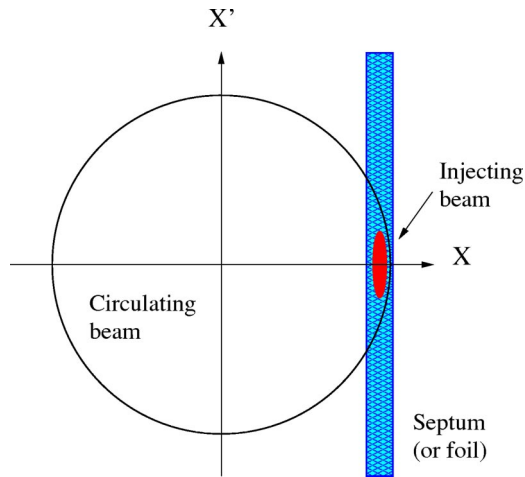


FIG. 22. (Color in online edition) Mismatched multiturn injection in the normalized transverse phase space (Sec. III.C.2). In this design, the width of the injection foil is minimized. (A matched beam would be circular in cross section.)

3. Multiturn charge-exchange injection

Charge-exchange injection is preferred for modern high-intensity rings because it allows a large number of revolutions to be injected and controlled to realize a desired beam distribution. The constraints imposed by Liouville's theorem on conventional multiturn injection do not apply since the H^- ions are stripped within the acceptance of the ring. With a programmed orbit bump, several hundreds of turns can be injected into the ring with tolerable foil scattering.

Key issues in charge-exchange injection are associated with stripping and collecting the electrons of the H^- beam. The magnetic field B in the transport and the injection region must be low enough so that beam loss due to magnetic stripping is acceptable. This condition becomes increasingly stringent for injection at higher energies. The scaling law is calculated from the requirement that the mean decay length λ_s due to Lorentz stripping be much longer than the path length in the laboratory frame (Furman, 1998),

$$\lambda_s = \frac{A_{s1}}{B} \exp\left(\frac{A_{s2}}{\beta\gamma B}\right), \quad (5)$$

where the coefficients $A_{s1} = (2.47 \pm 0.09) \times 10^{-6}$ Tm, and $A_{s2} = 15.0 \pm 0.03$ T are valid for $\beta\gamma B$ from 0.62 to 2.34 T. The magnetic field around the stripping foil must be such that the residual, excited-state H^0 particles produced from the stripping foil are extracted from the ring with negligible decay (Rees, 1994; Blumberg and Lee, 1996).

The stripped electrons have a kinetic energy of $m_e c^2(\gamma - 1)$, where γ is related to the kinetic energy $m_0 c^2(\gamma - 1)$ of the injecting proton. The electron current is twice that of the proton-beam current. This electron beam, often at a kW power level produced from a MW proton beam, has as small a cross-section as does the injecting proton beam. It needs to be guided by a magnetic field and collected by a water-cooled device of

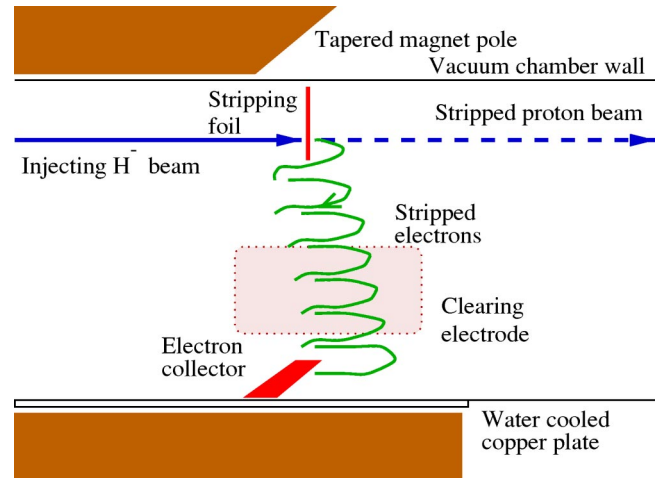


FIG. 23. (Color in online edition) Collection of stripped electrons during the injection of H^- beam at the SNS accumulator ring. The stripped electrons are guided by a magnetic field and collected by a water-cooled device of heat-resistant material (Sec. III.C.3).

heat-resistant material (Jason *et al.*, 1994; Abell *et al.*, 2000). Figure 23 shows the collection of stripped electrons at the SNS accumulator ring. The electron collector uses a carbon material attached to a water-cooled copper plate (Brodowski, 2002). Selecting a low-charge-state material for the collector also reduces the effects of backscattered electrons.

Significant efforts have been made to optimize the stripping foil's performance. The density of the foil, typically $200\text{--}400 \mu\text{g}/\text{cm}^2$, is a compromise between its stressing and heating, and stripping efficiency. For easy placement, the foil, with its size minimized so as to reduce the number of traversals of the beam, can be hung from a frame, supported with thin fiber, and mounted on quick-exchange devices (Brodowski, 2000). During recent tests, foils made of diamond material showed good heat resistance and a significantly improved lifetime that meets the requirements of a high-intensity injection (Liaw *et al.*, 2001; Shaw *et al.*, 2003). Forming the foil into a cylindrical tube instead of a flat piece may improve its mechanical support and performance (Brodowski, 2002).

Laser stripping was explored as an alternative to foils but the required power and efficiency are very demanding (Yamane, 1998; Suzuki, 1999). Other novel injection schemes include resonance injection, radio-frequency stacking, and beam-cooling stacking. However, these processes are too slow to accommodate a high repetition rate.

ISIS and ESS inject at a high-dispersion region, as shown in Fig. 24 (Boardman, 1982; ESS, 2002). The injection dipole magnet, part of the periodic lattice structure, separates the injecting and circulating beams without using a septum. Thus the arrangement of the injection magnets is simplified. The high dispersion at injection also facilitates the collection of the momentum halo (Sec. III.B).

In contrast, SNS injects in a zero-dispersion straight

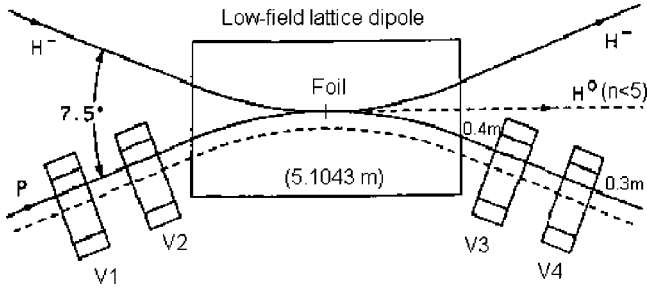


FIG. 24. ESS dispersive injection layout indicating the injection dipole and four vertical painting bump magnets. The long injection dipole is part of the periodic lattice structure (Sec. III.C.3). Figure courtesy of C. Prior and G. H. Rees.

region (Fig. 25), thereby allowing independent control of phase-space painting both transversely and longitudinally (Wei, Abell, *et al.*, 2000). The injection process is more tolerant to deviations in linac energy. A long, uninterrupted straight is preferred to contain the entire injection chicane, so that the effects of lattice tuning can be minimized. Intentionally mismatched injection can noticeably reduce the foil traverses (Beebe-Wang *et al.*, 2000; Galambos *et al.*, 2000).

4. Phase-space painting

Injection painting refers to the process of populating the phase space with the injected beam to realize a de-

sired distribution. Transverse painting alleviates the fundamental limit on space charge and controls the uniformity and shape of the beam’s profile. Transverse painting can be realized in several ways: varying the closed-orbit bump in the ring (Fig. 26); varying the angle of the injecting beam (Fig. 27); or varying the injecting beam’s energy upon injection in a dispersive location (Fig. 24).

Anticorrelated painting utilizes both the horizontal and vertical orbit bumps, one with increasing and the other with decreasing closed-orbit bump amplitude, respectively. Ideally, this painting scheme produces a distribution with an elliptical transverse profile and a uniform density distribution. Such a configuration can also be obtained by painting in one direction and steering in the other (Wei, Beebe-Wang, *et al.*, 2001). However, in the presence of strong space charge, this scheme can produce an excessive beam halo in the direction of the large initial oscillation amplitude, which requires extra clearance.

Correlated painting using parallel horizontal and vertical orbit bumps generates a rectangular transverse profile. Its advantage is that the beam halo is constantly painted over by the freshly injected beam. The main concern is whether the rectangular beam profile can be preserved in the presence of coupling produced by space charge and magnetic errors (Fedotov, Gluckstera, and Wei, 2001). SNS adopts correlated painting to realize

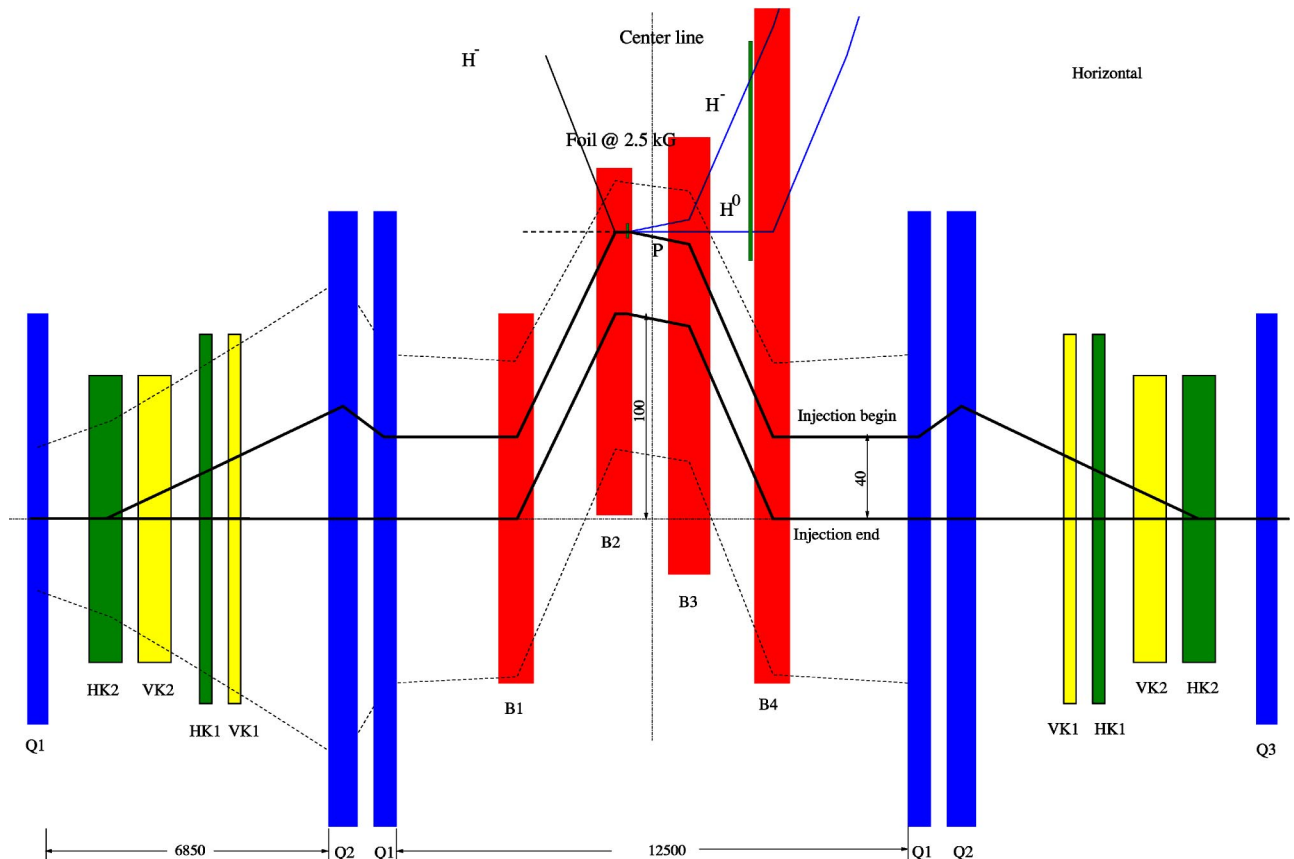


FIG. 25. (Color in online edition) SNS dispersion-free injection. Elements shown are the chicane (B1, B2, B3, and B4), the ring lattice quadrupoles (Q1, Q2, and Q3), and dynamic kickers (horizontal HK1 and HK2, and vertical VK1 and VK2) (Sec. III.C.3).

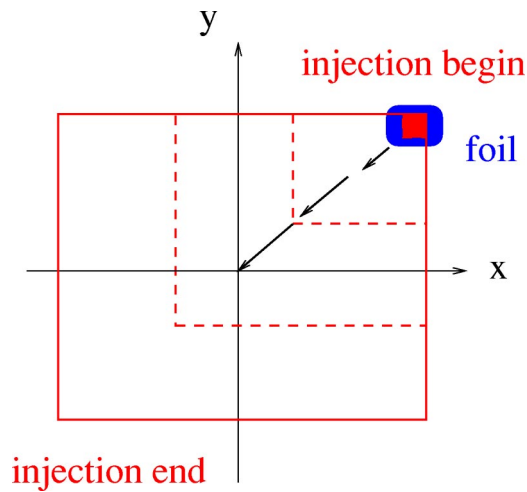


FIG. 26. (Color in online edition) Beam transverse profile of correlated bump painting used in charge-exchange injection into the SNS ring (Sec. III.C.4).

equal transverse emittances, operating near coupling resonance to achieve a fully coupled, circular distribution in the physical dimension. More sophisticated schemes have proposed, using alternating orbit bumps and relying on controlled transverse coupling (Beebe-Wang *et al.*, 2000; Franchetti and Hofmann, 2000; Loulergue *et al.*, 2001).

Longitudinal painting provides the momentum spread required for beam stability without introducing an excessive momentum halo (Fig. 28). With dispersion-free injection, longitudinal painting can be achieved for linac-to-ring injection by using an “energy spreader” rf cavity located in the transport line upstream of the injection region, which is phase modulated with respect to the linac frequency. To facilitate such a painting scheme, the injecting beam’s momentum jitter and spread need to be controlled, possibly by an “energy corrector” rf cavity synchronized to the linac’s frequency, again located in the transport line upstream of injection at an optimized distance from the end of linac. SNS uses this

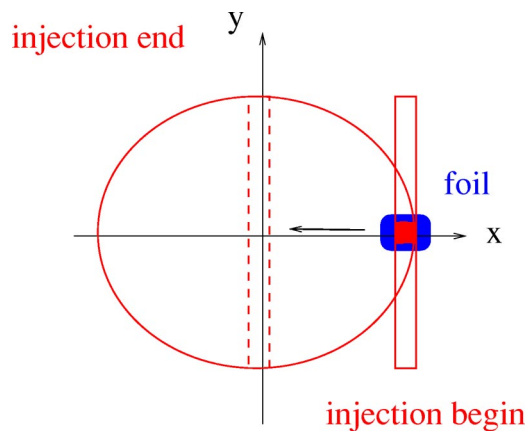


FIG. 27. (Color in online edition) Beam transverse profile of horizontal painting/vertical steering similar to the scheme used in the charge-exchange injection in the J-PARC 3-GeV ring (Sec. III.C.4).

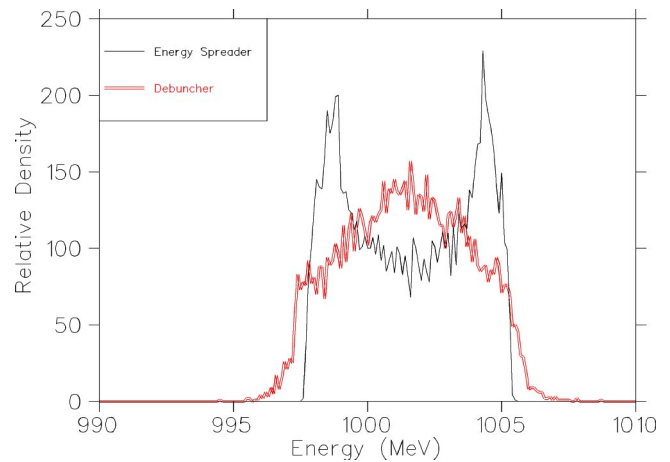


FIG. 28. (Color in online edition) Energy distribution at the injection foil, using either an energy spreader or a conventional debuncher. An energy spreader significantly suppresses the beam tail (Sec. III.C.4).

arrangement to allow for adequate beam-phase slippage and thus moderate rf voltage (Raparia *et al.*, 1998).

Phase-space painting that correlates the longitudinal and horizontal motion is proposed for the ESS accumulator rings (Fig. 24; Prior and Rees, 1998). Beam distribution in both horizontal and longitudinal phase space depends strongly on the energy variation during injection and on the frequency of synchrotron oscillation.

Beam acceleration using induction devices was proposed to realize barrier-bucket acceleration (Christofilos *et al.*, 1964; Takayama and Kishiro, 2000). Computer simulation indicates that a large bunching factor can be realized to alleviate space-charge effects.

D. Acceleration

1. Radio-frequency capture

For rapid-cycling synchrotrons, significant beam loss often occurs during the injection period when a coasting beam is adiabatically captured by the radio-frequency system, and also during initial acceleration (or “ramping”) when the phase-space area of stable longitudinal motion (the so-called “rf bucket area”) tends to decrease with the rising synchronous phase (Bryant and Johnsen, 1993; Wei, Fedotov, and Papaphilippou, 2001). Commonly, the beam is prechopped at low energy to realize a clean gap between successive beam bunches. The voltage amplitude of the ring rf system must be programmed according to the rising synchronous phase to ensure a monotonically increasing rf bucket area.

Radio-frequency systems operating at multiple frequencies can be combined to shape the rf bucket and flatten the peak beam density in several ways. For a dual-harmonic system, the frequency of the secondary rf system is chosen to be an integral multiple of the fundamental rf system. Typically the ratio in operating voltage amplitude is inversely proportional to the ratio in rf frequency. With this choice, the frequency of synchrotron oscillation extends from zero at the center of the bucket

to a maximum value across its core about 1.2 times the maximum synchrotron frequency of a single-harmonic system (Hofmann and Myers, 1980; Wei, 1992). Thus the spread of synchrotron frequency in the bunch usually is greatly enhanced.

Radio-frequency gymnastics techniques, such as bunch recombination and coalescing, are commonly used to manipulate the longitudinal distribution of the bunch (Griffin *et al.*, 1983; Brennan *et al.*, 1994; Garoby, 1998). Techniques employing wide-bandwidth frequency cavities (so-called “barrier cavities”) compress the bunch azimuthally, increasing the total number of injected bunches for heightened beam intensity (Blaskiewicz *et al.*, 1999; Fujieda *et al.*, 1999).

2. Ramping, power supply, and rf system

The magnet power supply and rf systems represent major engineering challenges associated with fast energy ramping. At present, three types of magnet power system commonly are used for synchrotrons: bridge rectifiers directly connected to the power grid (e.g., BNL AGS Booster); bridge rectifiers with local energy storage in the generator set (e.g., BNL AGS); and, resonant power systems with local energy storage in capacitors and chokes (e.g., ISIS). Rapid-cycling synchrotrons demand a large amount of electrical power (typically tens of megawatts) for the magnet and rf systems. As a general rule, the higher the repetition rate, the larger is the peak power drawn from the power grid, and the more likely is the need for local energy storage. Thus most existing rapid-cycling synchrotrons use resonant power systems.

With a resonant power system, the strength of the magnetic field varies sinusoidally along with the rigidity of the beam. The consequences are the lack of a “flat bottom” for a static injection condition, and the demand for high voltage amplitude by the rf system to sustain the largest ramping slope of the sinusoidal wave form. The quality of the magnet field usually suffers from current-induced effects and saturation. A variation is a dual-harmonic ramping with a slower slope during the up-ramp (acceleration) and faster slope during the down-ramp (IPNS, 1995; FNAL PD, 2000).

To satisfy the increasing need to accurately control the injection “flat bottom” and extraction “flat top,” and to have a flexible program of magnet current, high-frequency ac bridge rectifier systems are under development, such as those based on IGBT (insulated gate bipolar transistor) rectifiers. A programmable ramp using this technology provides maximum flexibility in manipulating the profile of the rise and fall, thus reducing the peak ramp rate and current-induced magnetic imperfections.

Proton acceleration in medium-energy, high-intensity synchrotrons (with a circumference of several hundred meters and kinetic energy from near one to several tens of GeV) typically are achieved with ferrite-loaded rf cavities, with an accelerating gradient around 10 kV/m in a frequency range from 1 to 20 MHz. Modern rapid-cycling synchrotrons demand a higher acceleration gra-

dient to attain sufficient accelerating voltage in the limited dispersion-free straight sections. Materials for magnetic energy storage are needed, with saturation magnetization beyond that of the ferrites. Some promising candidates are the crystalline magnetic-alloys like Finemet (Hitachi Co., Japan), and Metglass (Vitrovac, Germany). Prototype cavities using Finemet have successfully achieved a gradient of 50 kV/m at the BNL AGS and FNAL (Mori *et al.*, 1998; Ohmori *et al.*, 1999).

In addition to the development of high-gradient accelerating cavities for synchrotrons, muon-collider applications demand the exploration of burst-mode rf cavities for rotating proton bunches and manipulating muons. A research program is currently directed toward realizing an accelerating gradient around 1 MV/m at a frequency above 5 MHz (FNAL PD, 2000; Chou and Wei, 2001).

Radio-frequency “beam loading” refers to the transient response of the rf system to variations in the beam’s current, frequency, and energy (Wilson, 1974; Pedersen, 1975; Boussard, 1998). Compensation for “beam loading” aims at maintaining a stable accelerating voltage in the presence of varying beam conditions. The effect of beam loading is simplified by the AR option of using a fixed-energy accumulator ring. New challenges are associated with compensating high-intensity beam loading in the magnetic-alloy cavities where the broadband resonance spans several rf harmonic frequencies.

Detailed engineering design is needed to minimize system noises. Measures like ground break (separation of electrical grounding of different accelerator systems) are used to isolate pulsed signals from high-power power-supply systems and to minimize their interference with beam dynamics, accelerator control, and diagnostics. On the other hand, in comparison with colliders where the beam is stored for an extended period of time, requirements on power-supply ripples and rf system noise for a typical high-power ring are less stringent due to the relatively short time period of beam accumulation and acceleration.

3. Transition crossing

Among existing rings in which the beam has to cross transition energy (e.g., the AGS, the CERN PS and SPS, the KEK PS, and the FNAL Booster), beam loss and emittance growth often are observed due to chromatic nonlinearity, self-field mismatch, and instabilities (Sørensen, 1975; Wei, 1990, 1998). At the CERN SPS, the injection energy is raised to avoid transition during intense single-bunch operation. Longitudinal head-tail instability caused by the nonlinear momentum compaction further complicates injection near transition.

Complications at the transition energy are attributed to the nonadiabaticity of longitudinal motion. The characteristic time T_c near transition energy γ_T is

$$T_c = \left(\frac{\pi E_s \beta^2 \gamma_T^3}{q e V_{rf} |\cos \phi_s| \dot{\gamma} h \omega_s^2} \right)^{1/3}, \quad (6)$$

where E_s is the energy of the particle, qe is the electric charge, V_{rf} is the peak acceleration voltage, h is the rf harmonic number, and ω_s is the angular-revolution frequency. Thus a high acceleration rate $\dot{\gamma}$ is essential in reducing complications at transition.

Single-particle effects include mismatching to the accelerating rf bucket, coupling to transverse motion, and various kinds of mistiming in a duration comparable to T_c . Chromatic nonlinearities cause particles of different momenta to cross the transition at different times described by the time scale T_{nl} , where the “nonlinear time” T_{nl} is proportional to the rms momentum spread σ_p at transition (Johnsen, 1956; Takayama, 1984; Lee and Wei, 1988)

$$T_{nl} = \left| \left(\alpha_1 + \frac{3\beta^2}{2} \right) \frac{\sqrt{6}\sigma_p\gamma_T}{\dot{\gamma}} \right|, \quad (7)$$

where α_1 is the first-order nonlinear momentum compaction factor. The growth in longitudinal emittance is proportional to the ratio T_{nl}/T_c (Wei, 1990). Methods of compensating for this nonlinear effect include (1) a lattice design with $\alpha_1 \approx -3\beta^2/2$ to minimize leading-order chromatic nonlinearity, (2) a reduced rf voltage that decreases momentum spread, and (3) a faster transition-crossing rate that also reduces momentum spread at crossing.

Multiparticle effects at transition include longitudinal bunch-to-bucket mismatch and microwave instabilities. A capacitive (or inductive) longitudinal coupling impedance $Z_{||}$ near the frequency of the bunch defocuses (or focuses) it below transition, and focuses (or defocuses) it above. This change in focusing property causes a growth in longitudinal emittance proportional to the ratio of the beam-induced force to the rf accelerating force (Sørensen, 1967; Wei, 1990),

$$\frac{\Delta S}{S} \approx \frac{h\hat{I}|Z_{||}/n|}{3V_{rf}|\cos\phi_s|\sigma_\phi^2}, \quad (8)$$

where \hat{I} is the peak beam current at transition, σ_ϕ is the rms phase spread, and n is the frequency harmonic. Equation (8) is valid exactly for a parabolic distribution under the space-charge force. A longitudinal resistive coupling impedance near the bunch frequency dissipates energy, shifts the synchronous phase, and produces a growth in emittance. A capacitive (or inductive) longitudinal broadband impedance may cause a microwave instability after (or before) the transition. A resistive longitudinal impedance may cause instability both below and above the transition. The microwave instability near γ_T was observed experimentally and has been simulated. The jump in ϕ_s at transition induces a severe beam-loading transient, while the cavity tuning system changes the sign of the reactive beam-loading compensation. Countermeasures for these self-field effects include (1) reducing the effective coupling impedance; (2) increasing the rf voltage and focusing force; and, (3) raising the transition-crossing rate.

The transition energy of the ring can be varied during a short period of time by a perturbation of the machine's

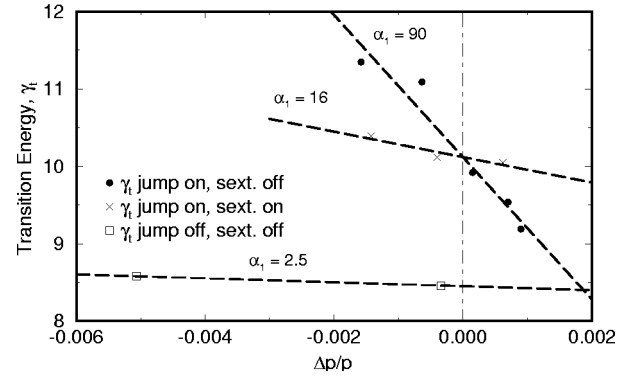


FIG. 29. Measured transition energy as a function of the momentum deviation of the gold beam at the AGS (Sec. III.D.3). A transition jump using pulsed quadrupoles reduced beam loss at high intensity but caused lattice distortion. Sextupoles could be used to correct the distortion.

lattice. Typically, the effective crossing rate $|\dot{\gamma} - \dot{\gamma}_T|$ can be increased by many times of $|\dot{\gamma}|$. To avoid variations in tune, γ_T can be suddenly changed by pulsing quadrupoles, often grouped in π doublets, at places of high dispersion. At the AGS, a transition jump using pulsed quadrupoles was employed to minimize beam loss at high intensity (Hardt and Mohl, 1969; Lee and Teng, 1971). The large lattice distortion introduced by the jump system before the crossing severely limits the machine's aperture. Efforts to correct the distortion with existing sextupoles were partially successful (Fig. 29; Wei, Brennan, *et al.*, 1995).

Newly designed rings usually avoid transition either by selecting the energy of injection and extraction or by manipulating the lattice, creating negative dispersion in the bends. For rings that must cross transition, e.g., at the Relativistic Heavy Ion Collider (RHIC), an optically matched transition jump is preferred, using multiple quadrupole families located at different values of dispersion (Risselada, 1990; Peggs *et al.*, 1993).

E. Extraction

Beam extraction usually entails the possibility of heavy beam loss and radioactivation. Typical beam loss is attributed to (1) accidental misfiring of the kicker power supply; (2) residual beam in the beam gap between adjacent bunches; (3) lack of transverse aperture in the extraction channel; and, (4) lack of momentum aperture in dispersive sections of the extraction channel. Other factors are the slow rise of, and nonflatness in, the kicker pulse wave form, and resonance loss in the case of a multturn slow extraction.

In newly designed high-intensity rings, the beam is extracted during a single turn by being kicked into the extraction channel of the septum magnet. This is the reverse process of single-turn injection. The average deflection in transverse momentum is given by

$$\langle \theta_{\text{kicker}} \rangle \approx \frac{x_{\text{sep}}}{\langle \sqrt{\beta_{\text{kicker}}} \sin \Delta\mu \sqrt{\beta_{\text{sep}}} \rangle}, \quad (9)$$

where x_{sep} is the design displacement at the extraction septum, β_{sep} and β_{kick} are the amplitude functions at the septum and kicker, respectively, and the optimum phase advance $\Delta\mu$ between the kicker and the septum is $\pi/2$. Often the kicker consists of multiple modules, so that beam loss is negligible even when one module fails. The pulse-forming network (PFN) is installed outside the ring tunnel for easy maintenance. In spallation applications, the phase advance between the extraction kicker and the target also is chosen so that the beam's position on target does not change if errors develop with the kickers.

To avoid complications due to rapid variations of the magnetic field, kicker magnets are made with a single-turn coil winding and are placed inside the vacuum chamber. Good field quality is achieved with a high-permeability ferrite material. In high-repetition-rate applications, sometimes water cooling is introduced to avoid heating, as at the ISIS. The typically high beam-coupling impedance associated with the high-permeability material can be reduced, and undesirable resonance structure can be avoided by the selection of termination in the pulse-forming network (PFN) circuit. A saturable inductor can isolate the influence of the PFN, shorten the rise time, and improve the flatness of the kicker-pulse's waveform (Wait, 1997). At the SNS, the 700-ns beam pulse is vertically kicked by 14 kicker modules each contributing about 1.5 mrad deflection, and then horizontally extracted with a Lambertson-type septum magnet (Tsoupas, Blaskiewicz, *et al.*, 2000). To ensure the maximum deflection, the kicker ferrite modules, with their acceptance containing both the circulating and extracting beams, are designed with a tight clearance. Thus the circulating beam's center deviates vertically from the module's mechanical center. The transverse coupling impedance introduces an intensity-dependent deflection that produces a closed-orbit deviation with peak amplitudes varying longitudinally from the center to the edge of the beam pulse; also known as a banana closed orbit (Fig. 30; Lee, 2002).

An alternative kicker design is to have transmission-line plates inside the vacuum chamber (as done at the PSR and proposed for the AHF). Extraction can be eased further by introducing orbit bumps before extraction, but at the expense of reduced aperture clearance. Recently, stacked MOSFET modulators have replaced traditional thyatron-based modulators to achieve a short rise and fall time [about 20 ns for 10–90 % rise and fall (Walstrom and Cook, 2001)].

F. Transport lines

More than simply connecting two accelerators, transport lines in modern high-intensity facilities serve the purpose of transverse optical matching, beam diagnostics, fault protection, beam collimation, and injection preparation. The layout of the transport line can be separated into straight sections of zero dispersion or achromat arcs of high peak-dispersion. The straight section design was created for transverse beam-diagnostics,

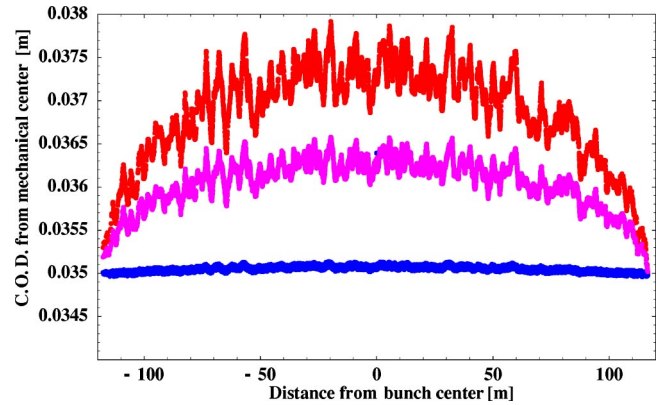


FIG. 30. (Color in online edition) Orbit deviation for three turns due to beam-centroid offset from the mechanical center of the extraction kickers (Sec. III.E). The transverse coupling impedance introduces an intensity-dependent deflection that produces a closed-orbit deviation with amplitudes varying longitudinally from the center to the edge of the beam pulse. Figure courtesy A. Fedotov.

transverse collimation, momentum spread and jitter correction, and momentum painting, whereas the arc design was created for momentum tail cleaning, momentum collimation, and beam-energy characterization. Figure 31 shows a schematic layout of the ESS facility with transport lines connecting the linac to the accumulator ring and connecting the ring to the targets. Beam collimation in the transport line before ring injection is especially important for accumulators where both beam energy and beam intensity are high compared to those in RCS's.

Transverse matching usually is performed on lattice amplitude functions, dispersion functions, and their derivatives. The locations of the collimators are strategically chosen with betatron phase advance of $n\pi + \pi/2$ (n is an integer) from critical elements like extraction kickers to catch accidental beam losses due to possible mal-

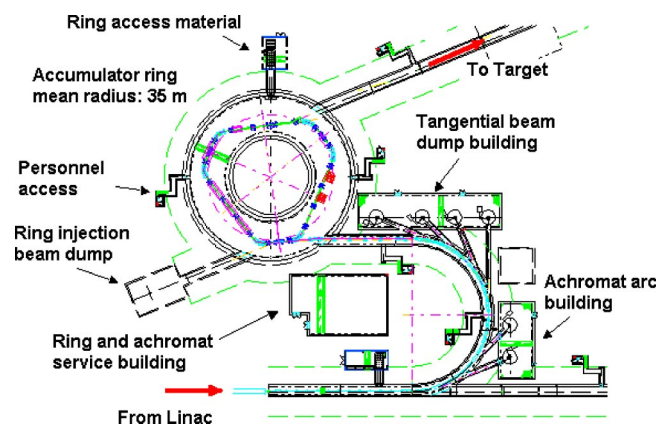


FIG. 31. (Color in online edition) Schematic layout of the ESS HEBT and Ring sections. The beam is transported from the linac (bottom) to the two vertically stacked rings through a HEBT line. The beam is collimated both transversely and longitudinally through the 180° bend (Sec. III.F). Figure courtesy ESS Council.

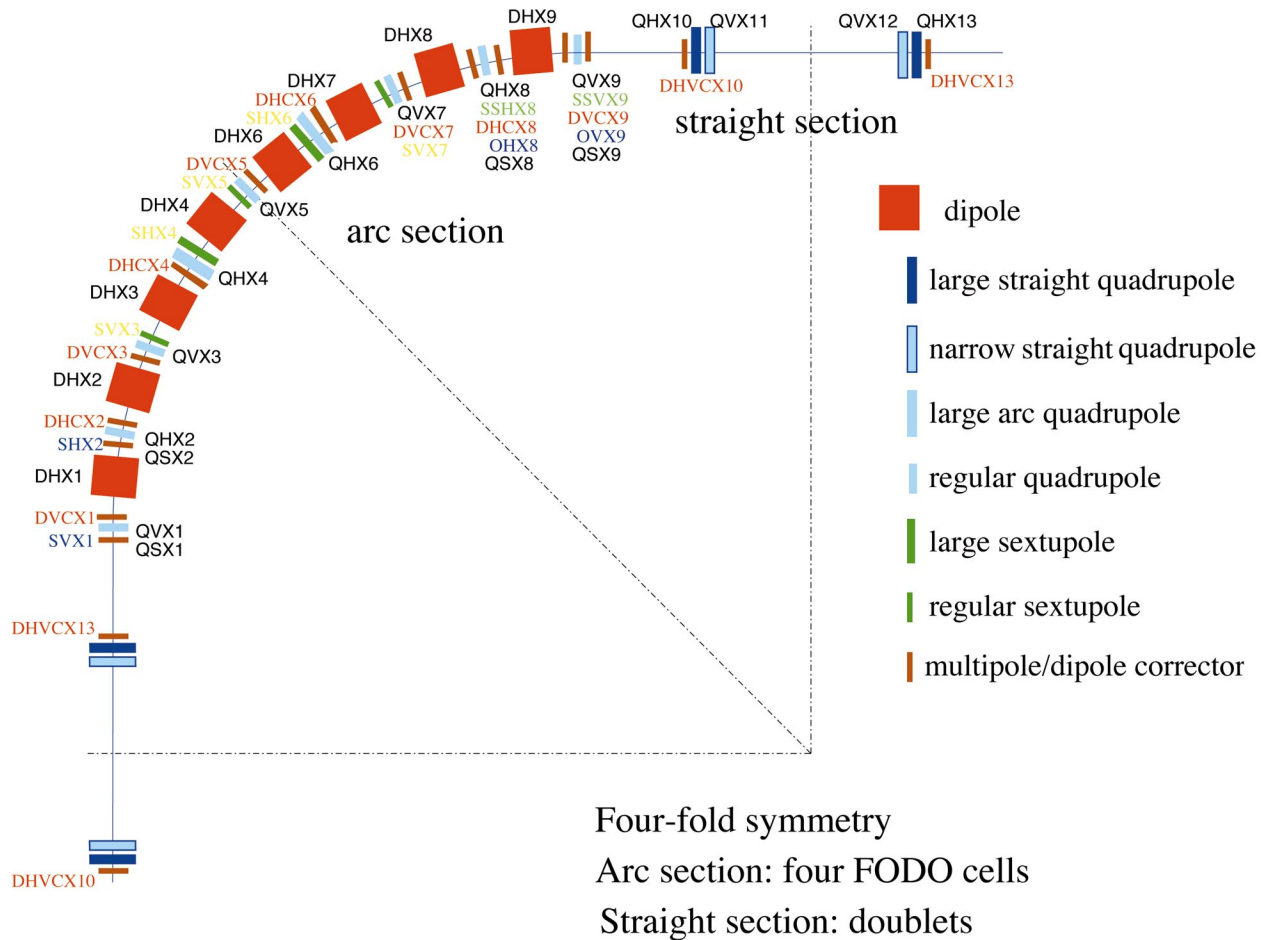


FIG. 32. (Color) Schematic layout of dipole, quadrupole, sextupole, and correctors in one superperiod of the SNS accumulator ring. The ring superperiodicity is 4 (Sec. III.G.1).

function. The transverse phase advances between the kickers and the target may be designed to be near an integer multiple of 2π , so that a kicker's error does not displace the beam at the target. For both beam dumps and beam targets, adequate beam diagnostics (harps, fast beam-loss monitors) and fast machine-protection systems are necessary.

G. Magnet system and field-error compensation

1. Magnet system

For high-intensity synchrotrons, normal-conducting magnets are preferable to superconducting magnets because of their resistance to radiation and heating (Fig. 32). Even for fixed-energy accumulators, electromagnets are preferred over permanent-field magnets for their adjustability to varying conditions of injection and operation. Most common magnets consist of a ferric core shaped in H-style, C-style, or window-frame form, and water-cooled hollow copper windings passing a current of up to several thousand amperes (Zeller, 1998). The steel core of the magnets must be laminated for rapid-cycling synchrotrons to alleviate eddy-current effects. For fixed-energy accumulator rings, laminated cores

provide good mechanical accuracy, high uniformity of material and field, and cost savings for a high-volume production.

Magnets designed for rapid-cycling synchrotrons need to meet the challenge of providing good field uniformity under a wide range of rapid field variations (up to 50 Hz). For the J-PARC 3-GeV synchrotron, the peak field of the dipole magnet is designed to be 1.4 T, and the repetition rate is 25 Hz. This combination of a high field and high repetition rate entails large eddy-current losses and current distributions unless a special water-cooled stranded conductor is used (Sasaki, 1987).

By contrast, magnets designed for accumulation operate at a fixed field. There, the focus mainly is on field uniformity and radiation resistance.

2. Magnet transfer function

Magnets typically are grouped in families and powered by common power supplies for both cost savings and magnet-to-magnet field tracking. The transfer function is defined as the ratio between the magnetic field integrated along the path of the particle to the magnet excitation current. Variations in a magnet's material properties and geometry result in variation in its transfer function, causing deviation of the beam's closed orbit

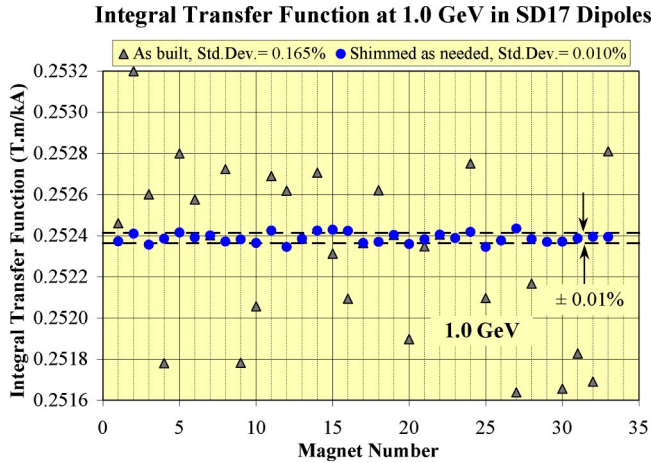


FIG. 33. (Color in online edition) Variation of integral transfer function of SNS ring's dipole magnets before and after shimming. Such large variation before shimming is mainly due to the magnet-to-magnet variation in the material of the solid steel core. The measurement current corresponds to 1 GeV beam energy (Sec. III.G.2). Figure courtesy P. Wanderer and A. Jain.

and amplitude function for dipoles and quadrupoles, respectively. With a laminated steel core, laminations produced at different production periods usually are randomized to minimize variation in material properties.

Solid steel, as opposed to laminated steel, was selected for the SNS ring's magnet cores for lower costs. Individually, field quality ($<10^{-4}$ relative error at full acceptance) is good. However, excessive (up to 0.25%) magnet-to-magnet variation is found in the dipole transfer function and its current dependence, as shown in Fig. 33. Thin (tens of μm) layers of shims are inserted at either the pole base or the back leg of the magnets to reduce the variation in transfer function below 10^{-4} for operation at the nominal energy (Wanderer *et al.*, 2002).

3. Imperfections in the magnetic field

Factors leading to imperfections in the magnetic field include the geometrical displacement of magnet components, nonuniformity in material composition, field saturation, hysteresis, eddy-current effects, ramp-induced effects, and the magnet's fringe field.

Accumulator rings are susceptible only to geometric magnetic errors and fringe-field effects. The leading components of error are those allowed by the magnet's symmetry. For a magnet of $2m$ poles ($m=1$ for dipole, $m=2$ for quadrupole magnet, and so on) the allowed multipoles are

$$2m(2k+1), \quad k=0,1,2,\dots \quad (10)$$

For a dipole magnet, such allowed multipoles are sextupole, decapole, etc. For a quadrupole magnet, the allowed harmonics are at the 12th pole, 20th pole, etc. This systematic imperfection can be corrected locally either by magnet-pole-profile shaping and shimming, or as an integral by shaping the magnet's ends (Rose, 1938; Danby *et al.*, 1999). Mechanical tolerance and material

variations produce random variation in the magnet's transfer function (defined as the ratio of the magnet field to the driving current) and random multipole errors. The effect of fringe field is discussed further in Secs. III.G.4 and IV.A.5.

Rapid-cycling synchrotrons are susceptible to time-varying effects, typically limiting the peak magnetic field to about 1.2 T and the peak ramp rate to about 50 T/s. Technical challenges are posed by the increased current density and resistive loss in the coil, as the skin depth decreases with increasing repetition rate, and due to eddy-current losses in the core material, calling for thinner lamination and lower-loss iron (Halbach, 1998; Mills, 1998). The skin depth decreases with the repetition rate according to the relation

$$\delta_s = \sqrt{\frac{2\rho_r}{\mu\omega}}, \quad (11)$$

where μ is the permeability of the conductor, and ω is the angular frequency. At a rate of 50 Hz, it is about 9 mm in copper material.

Leading sources of field imperfections are ramping eddy current and saturation. Variation in the level of saturation contributes to the tracking errors between different types of magnet. Eddy currents induced in the vacuum chamber under the changing magnetic field distort and delay the field and generate multipole errors. For a wide chamber of thickness d_w inside a dipole magnet of gap g , the sextupole field is given by (Edwards and Syphers, 1993; Rice, 1998)

$$\frac{\partial^2 B_y}{\partial x^2} = \frac{\mu_0}{\rho_r} \frac{d_w}{g} \dot{B}. \quad (12)$$

This quantity is linearly proportional to the ramp rate.

4. Magnetic fringe field

Generally, magnet fringe field refers to the longitudinal and transverse field components near the mechanical ends of the magnet, which differ both qualitatively and quantitatively from those within the body of the magnet. Effects of the transverse field component, usually a strong function of the geometry of the magnet's ends, are well represented by the formalism of magnet multipole expansion described in Sec. III.G.3. Here, the magnet's fringe field specifically refers to the longitudinal field component near the ends of a nonsolenoidal magnet as the body main field diminishes in a finite distance.

The relative impulse from the longitudinal field component on a particle's transverse momentum is approximately equal to the ratio between beam's emittance and magnet length (Wei and Talman, 1996),

$$\frac{\Delta x'_{fr}}{\Delta x'_0} \approx \frac{\epsilon_{\perp}}{L} \sqrt{\frac{1+0.75\beta'^2}{8}}, \quad (13)$$

where $\Delta x'_{fr}$ is the change of transverse momentum due to the fringe field, and $\Delta x'_0$ is the change of transverse momentum due to the main magnetic field. This effect can be significant for a high-intensity synchrotron where

the beam's emittance is intentionally increased to alleviate the space-charge force, and where the magnet typically is short. For example, the Spallation Neutron Source beam's emittance is about $240\pi \mu\text{m}$. The fringe field at each end of a 0.5-m-long quadrupole magnet produces an octupolelike transverse kick of about 5×10^{-4} relative to the main quadrupole deflection (Forest, 1998). Unlike the impulse from the transverse magnetic-field component, the impulse of the longitudinal component is independent of the geometry of the magnet's ends.

5. Magnetic interference

Magnetic interference refers to the change of magnetic field produced by an individual magnet in the presence of other nearby magnetic elements. The effect can be important when short, large-aperture magnets are used in accelerators of moderate circumferences so that magnetic end fields overlap significantly with the iron of nearby elements (Papaphilippou, Lee, and Meng, 2001). The interference usually manifests itself as a change in the magnet's transfer function and an enhancement of multipole harmonics. In the presence of magnet iron, the effects may not be obtained by a direct superposition of contributions from individual magnet elements.

In order to alleviate the amount of magnetic interference, the minimum distance between the iron of the adjacent magnets is usually chosen to be the diameter of the opening of the magnet poles. Measurements and modeling are needed to evaluate the effects under operational conditions. For magnets powered by a common power supply, trim magnet coils and trim power supplies are sometimes needed to compensate for the effect of the variation in the magnet's transfer functions.

6. Correction system

Magnet imperfections can cause deviation of the beam's closed orbit, variations in its envelope, transverse coupling, chromaticity variations, spread of tune shifts, and resonance excitation. Typically, the relative strength of the multipole field errors need to be controlled at a 10^{-4} level for lattice dipoles and quadrupoles, at a 10^{-3} level for transfer-line magnets, low-field chicane magnets, and chromaticity sextupoles, and at a 10^{-2} level for correction magnets.

Closed-orbit deviations are corrected by minimizing the beam's displacements at locations of beam position monitors (BPM) using dipole correctors preferably sited at places of peak beam amplitude (β) function. The correction can be made either globally, using orbit-response-matrix analysis, or locally, using closed-orbit bumps. Ideally, several BPM's and correctors are needed in each betatron wavelength. To prevent radiation damage, the electronic elements must be located at areas of low radioactivity outside the accelerator tunnel. Closed-orbit correction during rapid acceleration often requires dynamic correction. Rings using combined-function gradient dipole magnets usually need separate correction elements.

Trim quadrupoles can correct deviations in the beam's envelope. Correction is based on measuring and evaluating the lattice amplitude function β_{\perp} and the betatron phase advance using some of the following methods: (1) measuring tune dependence on variations in quadrupole strength to determine β_{\perp} , especially at locations of large amplitude (focusing quadrupole). However, the method is susceptible to magnet hysteresis and coupling; (2) measuring the betatron envelope after perturbing the beam transversely to determine the relative value of β_{\perp} ; and, (3) assessing the betatron phase at the BPM locations after resonantly perturbing the beam at the betatron frequency, determining β_{\perp} especially at small-amplitude locations.

Coupling in transverse motion originating from skew quadrupole error components, space-charge effects, and solenoidal fields usually is enhanced by near-equal horizontal and vertical working points in tune space. The typical coupling strength is proportional to the quantity

$$\sum_i a_{2,i} \sqrt{\beta_{x,i} \beta_{y,i}} \sin(\psi_{x,i} - \psi_{y,i}), \quad (14)$$

where the subscript i indicates the source of error, ψ_x and ψ_y are the horizontal and vertical betatron phases, and a_2 is the strength of the skew quadrupole error (Edwards and Teng, 1973; Peggs, 1983). The effect of systematic skew quadrupole errors usually can be alleviated by splitting the horizontal and vertical tunes by at least half a unit, so that variations in phase difference results in randomization [Eq. (14)]. Global decoupling is attained by at least two families of skew quadrupoles to reduce the minimum tune splitting. Local decoupling is performed by analyzing turn-by-turn data from dual-plane BPM's, and correcting with multiple skew quadrupole correctors.

Control of chromaticity is necessary for rings operating above transition energy to avoid the head-tail instability, and it is also desirable for rings operating below (Sec. IV.A.2). For rings operating solely below transition, chromatic sextupoles, arranged according to lattice symmetry and powered in multiple families, offer control of tune spread, damping of instability, and matching of off-momentum optics. The SNS ring uses four-family chromatic sextupole magnets located in high-dispersion regions, complemented by resonance-correction sextupole windings placed in zero-dispersion regions (Tsoupas, Gardner, *et al.*, 2000).

Resonance correction has been used successfully on several machines, including the CERN PS and the Brookhaven AGS and AGS Booster (Schindl, 1979). The principle is summarized in Sec. IV.A.7. At the AGS Booster, resonance correction up to normal and skew sextupole was essential during high-intensity operations (Fig. 34; Gardner *et al.*, 1994).

H. Vacuum chamber and shielding

The vacuum chamber through which the circulating beam passes provides an environment intended to re-

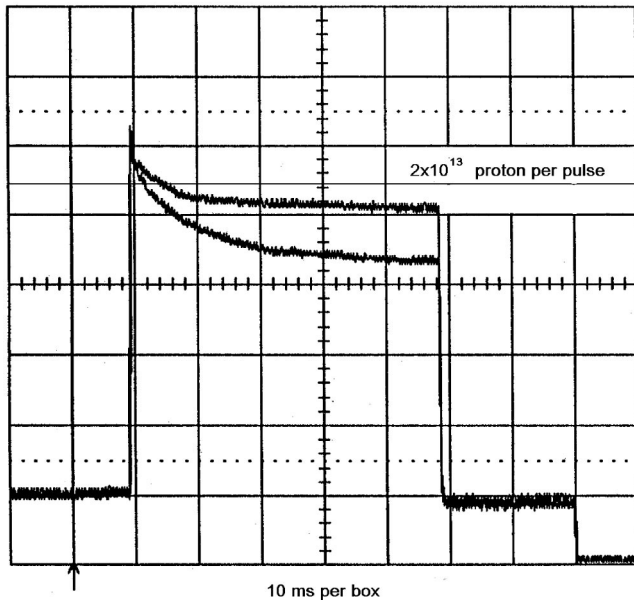


FIG. 34. Increase of beam survival with sextupole resonance correction in the AGS Booster: x , 10 ms per box; y , 2×10^{13} particle per pulse at flat top. Resonance correction up to normal and skew sextupole was essential during high-intensity operations (Sec. III.G.6). Figure courtesy C. Gardner.

duce the effects of residual gas scattering and, in the case of an H^- beam, to lower electron stripping. For high-intensity proton synchrotrons, the high beam current can drive gas ions into the chamber's walls, leading to positive feedback and pressure runaway, unless the ion-induced desorption coefficient is kept below a threshold value (Gröbner and Calder, 1973). In addition, the enclosure offers a conducting surface to carry the induced current so that the coupling impedance is minimized.

In time-varying magnetic fields, the vacuum enclosure must accommodate several factors: (1) thermal heating from the eddy current generated by the varying field in a resistive material; (2) the delay of rise time of the magnetic field inside the chamber; and (3) the continuous passage of beam-image current. Conventionally, the vacuum chamber is either made of a metallic pipe (stainless steel or aluminum) or is directly formed from the magnet pole faces (as in the FNAL Booster). For rapid-cycling synchrotrons, the vacuum chambers need to be rf shielded to give high impedance to the eddy current but low impedance to the induced current. Consider a pipe of thickness d_w and volume resistivity ρ_r . As an example, for a resistive loop of width w_r and height h_r penetrated by a magnetic field B , the instantaneous power per unit length is given by (Henderson, 1998)

$$\frac{dP_r}{ds} = \frac{B^2 w_r^2 h_r d_w}{2\rho_r}. \quad (15)$$

For a circular pipe of radius b , the average power is proportional to the repetition rate, the field variation

rate, the magnetic-field amplitude squared, and the pipe's radius b cubed. It also is inversely proportional to the sheet resistivity ρ_r/d_w .

ISIS adopted ceramic chambers with supported internal stainless-steel wires, interrupted with ceramic-chip capacitors to allow the passage only of beam image charge at high frequency (Boardman, 1982). The wires are contoured according to the design beam's envelope, reducing the beam coupling impedance. For newly proposed synchrotrons of much higher beam power, the main concern with this approach is the failure of the wires and the consequent unavailability of the machine. Other candidates include a ceramic chamber with printed, internal silver wires (KAON factory, SNS RCS), external shielding and internal coating (J-PARC), and an extra-thin Inconel chamber of high mechanical strength (FNAL PD; see KAON, 1990; FNAL PD, 2000; Wei, Beebe-Wang, *et al.*, 2000). Figure 35 shows the circular vacuum chamber used in the straight section of the 3-GeV synchrotron of the J-PARC project (Kinsho *et al.*, 2002).

For both rapid-cycling synchrotrons and accumulators, ceramic vacuum-chambers are often used to allow fast programming of trim quadrupole and dipole correction fields. Such chambers also are used in the injection region to accommodate the fast programming of bump magnet fields for phase-space painting.

I. Beam diagnostics and machine protection

Beam diagnostics are essential to commissioning and operating a high-intensity synchrotron, not only for monitoring and controlling the beam but, equally important, as an integral part of a machine protection system. Beam-loss monitors with a fast response (typically tens of ns) are located at critical locations to instantaneously detect machine malfunction. The machine protection system, linked with critical diagnostics systems and power supplies for critical elements (e.g., dipole magnets, injection bump magnets, extraction kicker magnets), is designed to immediately shut off subsequent beam pulses after detecting the failure of a critical device. Elements that are susceptible to beam loss upon system malfunction (e.g., collimators, bellows) are designed to withstand at least one full beam pulse.

Multiturn injection is a complex dynamic process during which the beam's intensity can increase by three orders of magnitude, and the transverse beam size can grow by several tens of times. The diagnostics instrumentation must possess a wide range of sensitivity and turn-by-turn capability to monitor the beam's intensity (beam current monitors), position (beam position monitors), transverse and longitudinal profiles (ionization-profile monitor, wire-profile monitor, luminescence-profile monitor, wall-current monitor), and beam loss (loss monitor). Dual-plane beam position monitors are needed at all critical areas for monitoring orbit and local decoupling.

Credible measurement of the turn-by-turn evolution of the beam profile is difficult to obtain in a high-

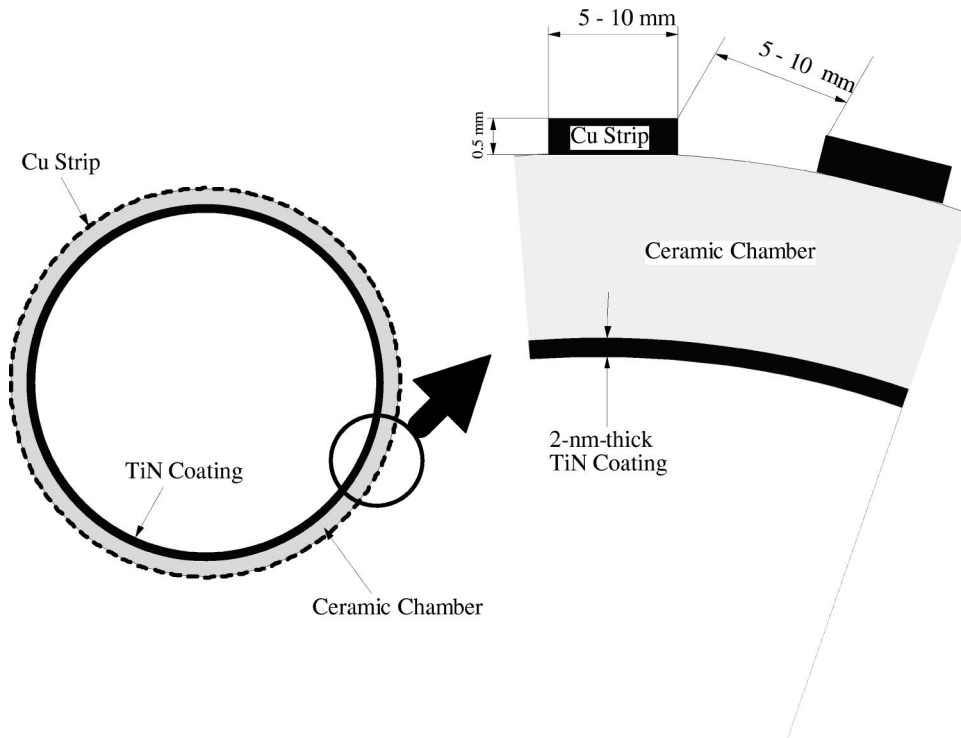


FIG. 35. Schematic view of the ceramic vacuum chamber and the rf shield of the 3-GeV synchrotron of the J-PARC project (Sec. III.H). The 5–6-mm-thick chamber wall is made of 99.8% high-purity alumina. Figure courtesy M. Kinsho.

intensity ring. One candidate is the ionization-profile monitor (IPM), which measures the distribution of electrons freed by ionizing collisions of the beam with the residual gas in the beam line (DeLuca, 1969; Connolly *et al.*, 1999). The IPM's performance is anticipated to be complicated by the presence of an electron cloud in the vacuum pipe (Sec. IV.D). The IPM designed for the SNS ring uses a magnetic field to collect ionized electrons, instead of ions, to avoid signal broadening due to the space-charge force (Fig. 36). Sweeping electrodes are used, and the multichannel plates for electron collection are recessed from the vacuum chamber wall to avoid superfluous signals. Three electromagnets are used in

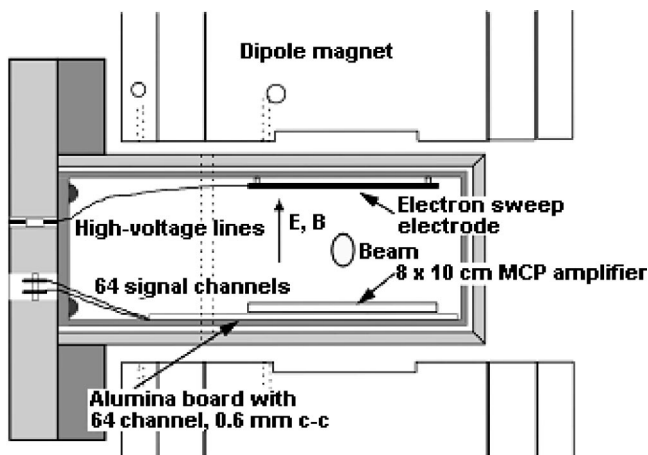


FIG. 36. A cross section of the ionization-profile monitor for the SNS ring. Sweeping electrodes are used, and the multichannel plates for electron collection are recessed from the vacuum-chamber wall to avoid superfluous signals (Sec. III.I). Figure courtesy R. Connolly.

each transverse direction to minimize optical perturbation and to maintain operational robustness. Another alternative for turn-by-turn profile measurement is the luminescence-profile monitor that was successfully tested at the CERN SPS (Burtin *et al.*, 2000).

An understanding of the beam's behavior in the presence of space charge and coupling impedance entails measuring the beam halo. With recently designed synchrotrons, the measurement can be made by detecting the extent of beam loss scattered by the adjustable scrapers. For accumulator rings, the residual beam in the beam gap needs to be measured on a submicrosecond time scale, preferably at a level of 10^{-5} of the peak beam density.

With electron-cloud effects playing an increasing role in high-intensity rings, measurement of electron density and the energy spectrum becomes important. From experience gained at PSR, the SNS implemented electron detectors at locations where significant beam loss and electron concentration is expected (e.g., near injection foil, scrapers, and collimators; Fig. 37). Fourier-transform analysis of high-harmonic betatron-sideband signals from a wideband beam position monitor is another technique that may be applicable to diagnosing electron-proton interactions.

All time- and frequency-domain diagnostics become considerably complicated in rapid-cycling synchrotrons due to the fast changes in the beam's velocity.

IV. BEAM DYNAMICS: INTENSITY-LIMITING MECHANISMS

In this section, several beam dynamics topics are discussed, emphasizing mechanisms that potentially limit

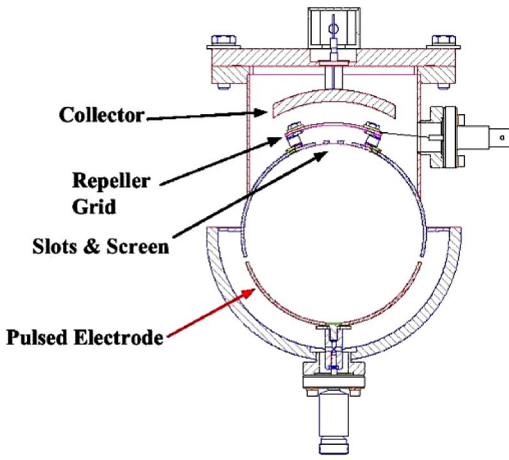


FIG. 37. (Color in online edition) Electron sweeping detector developed at the LANL PSR (Sec. III.I). The pulsed electrode sweeps electrons towards the open slots. The grounded screen shields the collector from signals induced by the passage of the proton beam. The repeller grid is used for the analysis of electron energy (see Fig. 47). The collector is electrically biased to prevent the escape of secondary electrons. Figure courtesy A. Browman.

the intensity of the beam in synchrotrons. In a proton synchrotron, the frequency of longitudinal oscillation usually is several orders of magnitude smaller than the transverse oscillation frequency. The transverse and longitudinal dynamics often may be treated separately.

A. Transverse tune shifts and resonances

Tune is defined as the number of oscillation cycles that a particle executes in one revolution around the ring’s circumference. The spread of transverse tune shift in a beam is an important characterization that determines nonlinear resonance behavior and the beam’s stability. As an example, Table II lists the tune shifts produced by various mechanisms in the SNS accumulator

TABLE II. Tune shift produced by various mechanisms on a 2-MW beam in the SNS ring with transverse emittance of $120\pi \mu\text{m}$ in each plane and momentum spread of $\pm 0.7\%$ (Sec. IV.A).

Mechanism	Maximum tune shift
Space charge	-0.2 (2 MW beam)
Chromaticity	± 0.06 ($0.7\% \Delta p/p$)
Kinematic nonlinearity (480π)	0.001
Fringe field (480π)	± 0.025
Uncompensated ring magnet error (480π)	± 0.02
Compensated ring magnet error (480π)	± 0.002
Fixed injection chicane	± 0.004
Injection painting bump	± 0.001
Electron cloud	~ 0.04

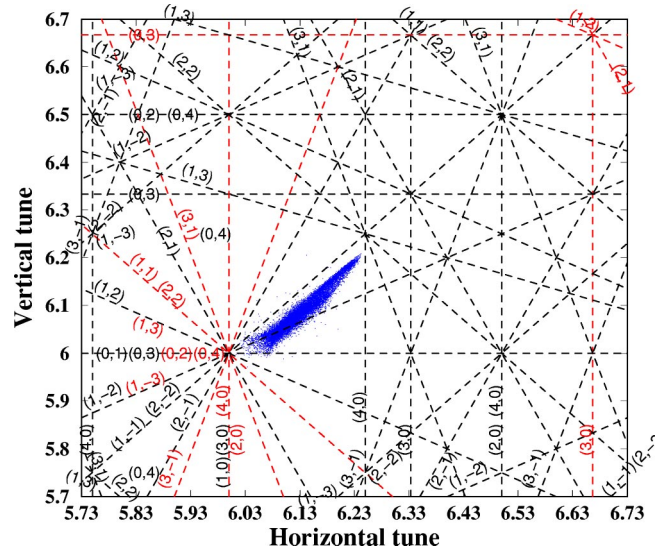


FIG. 38. (Color in online edition) Transverse tune spread of proton beams at intensity of 2×10^{14} at the end of injection in the SNS accumulator ring. The transverse tunes are (6.23, 6.20). The beam has a full, unnormalized total transverse emittance of $240\pi \mu\text{m}$ and a full momentum deviation of $\pm 0.7\%$. Computer simulation is performed with UAL/ORBIT package. Effects of space charge, transverse painting, natural chromaticity, kinematic nonlinearity, fringe field, and magnetic manufacturing imperfections are included (Sec. IV.A). Figure courtesy Y. Papaphilippou.

ring, including space charge, natural chromaticity, and magnet imperfection. The amount of tune shift indicates its relative impact on the beam. In general, tune shifts from the ideal design value are due to changes in the effective strength of focusing on the particles (Courant and Snyder, 1958):

$$\Delta \nu = -\frac{1}{4\pi} \oint \beta_{\perp} \Delta K_{\perp} ds, \quad \Delta K_{\perp} = \frac{\partial B_y / \partial x}{B_0 \rho}, \quad (16)$$

where $B_0 \rho$ is the rigidity of the beam. When the perturbation in the amplitude function β_{\perp} is relatively small, tune shifts due to various mechanisms may be superimposed according to their dependence on the particles’ oscillation amplitude and momentum deviation. More accurately, computer tracking and frequency analysis can be used. Figure 38 shows an example of the transverse tune spread of a high-intensity proton beam in the SNS accumulator ring (Malitsky, Smith, and Talman, 1999; Fedotov, Gluckstern, and Wei, 2001; Papaphilippou, 2001).

1. Space-charge tune shift

Space charge is a fundamental limitation in high-intensity circular accelerators. The amount of tune shift is linearly proportional to the product of the linear particle density and the ring’s circumference (i.e., proportional to the total number of particles in the ring for a given bunching factor). The space-charge effect is drastically alleviated at higher beam energy when the transverse space-charge forces produced by the electric and

magnetic forces tend to cancel each other. The on-axis, incoherent tune spread due to the space-charge self-field is approximated by

$$\Delta\nu_{x,y} = -\frac{f_{sc}N_0r_0R_0}{2\pi B_f\nu_{x,y,0}\beta^2\gamma}\left[\frac{1}{\sigma_{x,y}(\sigma_x+\sigma_y)}\left(\frac{1}{\gamma^2}-\eta_e\right)+A_{im}^e(\gamma^{-2}-\eta_e)+A_{im}^m\right], \quad (17)$$

where $r_0=e^2/4\pi\epsilon_0m_0c^2$ is the classical radius of a proton, $2\pi R_0$ is the ring circumference, and σ_x and σ_y are the horizontal and vertical rms beam size. The bunch form factor f_{sc} is equal to 1/2 for a uniform distribution, and to 1 for a Gaussian distribution. The bunching factor $B_f\leq 1$ is the ratio between the average and the peak beam density. The neutralization factor η_e , defined as the electron-to-proton density ratio in the laboratory frame, represents the contribution of an electron cloud of low energy (typically up to several hundred eV). The contribution from the electric and magnetic images of the beam are represented by the Laslett tune shifts A_{im}^e and A_{im}^m , respectively. The electric fields due to both the direct space charge and the image charge are reduced by the neutralization (Laslett, 1963; Zotter and Kheifets, 1998). For both incoherent and coherent space-charge tune shifts, the relative contribution of the electron cloud to the direct space charge and electric image is $-\gamma^2\eta_e$.

For a round beam with no neutralization, the direct space-charge tune shift becomes

$$\Delta\nu_{sc}\approx\frac{f_{sc}N_0r_0}{4\pi B_f\epsilon_{rms}\beta^2\gamma^3}, \quad (18)$$

where $\epsilon_{rms}=\sigma_{\perp}^2/\beta_{\perp}$ is the rms emittance, and the relation used is

$$\beta_{\perp}\approx R_0/\nu_0. \quad (19)$$

The Laslett tune shift, contributed by the electric and dc as well as ac magnetic images of the beam, depends on the beam's surrounding environment (Zotter and Kheifets, 1998). It usually perturbs the cancellation between the electric and magnetic forces. Compared with the direct space-charge force, the contribution of the image field can become important at higher energies. The lattice dispersion effectively increases the transverse beam's size and reduces the space-charge tune shift.

Rings are designed to avoid strong resonances, using a formula for the incoherent space-charge tune shift based on assuming a constant beam size. Taking into account the beam's coherent-oscillation modes, the resonance condition actually is (Smith, 1963; Sacherer, 1968; Baartman, 1998)

$$\frac{k}{l}=\nu_0-C_l\Delta\nu_{sc}, \quad (20)$$

where ν_0 is the base tune, $\Delta\nu_{sc}$ is the incoherent space-charge tune shift of an rms-equivalent uniform-density beam, k is the excited harmonic, l is the resonance order, and the deviation of the coefficient C_l from 1 rep-

resents the contribution of envelope oscillations. This contribution is most significant for low-order resonances (Gluckstern, 1970; Hofmann, 1998). For a round beam near a half-integer resonance ($l=2$), when the horizontal and vertical tunes are close to one other, $C_2=1/2$ for the symmetric mode, and $C_2=3/4$ for the antisymmetric mode. In the case of split tunes, $C_2=5/8$. For the SNS ring at the split-tune working point with $\Delta\nu_{sc}\approx 0.15$, the effective tune shift is $\Delta\nu_{eff}=5\Delta\nu_{sc}/8=0.09$. Therefore the actual space-charge limit is less restrictive (Fedotov and Hofmann, 2002).

2. Chromatic tune shift

Variation of transverse focusing with beam energy generates the chromatic tune shift, which usually is expressed in terms of the chromaticity ξ_{\perp} as

$$\Delta\nu_{\perp}=\xi_{\perp}\frac{\Delta p}{p}, \quad (21)$$

where $\Delta p/p$ is the relative momentum deviation of the particle. A linear lattice (consisting of dipole and quadrupole magnets only) with moderate focusing usually results in a negative, "natural" chromaticity of a value near the transverse tune (Courant and Snyder, 1958); negative chromaticity is necessary for damping instabilities below transition (Chao, 1993).

Existing rings, like the ISIS and PSR, which accelerate or accumulate the beam solely below transition energy, may operate without chromaticity control. For newly designed high-intensity rings, chromatic tune spread often becomes significant when instability damping demands a large, sometimes intentionally broadened beam-momentum spread. Then, sextupole magnets are used to adjust chromaticity. The nonlinearity they introduce often causes a strong dependence of the machine's chromaticity on momentum deviation $\Delta p/p$. The SNS uses four-family chromatic sextupole magnets to control chromatic tune shift across the entire range of momentum (Tsoupas, Gardner, *et al.*, 2000).

3. Kinematic tune shift

Kinematic nonlinearities refer to effects stemming from the fact that the classical relativistic Hamiltonian contains terms higher than quadratic order of canonical momentum. The leading order in tune shift has an octupolelike dependence on the particle's transverse action as (Wan, 1999; Papaphilippou and Abell, 2000)

$$\Delta\nu_{x,y}=\frac{1}{4\pi}\left[\frac{3\epsilon_{x,y}}{8}\int\gamma_{x,y}^2ds+\frac{\epsilon_{y,x}}{4}\int\gamma_x\gamma_yds\right], \quad (22)$$

where $\gamma_{x,y}$ are the Courant-Snyder lattice functions. For high-intensity synchrotrons, the tune shift can become noticeable, especially at the end of injection when the beam's emittance is large. For the SNS ring, the tune shift is about 10^{-3} at a full acceptance of $480\pi\mu\text{m}$.

4. Magnetic imperfections

Quadrupole errors cause tune shifts and tune coupling for the entire beam. Sextupole and higher-order multipoles produce tune shifts that depend on the particles' action (Wei and Harrison, 1992). The effects of even-order multipoles (quadrupole, octupole, etc.) can be directly assessed from the amount of tune shift produced—tune shift that is linearly proportional to the strength of the source. Multipoles of odd order (sextupole, decapole, etc.) do not produce first-order tune shifts; their impact may be evaluated by second-order tune shift analysis, dynamic aperture tracking, and resonance analysis.

In general, the two-dimensional magnetic field in a magnet can be expressed in terms of the multipole expansion

$$B_y + jB_x = B_0 \sum_{n=0}^{\infty} (b_n + ja_n)(x + jy)^n, \quad (23)$$

where B_0 is the nominal field, and b_n and a_n are the normal and skew multipole components, respectively. To the first order of the error strengths a_n and b_n , retaining terms up to order 9 (20th-pole), the tune shifts are given by

$$\begin{aligned} \Delta\nu_x = & \left(-\frac{\Delta b_0}{2\rho} + \frac{b_0\delta}{2\rho} - C_1 \right) \beta_x + 3C_2\beta_x^2\epsilon_x - 6C_2\beta_x\beta_y\epsilon_y \\ & + \frac{15}{2}C_3\beta_x^3\epsilon_x^2 - 45C_3\beta_x^2\beta_y\epsilon_x\epsilon_y + \frac{45}{2}C_3\beta_x\beta_y^2\epsilon_y^2 \\ & + \frac{35}{2}C_4\beta_x^4\epsilon_x^3 - 210C_4\beta_x^3\beta_y\epsilon_x^2\epsilon_y + 315C_4\beta_x^2\beta_y^2\epsilon_x\epsilon_y^2 \\ & - 70C_4\beta_x\beta_y^3\epsilon_y^3 + \frac{315}{8}C_5\beta_x^5\epsilon_x^4 - \frac{1575}{2}C_5\beta_x^4\beta_y\epsilon_x^3\epsilon_y \\ & + \frac{4725}{2}C_5\beta_x^3\beta_y^2\epsilon_x^2\epsilon_y^2 - 1575C_5\beta_x^2\beta_y^3\epsilon_x\epsilon_y^3 \\ & + \frac{1575}{8}C_5\beta_x\beta_y^4\epsilon_y^4, \end{aligned} \quad (24)$$

$$\begin{aligned} \Delta\nu_y = & C_1\beta_y + 3C_2\beta_y^2\epsilon_y - 6C_2\beta_x\beta_y\epsilon_x - \frac{15}{2}C_3\beta_y^3\epsilon_y^2 \\ & + 45C_3\beta_x\beta_y^2\epsilon_x\epsilon_y - \frac{45}{2}C_3\beta_x^2\beta_y\epsilon_x^2 + \frac{35}{2}C_4\beta_y^4\epsilon_y^3 \\ & - 210C_4\beta_x\beta_y^3\epsilon_x\epsilon_y^2 + 315C_4\beta_x^2\beta_y^2\epsilon_x^2\epsilon_y - 70C_4\beta_x^3\beta_y\epsilon_x^3 \\ & - \frac{315}{8}C_5\beta_y^5\epsilon_y^4 + \frac{1575}{2}C_5\beta_x\beta_y^4\epsilon_x\epsilon_y^3 \\ & - \frac{4725}{2}C_5\beta_x^2\beta_y^3\epsilon_x^2\epsilon_y^2 + 1575C_5\beta_x^3\beta_y^2\epsilon_x^3\epsilon_y \\ & - \frac{1575}{8}C_5\beta_x^4\beta_y\epsilon_x^4, \end{aligned} \quad (25)$$

where

$$\begin{aligned} C_1 &= \frac{1}{2}(\Delta b_1 - b_1\delta) + b_2\Delta_x - a_2\Delta_y + \frac{3}{2}(b_3\Delta_x^2 - a_3\Delta_y^2), \\ C_2 &= \frac{1}{2}\left(\frac{1}{4}b_3 + b_4\Delta_x - a_4\Delta_y\right), \\ C_3 &= \frac{1}{4}\left(\frac{1}{6}b_5 + b_6\Delta_x - a_6\Delta_y\right), \\ C_4 &= \frac{1}{8}\left(\frac{1}{8}b_7 + b_8\Delta_x - a_8\Delta_y\right), \\ C_5 &= \frac{1}{16}\left(\frac{1}{10}b_9 + b_{10}\Delta_x - a_{10}\Delta_y\right), \end{aligned} \quad (26)$$

and

$$\Delta_x = D_x \frac{\Delta p}{p} + x_c, \quad \Delta_y = D_y \frac{\Delta p}{p} + y_c. \quad (27)$$

5. Magnetic fringe field

As discussed in Sec. III.G.4, the relative impulse on a particle's transverse momentum is proportional to the ratio between beam emittance and the magnet length (Wei and Talman, 1996; Papaphilippou, Wei, and Talman, 2003). For a magnet with a transverse-field multipole component of n th order, the contribution from the fringe field, corresponding to a multipole of leading order $(n+2)$, is weakly dependent on the detailed geometry of the magnet's end. For quadrupole magnets, the fringe fields produce octupole terms that contribute to the tune shifts (Papaphilippou and Abell, 2000)

$$\begin{aligned} \Delta\nu_x &= \frac{\pm}{16\pi} \sum_i K_{\perp,i} [-\beta_{x,i}\alpha_{x,i}\epsilon_x + (\beta_{x,i}\alpha_{y,i} - \beta_{y,i}\alpha_{x,i})\epsilon_y], \\ \Delta\nu_y &= \frac{\pm}{16\pi} \sum_i K_{\perp,i} [\beta_{y,i}\alpha_{y,i}\epsilon_y + (\beta_{x,i}\alpha_{y,i} - \beta_{y,i}\alpha_{x,i})\epsilon_x], \end{aligned} \quad (28)$$

where the summation is over all quadrupole ends indicated by the subscript i , K_{\perp} is the strength of the quadrupole's main field, and the $+$ (or $-$) sign applies to the entrance (or exit) end of the magnet. For dipole magnets, the fringe field produces to leading order a sextupole term that again contributes to octupole-like amplitude detuning that is second order in strength.

Accurate modeling of 3D magnetic field is performed with computer codes like TOSCA3D (OPERA, 2002). Fringe-field dynamics can be quantitatively studied with map representations using computer codes like COSY (Makino and Berz, 1999) and MARYLIE (Dragt *et al.*, 1999).

6. Electron cloud

An electron cloud tends to neutralize the positive charge of the proton beam. Compared to the space-charge tune shift between the protons, the tune shift produced by the electron cloud is enhanced by a factor γ^2 due to absence of the compensating magnetic force in the laboratory frame [Eq. (17)]. As discussed in Sec.

TABLE III. Estimated controlled loss of a proton beam at 1 GeV in the SNS ring, linac-to-ring transport (HEBT), and ring-to-target transport (RTBT) (Sec. IV.B.1). Losses are given as a fraction of the total beam intensity. The total beam power is 2 MW.

Mechanism	Location	Fraction	Power
HEBT:			
H ⁰ from linac	linac dump	10 ⁻⁵	20 W
linac transverse tail	HEBT H/V collimator	10 ⁻³	2 kW
energy jitter/spread from linac	HEBT L collimator	10 ⁻³	2 kW
Ring:			
beam-in-gap	BIG kicker/collimator	10 ⁻⁴	200 W
excited H ⁰ at foil	collimator	1.3×10 ⁻⁵	26 W
partial ionization at foil	injection dump	10 ⁻²	20 kW
foil miss	injection dump	10 ⁻²	20 kW
ring beam halo	collimator	1.9×10 ⁻³	3.8 kW
energy straggling at foil	collimator	3×10 ⁻⁶	6 W
RTBT:			
kicker misfiring	RTBT collimator	10 ⁻⁵	20 W

IV.D, the effects can be serious resonance crossing and beam loss. Take a 2-MW beam in the SNS ring as an example. The peak tune shift due to space charge is about -0.2 . Assume that the neutralization level is 10% ($\eta_e \approx 0.1$) inside the proton beam for trailing-edge particles at 50% of the peak's longitudinal density. Then, the tune shift due to electron cloud is about $+0.04$ [Eq. (17)].

7. Resonance effects and correction

The transverse resonance condition is given by the relation

$$m\nu_x + n\nu_y = k, \quad (29)$$

where ν_x and ν_y are the horizontal and vertical tunes, and m , n , and k are integers. If m and n have the same signs, the resonance is called a sum resonance, and if they have opposite signs it is called a difference resonance. The order, l , of the resonance is

$$l = |m| + |n|. \quad (30)$$

The strength of the resonance is characterized by the quantity

$$\kappa = \frac{R_0}{\pi 2^l m! n!} \oint \beta_x^{|m/2|} \beta_y^{|n/2|} K_{\perp}^{(l)} \exp(i\Psi) d\theta, \quad (31)$$

where $K_{\perp}^{(l)}$ is the strength of the error field. It is given by

$$K_{\perp}^{(l)} = \frac{1}{B_0 \rho} \left(\frac{\partial^{(l-1)} B_i}{\partial x^{(l-1)}} \right), \quad (32)$$

with $B_i = B_y$ for a normal magnetic field (i.e., n even) and $B_i = B_x$ for a skew field (n odd). The integral is over the azimuthal angle $\theta = s/R$, and the phase ψ satisfies $\psi \approx k\theta$ when the tunes are near resonance. The resonance is excited by the k th harmonic of θ by the error component of $2l$ -pole. In the vicinity of the resonance line, particle motion becomes unstable. The size of the “stop band” is given by (Schoch, 1958; Guignard, 1975)

$$\Delta\nu^{(m,n)} = \pm |\kappa| \epsilon_x^{|m/2|} \epsilon_y^{|n/2|} \left(\frac{m^2}{\epsilon_x} + \frac{n^2}{\epsilon_y} \right). \quad (33)$$

For systematic field errors, the major resonances are so-called structure resonances that occur when k is an integral multiple of the lattice superperiodicity M . Resonance correction is based on minimizing κ [Eq. (31)] using correctors of the appropriate order located at strategic positions of azimuth θ to generate the intended harmonics.

B. Beam-loss mechanisms

1. Controlled beam loss

Beam loss is categorized into two classes: controlled and uncontrolled. Controlled beam loss includes the beam reaching the beam dump and also striking the collimators, both located in shielded regions. As an example, Table III lists the expected controlled beam loss in the SNS accumulator ring and the transports, including the beam's tail and residual from the linac, the H⁻ beam missing or escaping the stripping-foil reaching the injection beam-dump, the beam halo generated in the ring, energy straggling at the foil, and loss due to the kicker's misfiring (Catalan-Lasheras, Lee, *et al.*, 2001).

The beam dump and collimators must withstand the effects of the beam's high power, power density, and repetition rate. Mechanical analyses with computer simulation programs like ANSYS and performance tests of prototypes are essential, including their resistance to thermal, radiation, and mechanical stresses, vacuum outgassing, vacuum leakage, and long-term fatigue (ANSYS, 2003). An example is the window to the beam dumps that separates the accelerator vacuum from the atmosphere. A plasma window was proposed as an alternative to the conventional water-cooled Inconel window, to reduce beam loss and to avoid having to use radioactive water for cooling (Hershcovitch, 1995; Raparia and Hershcovitch, 2002).

TABLE IV. Estimated uncontrolled loss of a proton beam at 1 GeV in the SNS ring, linac-to-ring transport (HEBT), and ring-to-target transport (RTBT) (Sec. IV.B.2). Losses are given as a fraction of the total beam intensity distributed in the specified machine length. The total beam power is 2 MW.

Mechanism	Location	Fraction	Length (m)	Power (W/m)
HEBT:				
H ⁻ magnetic stripping	all HEBT	1.7×10^{-6}	169	0.02
collimator outscattering	HEBT achromat	7.5×10^{-6}	15	0.1
Ring:				
H ⁻ magnetic stripping	injection dipole	1.3×10^{-7}	1	0.3
nuclear scattering at foil	foil	3.7×10^{-5}	30	2.5
collimation inefficiency	all ring	10^{-4}	218	0.9
RTBT:				
nuclear scattering at window	target window	4×10^{-2}		

2. Uncontrolled beam loss

Uncontrolled beam loss falls into two categories: those losses linearly proportional to the beam's intensity (e.g., Coulomb scattering and nuclear scattering at the injection foil, magnetic stripping, gas scattering, kicker malfunction, noises from the rf system and the magnet power-supply system) and those losses that grow progressively with intensity (e.g., space-charge-induced tune spread and coherent resonance crossing, instability, electron-cloud effects). Table IV lists some known mechanisms and the expected level of loss (Catalan-Lasheras, Galambos, *et al.*, 2001). As a design guideline for hands-on maintenance, the average beam loss must be under 1 W per meter. That translates into a level of radioactivation of approximately 1 mSv/h (100 mrem/h), measured at 30 cm from the surface, 4 h after the machine is shut down (Wangler, 1998; Mokhov and Chou, 1999). Computer simulations with programs like MCNP and MARS are often used to determine the transport of the primary and secondary particles through the surrounding material and to estimate the level of radioactivation and needed protection (Mokhov, 1995; MCNP, 2002).

3. Resonance-loss model

The beam intensity achievable in synchrotrons ultimately is limited by the uncontrolled beam loss. Beam-loss models predict the time structure of the loss and the maximum intensity that can be stored in the ring. By monitoring various mechanisms of loss, one can explore the operational potential, optimize the working point, and design resonance correction.

Figure 39 shows, at a typical optimized working point, the dependence of fractional beam loss on the beam's intensity in the SNS accumulator ring. The results were obtained with computer modeling of macroparticles simulating the injection-painting process, the space-charge forces, the coupling impedance, magnetic-field errors, the magnetic fringe field, and kinematic nonlinearity (Galambos *et al.*, 1999; Malitsky *et al.*, 1999). Below a tune range of about 0.15, weak resonance crossing

mostly contributes to the constant fractional beam loss in the absence of chromatic and nonlinear correction, while foil scattering of the circulating beam is a major factor during the injection. Compared with the uncontrolled loss measured at the PSR accumulator ring (Fig. 40), injection loss is low due to detailed transverse painting both horizontally and vertically. As the intensity increases, beam loss increases progressively upon overlapping with the half-integer coherent-resonance lines (Fedotov, Blaskiewicz, *et al.*, 2002). Depending upon operational conditions, the behavior of the loss curve varies with the choice of working point, the nature and excitation of nearby resonance lines, and the correction of major resonances.

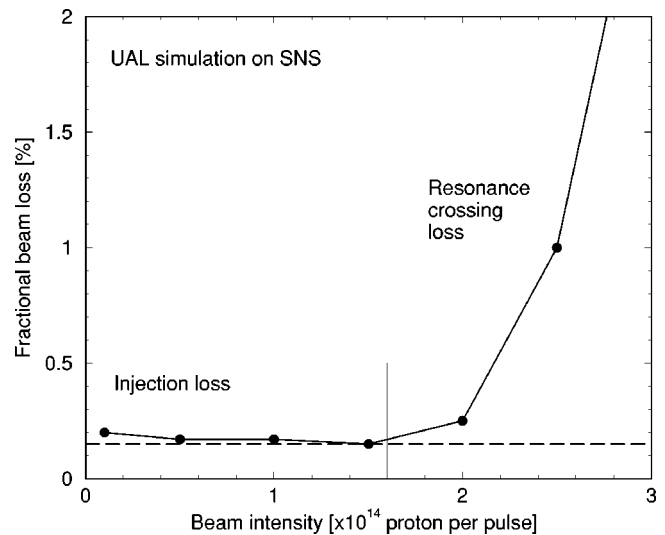


FIG. 39. Fractional uncontrolled beam loss as a function of final beam intensity of proton beam at the end of injection in the SNS accumulator ring. Computer simulation is performed with UAL/ORBIT package. Effects of space charge, chromaticity, kinematic nonlinearity, fringe field, and magnetic manufacturing imperfections are included. The base transverse tunes are (6.23, 6.20). Based on such a model, a beam intensity beyond 2×10^{14} protons per pulse is not achievable unless resonance corrections are applied (Sec. IV.B.3). Figure courtesy A. Fedotov.

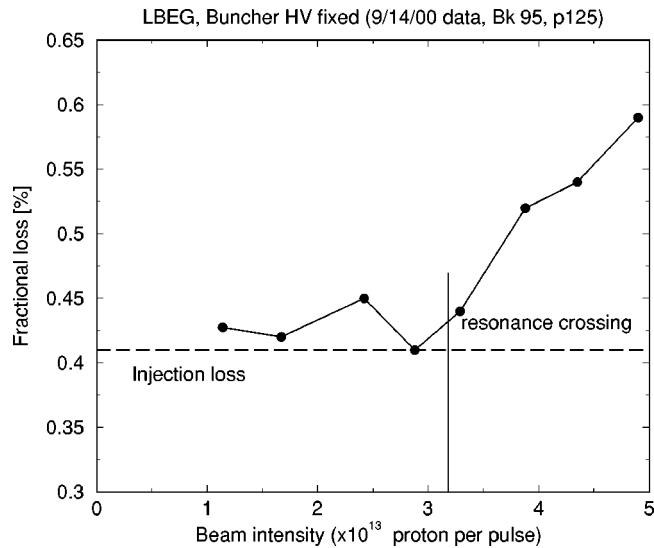


FIG. 40. Fractional uncontrolled beam loss as a function of final beam intensity of proton beam at the end of injection in the PSR accumulator ring. The transverse tunes are near (3.19, 2.19) (Sec. IV.B.3). Figure courtesy R. Macek.

C. Collective effects

Collective effects limit the beam current that may be transported through a high-intensity synchrotron. Collective effects can arise either directly from electromagnetic interaction of particles in the same bunch (space-charge effect) or indirectly, since a particle beam generates an electromagnetic field while passing through discontinuities and variations in the vacuum chamber's cross-sectional shape and conducting properties. The effects of Coulomb scattering among particles of the same bunch (intrabeam scattering) usually is negligible during the short time of accumulation and acceleration.

1. Space charge and beam halo

Space-charge effects set a fundamental limitation for medium-energy high-intensity synchrotrons. In contrast to linacs, where longitudinal and transverse bunch sizes are similar, in proton synchrotrons the longitudinal size of the bunch is usually much greater than its transverse dimensions. Accordingly, transverse space-charge tune shifts are orders of magnitude larger than the longitudinal ones, and so longitudinal and transverse space charge usually can be considered separately (Jones *et al.*, 1990; Holmes *et al.*, 1999).

In the longitudinal direction, space charge contributes a defocusing force below the transition energy. The longitudinal spread of the bunch may cause particles to escape from the rf bucket, requiring compensation by enhancing rf field focusing or introducing an inductive impedance into the ring (Sessler and Vaccaro, 1967).

In the transverse direction, the dominant effects are the coupling of the transverse motions and the development of space-charge resonances. The coherent tune of the beam, along with the associated collective oscillations, determines its resonant behavior. To prevent sig-

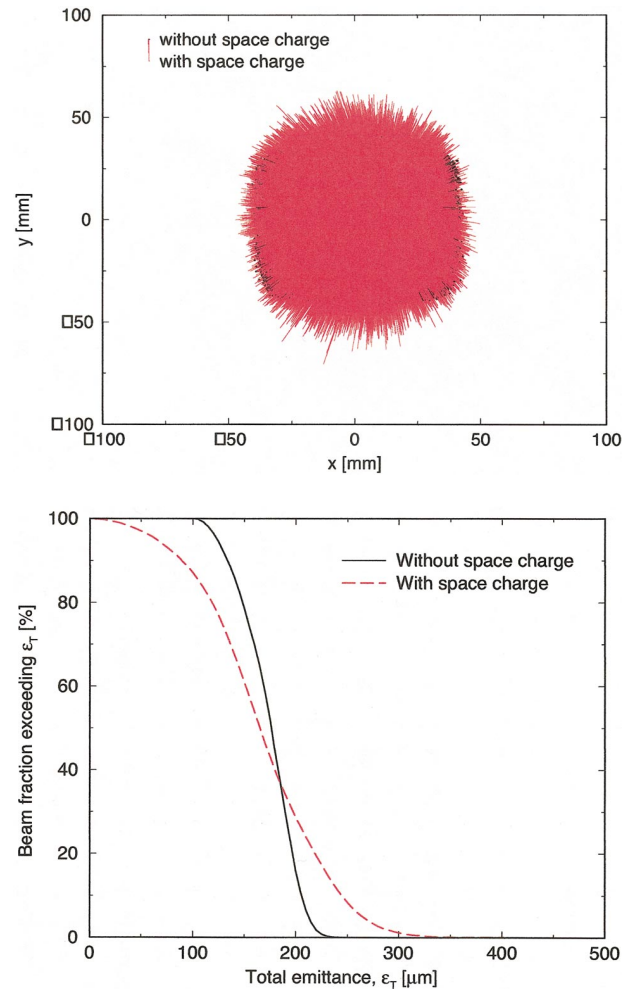


FIG. 41. (Color) Vertical emittance growth due to space charge if anticorrelated painting is used during SNS beam accumulation. The transverse tunes are (6.23, 6.20). For the data shown in black, space charge was neglected; for the data shown in red, the space-charge force for a 2-MW beam was included. Space charge produces a significant beam tail (Sec. IV.C.1). Figure courtesy A. Fedotov.

nificant beam broadening and emittance growth, it is necessary to maintain the coherent tunes of the beam away from low-order (integer and half integer) imperfection and structure resonances (Sec. IV.A.1). The choice of working tune is based on a consideration of the space-charge resonances and avoidance of higher-order resonances excited by lattice nonlinearity in the presence of space-charge-induced tune spread. When the horizontal and vertical tunes are close to each other, significant exchange of emittance also occurs, generating a round beam in the transverse physical space (Figs. 41 and 42). On the other hand, beam-core parametric resonance induced by beam mismatch, which is the primary source of halos in a proton linac, often is unimportant, especially for a multiturn injected ring when the halo is covered by the subsequently injected beam (Fedotov *et al.*, 2000).

The most effective approach to resolving space-charge problems is to raise the injection energy. Space charge

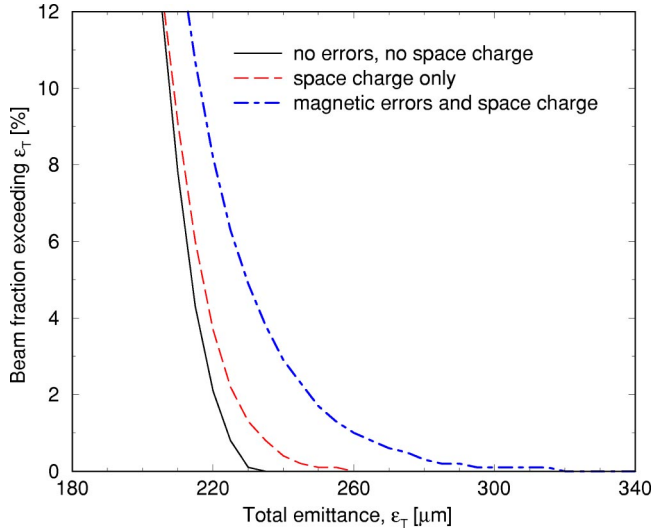


FIG. 42. (Color in online edition) Beam tail driven by space charge and magnet errors. The development of beam tail is noticeably enhanced by the combination of these two driving sources (Sec. IV.C.1). A nonstandard working point, (6.40,6.30), is chosen to illustrate the effect. The nominal working point, (6.23,6.20), is chosen to avoid resonances that lead to the development of such an enhanced beam tail (Sec. IV.C.1). Figure courtesy A. Fedotov.

can also be alleviated by longitudinal manipulation (e.g., dual-harmonic rf system, barrier cavity) to enhance the bunching factor, and by transverse and longitudinal painting and controlled injection as discussed in Sec. III.C.4. Longitudinal space-charge compensation using inductive inserts has also been demonstrated (Sessler and Vaccaro, 1967; Koba *et al.*, 1999; Ng *et al.*, 2001).

2. Coupling impedance

The coupling impedance describes the interaction between a beam and its environment (Sessler and Vaccaro, 1967; Zotter and Kheifets, 1998). Assume a harmonic excitation of beam current $\tilde{I}(\omega)$ at frequency ω which

excites a harmonic field with complex amplitude $\tilde{E}_z(\omega)$. The longitudinal coupling impedance is defined as

$$Z_{\parallel}(\omega) = -\frac{1}{\tilde{I}(\omega)} \oint \tilde{E}_z \exp(j\omega s/\beta c) ds. \quad (34)$$

The vertical and horizontal coupling impedances are defined as the integrals of the deflecting fields over one turn, normalized by the dipole moment of the excitation beam current,

$$Z_y(\omega) = \frac{j}{\tilde{I}\Delta y} \oint [\tilde{E}_y + \beta c \tilde{B}_x]_{|x=0, y=\Delta y} \exp(j\omega s/\beta c) ds,$$

$$Z_x(\omega) = \frac{j}{\tilde{I}\Delta x} \oint [\tilde{E}_x - \beta c \tilde{B}_y]_{|x=\Delta x, y=0} \exp(j\omega s/\beta c) ds, \quad (35)$$

where \tilde{E}_x , \tilde{E}_y , \tilde{B}_x , and \tilde{B}_y are the transverse components of the electric- and magnetic-field vectors in the frequency domain, and Δx and Δy are the horizontal and vertical offsets of the beam from the axis. With these definitions, Table V is an example of the coupling impedance “budget” estimated for the SNS accumulator ring at frequencies below 10 MHz. For simplicity, we use Z_{\perp} to represent both Z_x and Z_y .

Minimizing the impedance is an important measure to prevent collective instabilities. Below transition energy, the reactive part of the impedance generally is dominated by space charge, whose effect is discussed in Secs. IV.A.1 and IV.C.1 and whose value is given by

$$Z_{\parallel}^{\text{sc}}(\omega) = -j \frac{n g_0 Z_0}{2\beta \gamma^2}; \quad Z_{\perp}^{\text{sc}}(\omega) = -j \frac{g_0 Z_0}{\beta^2 \gamma^2} \left(\frac{1}{a^2} - \frac{1}{b^2} \right), \quad (36)$$

where $n = \omega/\omega_s$, $Z_0 = (\epsilon_0 c)^{-1} = 377 \Omega$, a is the effective beam radius, b is the radius of the vacuum pipe, and $g_0 \approx 1/2 + 2 \ln(b/a)$ for the geometric factor. Both transverse and longitudinal space-charge impedances can be reduced by allowing the contours of the conducting vacuum enclosure to follow the variations in the beam’s

TABLE V. Estimated beam coupling impedance of the SNS accumulator ring at frequency below 10 MHz. The beam revolution frequency is 1.058 MHz. The leading impedance source contributing to possible instability is the extraction kicker modules located inside the beam vacuum pipe (Sec. IV.C.2).

Device/Mechanism	Z_{\parallel}/n (Ω)	Z_{\perp} (k Ω /m)	Comment
Space charge	$-j196$	$j(-5.8+0.45) \times 10^3$	incoherent and coherent part
Extraction kicker	$0.6n + j50$	$33 + j125$	25 Ω termination at PFN
Injection kicker & pipe	$0.5/n$	17.5	pipe coated; lowest tune at 200 Hz
Injection foil assembly	$j0.05$	$j4.5$	MAFIA modeling
rf cavity	0.9 (resonance peak)	18	to be damped
Resistive wall	$(j+1)0.71$ at ω_0	$(j+1)8.5$ at ω_0	
Broadband beam position monitor	$j4$	$j18$	
Broadband bellows	$j1.1$	$j7$	unscreened
Broadband steps	$j1.9$	$j16$	tapered 1-to-3 ratio
Broadband ports	$j0.49$	$j4.4$	screened
Broadband valves	$j0.15$	$j1.4$	unscreened
Broadband collimator	$j0.22$	$j2.0$	

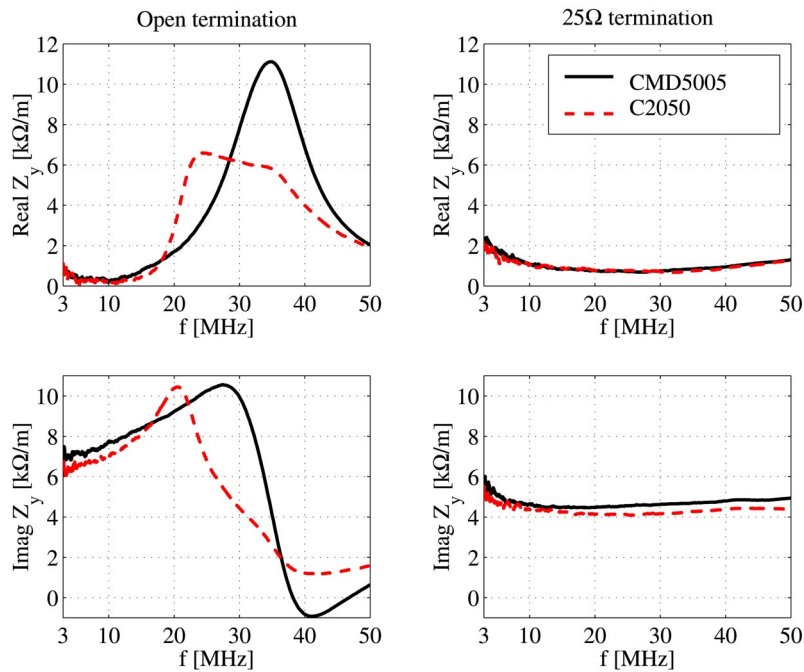


FIG. 43. (Color in online edition) Comparison of bench-measured coupling impedance for open and $25\ \Omega$ pulse-forming network termination, and high (1600) and medium (100) permeability ferrite of the SNS ring extraction-kicker assembly. The extraction kickers, residing inside the vacuum chamber of the SNS ring, are a major source of beam coupling impedances (Sec. IV.C.2). Figure courtesy D. Davino and H. Hahn.

envelope. This practice was adopted at the ISIS synchrotron, using metal wires contoured to the beam's envelope inside the ceramic beam pipe (Boardman, 1982).

The growth of an instability is associated mostly with the resistive part of the impedance. For the ISIS synchrotron, as well as the SNS and the ESS accumulator ring, the leading resistive component of the coupling impedance is from the extraction kicker modules located in the vacuum pipe. The coupling impedance is minimized by the design of the pulse-forming network (PFN) power-supply circuits (low termination impedance). The frequency dependence of the coupling impedance further depends on the permeability of the ferrite material. Ferrite material of relatively low permeability and low resistive loss was found to be beneficial if the PFN was not terminated with a low impedance (Fig. 43; Davino, 2002). Wrapping a special metal loop around the ferrite blocks was proposed as a method to influence the coupling response of the kicker module without changing the design kicker's magnetic field (Lee, 2002).

Impedance due to the resistive wall of the vacuum chamber can become important at low frequencies. When the thickness of the conducting chamber's wall is greater than the skin depth δ_s [Eq. (11)], the impedances are given by

$$Z_{\parallel}^{\text{rw}}(n\omega_s) = n(1+j) \frac{\beta Z_0 \delta_s}{2b}; \quad Z_{\perp}^{\text{rw}}(n\omega_s) = (1+j) \frac{R_0 Z_0 \delta_s}{b^3}. \quad (37)$$

Investigations have been pursued on the coupling impedance of thin resistive layers, such as the metallic coatings of ceramic vacuum chambers in kicker magnets. Theoretical studies showed that the beam's image current flows in the resistive layers, even in the low-frequency regime when the skin depth δ_s is larger than the layer's thickness, unless external structures offer alternative paths of lower impedance. At very low fre-

quencies, where δ_s^2 exceeds the product of the chamber's radius times the layer's thickness, a significant reduction in the real part of the transverse impedance might be expected. These predictions were validated by preliminary bench measurements at CERN (Piwinski, 1977; Henderson, 1998; Caspers *et al.*, 2000). Two layers of coating were applied to the SNS ring's ceramic chamber for injection kickers: a $1\text{-}\mu\text{m}$ -thick copper layer for bypassing the image charge and a $0.1\text{-}\mu\text{m}$ -thick titanium nitride (TiN) layer for a low secondary-electron yield, along with an exterior metal enclosure for dc current bypass. Such a design allows the passage of the image current above a frequency of the lowest betatron sideband (~ 200 kHz) without degrading the magnetic-field penetration (a rise time of about $200\ \mu\text{s}$), eddy-current heating, and beam-induced heating. Improvements to the vacuum chamber bypass also are planned at the CERN PS Booster, and shielding of the magnet septa and vacuum ports is underway at the CERN SPS.

LANL (PSR) and KEK assessed the ability of inductive inserts to compensate for the longitudinal space-charge coupling impedance. Such devices are considered practical for machines like the proposed CERN accumulator, which requires an inductive Z_{\parallel}/n of $70\ \Omega$, with a real part no larger than $1\ \Omega$ (Chou and Wei, 2001).

Computer modeling frequently is used to predict the coupling impedance of a device (Weiland, 1998). However, computation becomes inefficient when the geometry of the device is complex and asymmetric and when the material's permeability is high. Bench measurements are needed to determine the impedance of critical devices, e.g., the extraction kicker and its power-supply (PFN) network (Nassibian and Sacherer, 1979; Wang and Zhang, 2000; Davino *et al.*, 2002). After the machine is constructed, the total coupling impedance can be determined by measuring the beam's transfer function, energy loss, and tune shifts (Zotter and Kheifets, 1998).

TABLE VI. Collective effects and estimated thresholds for a 2-MW beam power in the SNS accumulator ring. The dominant effects are expected to be beam halo and beam loss generated by space-charge-related resonance crossing. Other intensity-limiting mechanisms include electron-cloud effects and instabilities due to the extraction kicker coupling impedance (Sec. IV.C.3).

Mechanism	Threshold	Comments
Transverse space charge	$\Delta \nu_{sc} \approx -0.2$	resonance crossing
Longitudinal space charge	15 kV induced RF voltage	60 kV RF voltage
Transverse microwave instability	$Z_{\perp} \approx 60 \text{ k}\Omega/\text{m}$	extraction kicker impedance
Longitudinal microwave instability	$ Z_{\parallel}/n \approx 100 \Omega$	extraction kicker impedance
Resistive wall		(walls and kicker impedance)
($\xi=0$)	$Z_{\perp} \approx 1.3 \text{ k}\Omega/\text{m}$	at 200 kHz; rise time $>300 \mu\text{s}$
($\xi=-3$)	$Z_{\perp} \approx 100 \text{ k}\Omega/\text{m}$	at 200 kHz
Electron cloud	above 2 nC/m	above 2% neutralization in beam

3. Instabilities

Instabilities are common in proton rings (Laslett *et al.*, 1961; Neil and Sessler, 1965; Chao, 1993). Due to the short accumulation time (typically around one synchrotron-oscillation period), a proton beam in an accumulator is susceptible only to fast, transverse instabilities like the electron-proton instability limiting the beam intensity in the PSR ring (Sec. IV.D.3; Macek *et al.*, 2001). On the other hand, rapid-cycling and conventional synchrotrons are susceptible to an extended list of instabilities. Head-tail instabilities were observed near injection in the KEK PS, the CERN PS, and the BNL AGS and are suspected to be due to chromaticity change caused by eddy-current-induced sextupole fields (proportional to \dot{B}/B) in the vacuum chamber under the dipole magnets. This type of instability can be cured by chamber correction windings (AGS Booster), chromaticity control, Landau damping with octupoles, and tune manipulation. Negative mass and microwave instabilities are observed at the CERN PS and SPS, the BNL AGS, and the KEK PS. They can be avoided by measures that reduce impedance (e.g., shielding vacuum ports and septa) and that improve the bunching factor (e.g., using dual-harmonic or dilution cavities). Instability in coupled bunches was observed at the CERN PS Booster, PS, and SPS, and the BNL AGS and was damped by fast feedback systems and Landau damping systems. The ISIS programs the tunes in each cycle to accommodate natural variations in chromaticity, to depress space-charge tunes, and to avoid the resistive-wall head-tail instability (Rees, 1994).

Next-generation proton sources, like the compressor ring for a neutrino factory or a muon collider, are expected to operate in the regime of kiloamperes, with peak beam current at low to medium energy (Ng and Zotter, 2001). In these machines, the intensity of the beam will be pushed close to its stability limits in the presence of strong space-charge and nonlinear resonances (Table VI).

A coasting-beam formalism may be applied to a bunched beam if the bunch length is much longer than the characteristic wavelength of the driving wake field, and if the instability growth rate is comparable with or faster than the synchrotron-oscillation frequency (Wang

and Pellegrini, 1980; Koscielniak, 1999). The criterion for longitudinal bunched-beam stability is the Keil-Schnell condition (Nielson *et al.*, 1959; Ruggiero *et al.*, 1968; Keil and Schnell, 1969; Boussard, 1975)

$$|Z_{\parallel}/n| \leq F_{\parallel} \frac{|\eta| B_f E_s}{e \beta^2 I_0} \left(\frac{\Delta E}{E_s} \right)_{\text{FWHM}}^2, \quad (38)$$

where I_0 is the average bunch current, η is the slip factor, and the form factor $F_{\parallel} \approx 1$ for a parabolic distribution. For transverse bunched-beam stability, this criterion is (Sacherer, 1977)

$$|Z_{\perp}| \leq F_{\perp} \frac{4 B_f E_s}{e \beta \langle \beta_{\perp} \rangle I_0} \left(\frac{\Delta E}{E_s} \right)_{\text{FWHM}} |(n - \nu_{\perp}) \eta + \xi_{\perp}|, \quad (39)$$

where the form factor F_{\perp} depends on the distribution of transverse particles, n is an arbitrary integer, and ξ_{\perp} is the chromaticity. Instability occurs only for slow waves with $n > \nu_{x,y}$. The lowest threshold obtained for n is just above the tune, $\nu_{x,y}$. The machine's chromaticity ξ_{\perp} plays an important role in providing Landau damping (Landau, 1946). Below transition energy, $\eta < 0$, the natural chromaticity ($\xi_{\perp} < 0$) helps to damp transverse instability.

The observed threshold for longitudinal instability may not correspond to that estimated from the Keil-Schnell criterion, especially in the presence of a strong space charge. Examples are the ISIS synchrotron, the CERN PS, and the BNL AGS Booster. In the longitudinal direction, space charge typically reduces the growth rate of instability with its debunching force (below transition) and results in self-stabilization (Hofmann, 1985; Rumolo *et al.*, 1998; Hofmann and Boine-Frankenheim, 1999; Koscielniak, 1999; Boine-Frankenheim and Hofmann, 2000; Woody *et al.*, 2001). Transversely, space charge lowers the instability threshold by altering the mode frequency and mode-coupling condition (Blaskiewicz, 1998; Fedotov and Hofmann, 2002). Recent developments in computer simulation have made it possible to investigate the mechanism numerically (Galambos *et al.*, 1999; Malitsky *et al.*, 1999).

Longitudinal and transverse coupled-bunch instabilities are mostly driven by the parasitic resonances in the rf system. Such instability is often cured by passively damping such resonances or by installing a fast bunch-by-bunch damper.

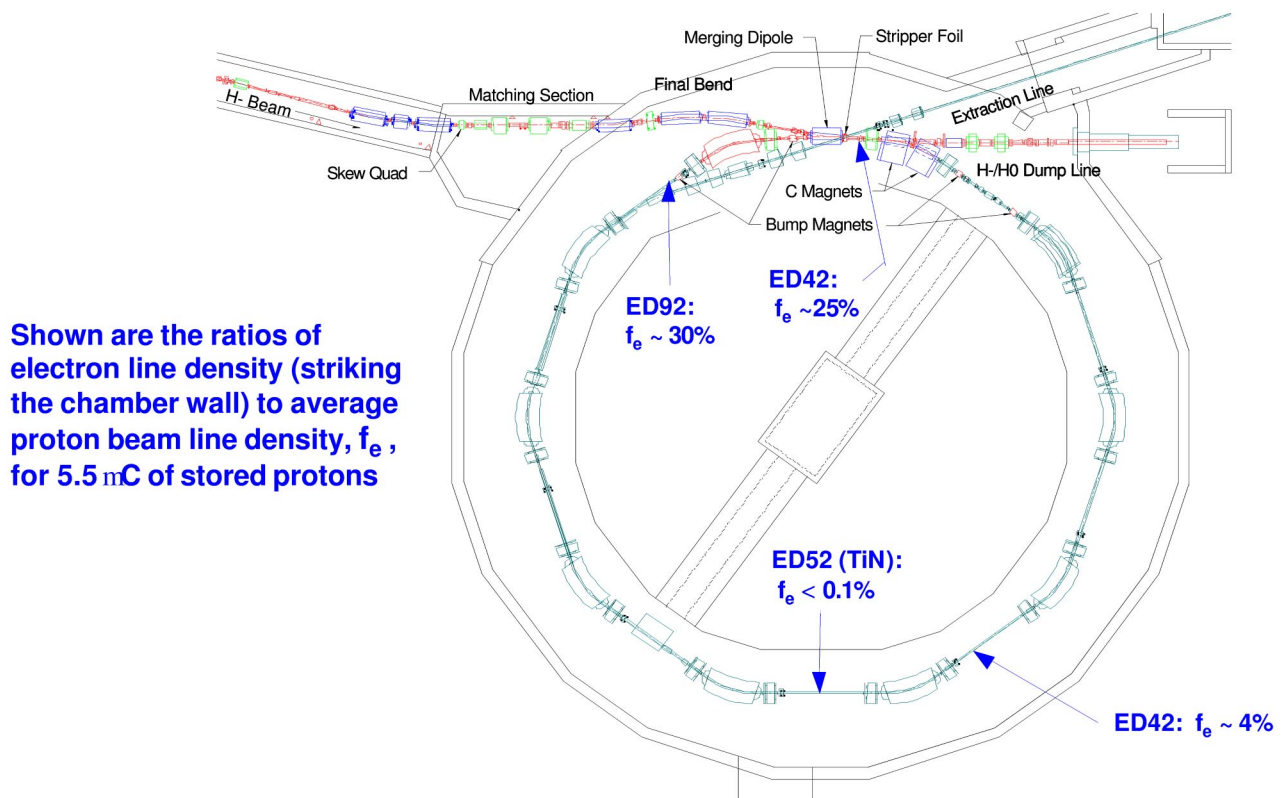


FIG. 44. (Color in online edition) Distribution of the electron flux measured on the wall of the vacuum pipe at the PSR. The circumference of the ring is 90.2 m. The kinetic energy of the proton beam is 800 MeV. The flux ratio f_e , varying around the ring, is about 30% downstream of the extraction septum, about 25% downstream of the injection stripping foil, about 4% in section 4, and within the noise level in the TiN-coated section 5 (Sec. IV.D.1). Figure courtesy R. Macek.

Feedback systems frequently are used to damp instabilities. The long wake of resistive-wall impedance may cause a closed-orbit drift during acceleration that can be damped by a slow-rate feedback system (Danilov, Henderson, *et al.*, 2001). On the other hand, fast-rate feedback systems are required to damp “banana closed-orbit” instability (Sec. III.E), electron-cloud instability, (Sec. IV.D), and coupled-bunch instability.

D. Electron-cloud effects

Electron-cloud effects are important, but incompletely understood dynamical phenomena. Effects that can severely limit the performance of high-intensity proton synchrotrons include trailing-edge tune shift and resonance crossing, electron-proton instability, emittance growth and beam loss, increases in vacuum pressure, heating of the vacuum pipe, and interference with beam diagnostics. The following are examples of hadron rings where electron-cloud effects are observed: the Proton Storage Ring (PSR) at the Los Alamos National Laboratory (LANL), where a strong, fast transverse instability occurs both for coasting and for a bunched beam when a threshold intensity is exceeded (Macek, 1999); the CERN PS and SPS, where a large number of electrons are produced by beam-induced multipacting

when the machine’s parameters are configured for LHC injection (LHC, 1995; Arduini *et al.*, 2000; Métral *et al.*, 2001); and the Relativistic Heavy Ion Collider (RHIC), where the vacuum pressure dramatically increases when the beams are injected with halved nominal bunch spacing (Zhang, 2002). Electron-cloud effects could limit the performance of the next-generation high-intensity proton rings, such as the Spallation Neutron Source’s (SNS’s) accumulator ring (Wei, Abell, *et al.* 2000), and neutrino-factory proton drivers.

1. Electron generation

Electron production is classified into the following categories: (1) electrons generated at the stripping foil; (2) electrons generated at collimators and vacuum-pipe surfaces due to the impact of lost protons; (3) electrons produced by multipacting from the vacuum chamber’s wall; and, (4) electrons produced around the ring from residual-gas ionization.

As an example, Fig. 44 shows the distribution of electron-density flux measured at the PSR using the electron detector developed at the Argonne National Laboratory (Rosenberg and Harkey, 2000). The quantity f_e is defined as the ratio of the number of electrons striking the vacuum pipe within one turn to the number of

TABLE VII. Estimated yield and kinetic energy of the electrons produced by the H^- beam at injection into the PSR. The yield is defined as the ratio of total number of electrons produced during the accumulation period per injected H^- particle. The average number of foil traversals is about 50. The kinetic energy of the injecting beam is 800 MeV. The average H^- beam current is $100 \mu A$ (Sec. IV.D.1, courtesy M. Plum).

Source	Yield	Kinetic energy
Stripped electron	2.0	430 keV
Secondary electron	1.0	up to 20 eV
Knock-on electron	0.4	up to 2.4 MeV
Thermionic electron	<0.002	~ 0.24 eV
Residual-gas ionization	0.02	up to 2.4 MeV

stored protons in the ring, scaled from the area of the detector's surface. The electron density is high at the injection region, where the H^- beam is stripped of its electrons, and high at the extraction region, due to the limited aperture. Near the injection stripping foil, a high concentration of electrons is expected with a broad energy spectrum. With a H^- beam, the stripped electrons carry twice the current of the injecting H^- beam and have a kinetic energy of $m_e c^2(\gamma - 1)$, where γ is the relativistic factor of the H^- beam. The injecting and circulating beams impacting on the foil produce secondary emission of electrons at low energy (tens of eV). Although the yield is low (0.006 for an 800-MeV proton beam incident on carbon material), the effect is proportional to the number of traversals of the foil. The injecting and circulating beams also produce knock-on electrons at a high energy (up to several MeV). The stripping foil, operating at a high temperature around

2000 K, emits thermionic electrons at low energy. All these electrons may back-scatter from the stripped-electron collector and the surrounding surfaces. Table VII lists the sources of production, yield, and energy-range of the electrons at the PSR's injection region (Plum, 1995)

The region near the scrapers and collimators is susceptible to a high beam loss and, potentially, is another location of high electron concentration. Protons incident on the collimator's surfaces produce secondary electrons. Depending on the energy of the beam and the incident angle, the secondary-electron-to-proton yield can greatly exceed 1 when the incident beam is nearly parallel to the surface (i.e., grazing angle $\theta_g \approx \pi/2$). Experiments were performed with different ions at the Brookhaven Tandem Accelerator to verify the angular dependence of electron yield (Thieberger *et al.*, 1999). As shown in Fig. 45, the proton-induced yield Y_{ep} has a $1/\cos \theta_g$ dependence on the angle θ_g , similar to the electron-induced secondary-emission yield as predicted by the Seiler model based on experimental fits (Shou *et al.*, 1980; Seiler, 1983; Borovsky *et al.*, 1988; Zhang, 2002),

$$Y_{ep} = \frac{1.11 Y_{ep}^{\max} \left\{ 1 - \exp \left[-2.3 \left(\frac{E_k}{E_k^{\max}} \right)^{1.35} \right] \right\}}{\left(\frac{E_k}{E_k^{\max}} \right)^{0.35} \cos \theta_g}, \quad (40)$$

where E_k is the kinetic energy of the primary proton, and the proton energy that corresponds to the maximum yield E_k^{\max} is about 0.7 MeV. A serrated surface with triangular teeth greatly reduced the generation of secondary-emission electrons. However, at a beam en-

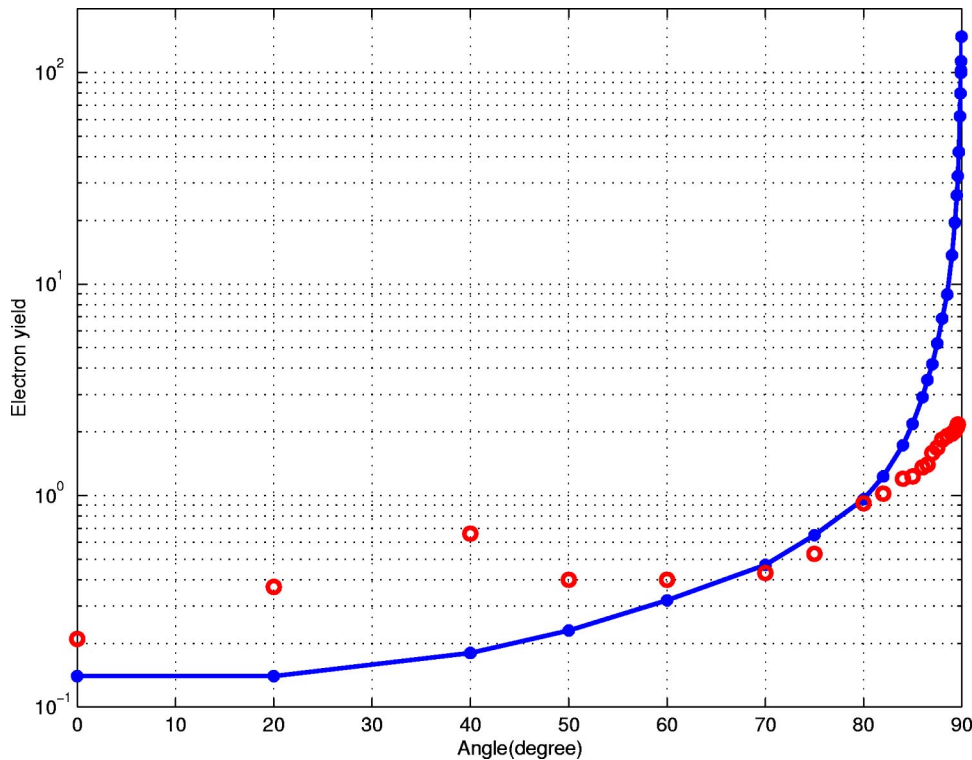


FIG. 45. (Color in online edition) Proton-induced secondary-emission yields of electrons as functions of the incident angle for 28-MeV protons striking a flat (solid line) and a serrated (open circles) stainless-steel surface (Sec. IV.D.1). Figure courtesy P. Thieberger.

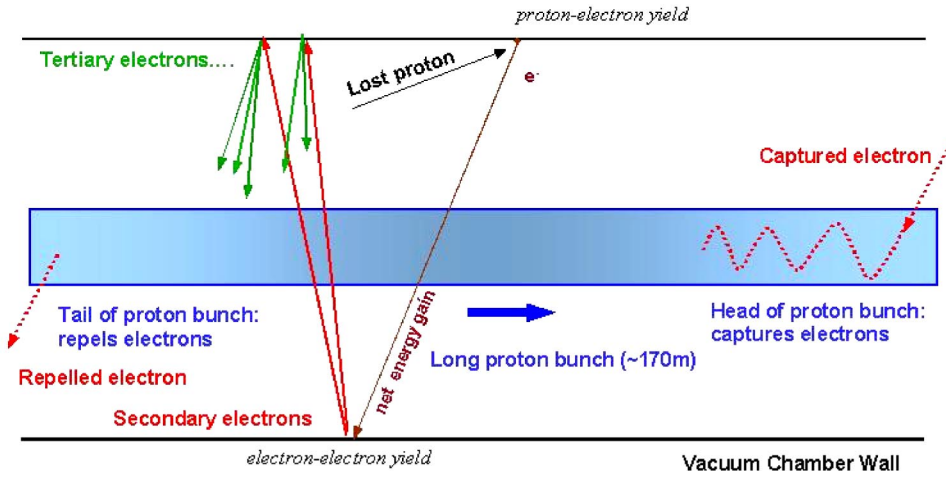


FIG. 46. (Color in online edition) Beam-induced electron multipacting at the trailing edge of a long proton bunch. The transit time of the electrons across the beam pipe is much shorter than the passage time of the proton bunch (Sec. IV.D.1).

ergy of around 1 GeV the proton stopping length is long (about 1 m). A serrated surface may be ineffective, since protons incident on the front edge of the teeth may easily escape from the collimator body. The SNS ring uses a two-stage collimation system so that the beam halo is likely to be incident on the front edge of the secondary collimators.

Beam-induced multipacting is believed to be the leading source of sustained electron production. Depending on the beam parameters, one of two multipacting models applies: multibunch passage multipacting (Gröbner, 1977, 1997; Furman and Lambertson, 1997; Zimmermann, 1997; Ruggiero *et al.*, 2001), or single-bunch, trailing-edge multipacting (Danilov *et al.*, 1999; Macek, 1999).

The phenomenon of multibunch, beam-induced multipacting was observed at the CERN PS and SPS when the machines' parameters were configured for LHC injection. The electron-cloud buildup was sensitive to the intensity, spacing, and length of the proton bunches, and to the secondary-emission yield of electrons from the beam-pipe surfaces. The multibunch multipacting occurs if the transit time of the electrons crossing the vacuum pipe is comparable to the time between successive bunches and if the electrons gain enough energy to produce more than one secondary electron when they hit the vacuum-pipe wall (Gröbner, 1977). The multipacting parameter ζ_m is defined as the ratio between the transit time of the electrons crossing the vacuum pipe to the time between successive bunches (Gröbner, 1977; Wei and Macek, 2002),

$$\zeta_m = \frac{2b}{s_b} \frac{\beta}{\beta_e} \approx \frac{\beta^2 b^2}{r_e N_0 s_b}, \quad (41)$$

where s_b is the distance between the successive bunches, βc is the velocity of the proton beam, $\beta_e c$ is the average velocity of the electrons, and the second relation is true if the electron motion is nonrelativistic. Here, β_e is related to the energy gained by the electron from the passage of the proton bunch,

$$\Delta E_e = m_e c^2 \left[\sqrt{\left(\frac{2r_e N_0}{\beta b} \right)^2 + 1} - 1 \right] \approx 2m_e c^2 \left(\frac{r_e N_0}{\beta b} \right)^2, \quad (42)$$

where $r_e = e^2/4\pi\epsilon_0 m_e c^2$ is the classical radius of an electron. The condition for proper multibunch multipacting is given by $\zeta_m = 1$. The energy gained by an electron must be such that the electron-induced secondary-emission yield satisfies $\alpha_e Y_{ee} > 1$, where $\alpha_e \leq 1$ is the electron survival rate in the bunch gap (Zhang, 2002). Multibunch electron multipacting may occur for almost any value of ζ_m (Zimmermann, 2001).

Single-bunch, trailing-edge multipacting starts to dominate if the bunch length is long enough to sustain multiple passes of electrons. As shown in Fig. 46, electrons are attracted to the rising edge of the proton bunch. The motion is characterized by the electron bounce frequency,

$$\omega_e = c \sqrt{2\pi r_e n_p}, \quad (43)$$

where n_p is the volume density of the proton beam. At the trailing edge of the proton bunch, electrons are released and accelerated by the bunch. The number of electrons grows dramatically at the trailing edge of the proton bunch, as observed at the PSR (Fig. 47) (Macek *et al.*, 2001). The electron-cloud buildup due to this single-bunch mechanism is expected to have a weak de-

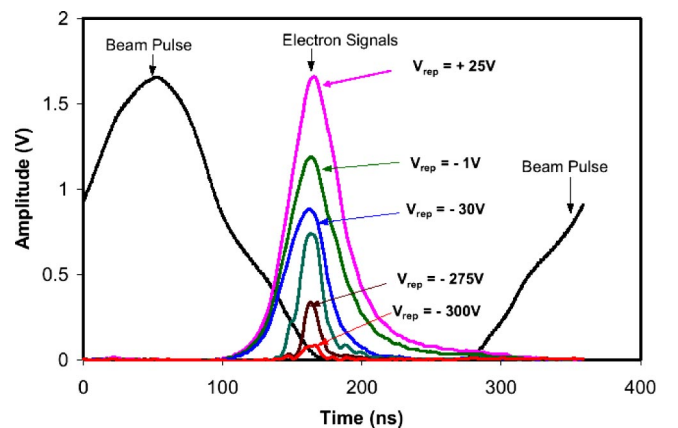


FIG. 47. (Color in online edition) Electron signals measured at the PSR as a function of time relative to the proton-beam pulse during a single revolution. The proton bunch length is about 250 ns. The repeller voltage V_{rep} is varied to select the electrons striking the detector according to their energy (Sec. IV.D.1). Figure courtesy R. Macek.

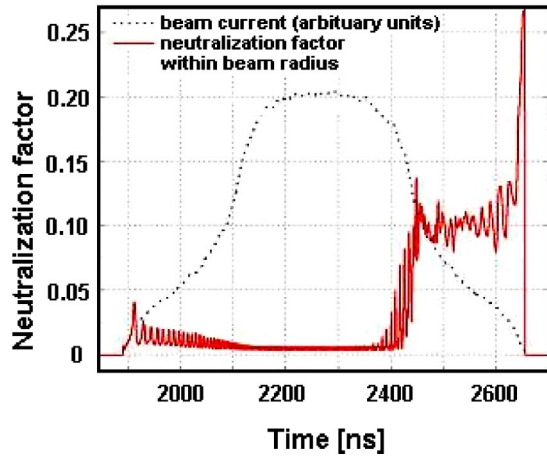


FIG. 48. (Color in online edition) Computer simulation of electron generation in the SNS accumulator ring (Sec. IV.D.1). The neutralization factor is defined as the density ratio between the electron and proton within the proton beam radius. The beam intensity is 2×10^{14} per bunch. The peak secondary-emission yield is assumed to be 2. The full bunch length is about 700 ns. The amount of peak neutralization at the trailing edge of the bunch is higher than the simulated amount for the PSR (about 5%). Preventive measures are adopted to minimize electron generation and to enhance Landau damping (Sec. IV.D.4). Figure courtesy M. Pivi and M. Furman.

pendence on bunch spacing, the vacuum pressure level, and the amount of residual protons in the beam gap. On the other hand, it depends critically on the length of the proton bunch and the variations in its longitudinal density. The single-bunch multipacting parameter ζ_s is defined as the ratio between the transit time of the electrons crossing the vacuum pipe to the passage time of half of the proton bunch (Wei and Macek, 2002),

$$\zeta_s = \frac{b}{s_b B_f} \frac{\beta}{\beta_e} \approx \frac{\beta b}{\sqrt{r_e N_0} s_b B_f}. \quad (44)$$

The energy gained by an electron is approximately

$$\Delta E_e \approx 4m_e c^2 \beta b \sqrt{\frac{r_e N_0}{s_b^3 B_f^3}}. \quad (45)$$

Single-bunch multipacting occurs if the condition $\zeta_s \ll 1$ is satisfied and if the energy gained by an electron is such that $Y_{ee} > 1$. Figure 48 shows an example of such single-bunch, trailing-edge multipacting with the SNS parameters (Pivi, 2002). The actual multipacting process may be a combination of single-bunch and multibunch multipacting.

Due to gas ionization, the rate of electron line-density increase per unit length of circumference is given by the relation (Zimmermann, 2001; Zhang, 2002)

$$\frac{d^2 \lambda_e}{dt ds} = \frac{\rho_m \beta I \sigma_{\text{ion}} P}{133.3e}, \quad (46)$$

where I is the proton current, σ_{ion} is the ionization cross section, P is in units of pascal (1 torr = 133.3 Pa). At a room temperature of 300 K, the molecular density ρ_m is

about $3.3 \times 10^{22} \text{ m}^{-3}$. The effect of photoemission usually is negligible for medium-energy protons due to lack of synchrotron radiation.

Various computer simulation programs were developed to model the process of electron generation (Ohmi, 1995; Furman and Lambertson, 1997; Zimmermann, 1997). Simulated mechanisms included space-charge fields of both protons (or e^+) and electrons, vacuum pipe and image charges, external magnetic fields, gas ionization, secondary emission, and photoemission. Recent developments have incorporated trailing-edge multipacting, rediffusion, backscattering, and proton-induced secondary emission with refined angular dependence of the incident particle (Blaskiewicz *et al.*, 2000; Danilov, Aleksandrov, *et al.*, 2001; Pivi, 2002). Particle-in-cell (PIC) algorithms also were developed to model detailed electron-generation processes (Wang, Channell, *et al.*, 2001).

2. Electron neutralization and the Pacman effect

An electron cloud tends to neutralize the positive charge of the proton beam. Compared to the space-charge tune shift between the protons, the tune shift produced by an electron cloud is enhanced by a factor γ^2 due to absence of compensating electric and magnetic forces in the laboratory frame. With the trailing-edge electron multipacting model, protons at the trailing edge of the bunch experience, on average, a high concentration of electrons. Electron neutralization increases the transverse tunes and possibly increases the tune shift of the beam. When the beam is stored in the ring for an extended time, the bunch may continuously lose its trailing-edge particles upon resonance crossing. We refer to this as the trailing-edge Pacman effect.

3. Electron-proton instabilities

Experimental observations of electron-cloud instabilities are distinctively different for “short bunches” stored at energies above the transition energy, where multi-bunch multipacting is expected to be important (the PS, SPS, and B factories), and “long bunches” stored at energies far below the transition energy, where single-bunch, trailing-edge multipacting is expected to be dominant (the PSR and SNS).

During the 1970s, coupled oscillations associated with electron trapping and multipacting occurred during high-intensity coasting-beam operation at the CERN ISR (Hereward, 1971; Keil and Zotter, 1971; Gröbner, 1977). The problem was alleviated by installing additional clearing electrodes around the ring. Since 1988, a fast, vertical instability accompanied by beam loss, with both bunched and unbunched beams, was attributed to coupled electron-proton oscillations (Neuffer, 1992; Macek *et al.*, 2001). At the BNL AGS Booster, an intense proton beam became vertically unstable when it was debunched.

The threshold of electron-proton instability is associated with the amount of Landau damping caused by the beam’s momentum spread (Keil and Zotter, 1971; Zenkevich and Koshkarev, 1972; Laslett, Sessler, and Möhl,

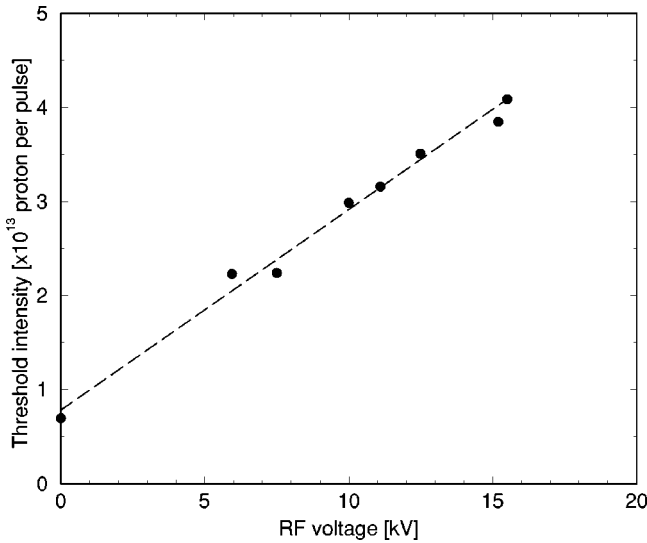


FIG. 49. Intensity threshold of the transverse instability as a function of the rf voltage at the PSR. The instability, accompanied by a large beam loss, occurs during a multiturn charge-exchange injection when the accumulated beam intensity reaches the threshold level. Growth time for the instability is about 75 ms or 200 turns. The unstable beam motion is at a frequency range between 70 and 200 MHz, depending on the beam intensity (Sec. IV.D.2). Figure courtesy R. Macek.

1974). Figure 49 shows the measured dependence of the threshold intensity on rf voltage for a given length of an injected bunch. The threshold scaling is different from that of transverse instability due to conventional coupling impedance, in which the threshold intensity is proportional to the rf voltage squared [Eq. (39)]. The linear dependence of the threshold results from the dependence of the instability's frequency on the beam's intensity (Blaskiewicz, 2000). In fact, at the electron bounce frequency ω_e , the transverse frequency spread is mostly contributed by the momentum slip, i.e.,

$$\frac{\omega_e}{\omega_0} \gg \nu_{x,y}; \quad |\eta|\omega_e \gg \xi_{\perp}\omega_0, \quad (47)$$

where ω_0 is the angular revolution frequency, η is the momentum-slip factor, $\nu_{x,y}$ are the transverse tunes, and ξ_{\perp} is the chromaticity. The threshold for the transverse stability is

$$|Z_{\perp x,y}| \leq F_{\perp} \frac{4|\eta|E_s}{\sqrt{\pi}e^2\omega_0 a \langle \beta_{\perp} \rangle} \sqrt{\frac{B_f R_0 r_e}{N_0} \left(\frac{\Delta p}{p} \right)_{\text{FWHM}}}, \quad (48)$$

where $(\Delta p/p)_{\text{FWHM}}$ is the full-width-at-half-maximum momentum spread of the beam, E_s is the total energy of the proton, F_{\perp} is the form factor, and a is the average beam radius. With a given coupling impedance, the threshold intensity is linearly proportional to the momentum spread squared and is insensitive to the machine's chromaticity. Also, the scaling behavior is extended from bunched beams to a coasting beam as the rf voltage is lowered.

Several theoretical approaches have been taken to study instabilities of the coupled electron-proton mo-

tion. Centroid models of rigid beams provided estimates of the unstable dipole modes and their scaling with intensity for coasting beams. They offered plausible predictions for the threshold intensities of the instability, given the uncertainties in parameters such as average neutralization (Laslett, Sessler, and Möhl, 1974; Neuffer, 1992; Wang, Channel, *et al.*, 2001). However, estimates of growth rates and behavior beyond threshold showed poor agreement with observations. The centroid models were extended to bunched beams to better describe the trailing-edge electron concentration, the instability threshold, and the structure and growth rates above the threshold (Blaskiewicz, 2000). Another approach was to develop fully kinetic simulations based on self-consistent solutions of the Maxwell-Vlasov equations for coasting beams in a smooth-focusing approximation (Davidson *et al.*, 1999).

The short-bunch regime included instabilities that occurred at most lepton (e^+) rings (the KEK photon factory, B factory KEKB, and BEPC), as well as proton rings (PS and SPS) when the beams were prepared for collider uses (Zimmermann, 2001). Coupled-bunch, transverse instabilities were observed at the KEK PF (Izawa *et al.*, 1995; Ohmi, 1995) and BEPC (Guo *et al.*, 1998), and at the SPS (horizontal direction) with the LHC proton test beams (Arduini *et al.*, 2001). The electron cloud coupled the motion of subsequent bunches similar to a multibunch wake field. With computer simulations, the effective wake fields were computed to predict the multibunch growth rates.

Single-bunch, transverse (strong and regular head-tail, fast blowup) instabilities were identified first at the KEK B factory and then at the CERN SPS (vertical direction) and the PS with the LHC proton test beams. The electron cloud coupled the head and tail of the bunch similar to a short-range wake field. A broadband-resonator model was used to describe the coupling impedance, with the resonator frequency at the electron bounce frequency (Ohmi *et al.*, 2001). Such single-bunch instabilities were often sensitive to the chromaticity.

Theoretically, beam breakup treatment and a two-particle model were used to obtain the threshold and growth time of the instability, assuming that the electron production saturated near the neutralization density (Raubenheimer and Zimmerman, 1995; Ohmi and Zimmerman, 2001). Transverse mode-coupling calculation using a simulated wake field was also used (Ohmi *et al.*, 2002). The instability threshold was found to be linearly proportional to the average electron density (i.e., N_0/s_b). Recently, particle-in-cell simulations based on strong-strong models were performed.

4. Preventive measures

Control of electron-cloud effects involves suppressing electron generation and enhancing Landau damping. The number of multipacting electrons can be effectively reduced by surface treatment of the vacuum pipe. Electrons in the injection region need to be guided to the collectors with a low backscattering yield (Tabata *et al.*,

1971). A beam-in-gap kicker can ensure a clean beam gap (Witkover *et al.*, 1999; Catalan-Lasheras, Lee, *et al.*, 2001). Vacuum ports can be screened, and steps in the vacuum pipe can be tapered to reduce peaked electric fields causing electron emission. A good vacuum can reduce electrons from gas ionization. Solenoids can be wound in straight sections to reduce multipacting (Funakoshi *et al.*, 2000). Electrodes can be installed around the ring to clear the electron cloud and to isolate areas of high electron concentration. Electron detectors need to be installed at locations susceptible to high electron concentration to monitor the production of electrons (Fig. 37).

Enhancement of Landau damping starts with the design of the machine. A large vacuum-pipe aperture is needed, especially at locations of high dispersion, to further increase momentum spread. A large rf voltage is required to provide sufficient momentum acceptance. Longitudinal painting can be used to expand the momentum spread of the injecting beam. Inductive inserts can be used to compensate for the space-charge effect, effectively increasing rf focusing (Koba *et al.*, 1999; Ng, Wildmans, *et al.*, 2001). Landau-damping octupoles (KEK PF and BEPC) were shown to raise the stability threshold. Lattice sextupole families (BEPC, SPS, KEKB, and SNS) can be used for chromatic adjustments, either to improve momentum acceptance (Tsoupas, Gardner, *et al.*, 2000) or to enhance damping. Finally, a fast, wideband feedback system can be implemented to damp instabilities.

A surface coating of TiN was shown to effectively suppress the electron flux by a factor of more than 100 at a coated section of the PSR (Fig. 44). The thickness of the coating, typically about 100 nm, is chosen to withstand bombardment from electrons during the lifetime of the machine operation. For critical elements, e.g., the ferrite of the extraction kicker inside the vacuum pipe (SNS), the pattern and thickness of the coating are selected to avoid eddy-current heating and to prevent changes in material properties. Measurements of TiN-coated surfaces indicated a reduction of secondary-emission yield (Y_{ee}) by more than half of a unit, possibly due to reentry of secondary electrons into the wall of craters created by the coating (Fig. 50) (He, 2003). A higher level of outgassing from the rougher coated surface may require additional vacuum pumping. Recent studies at CERN and ESRF showed that nonevaporable getter (NEG) film coating of TiZrV alloy reduces both secondary-emission yield and outgassing (Benvenuti *et al.*, 2001; Kersevan, 2002). Use of such a NEG film coating requires *in situ* baking of the coated vacuum chamber before accelerator operations. Planned, long-term bombardment with cold electrons further reduces the secondary-emission yield. Evidence of this “surface scrubbing” was seen at the SPS, KEKB, and PSR. The memory of the scrubbing may be preserved by a glow discharge in nitrogen (Jimenez, 2001).

Clearing electrodes were shown to suppress the electron multipacting at the CERN ISR. At the SNS accumulator ring, the beam position monitors around the

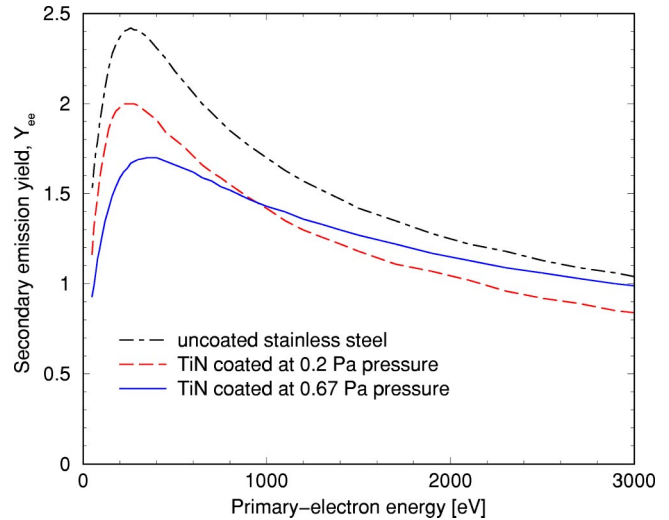


FIG. 50. (Color in online edition) Measured secondary-electron yield Y_{ee} as a function of the primary-electron energy for a perpendicular incidence and for various coating conditions of vacuum-pipe surfaces. Magnetron (dc) sputtering is used to coat the surfaces with 100 nm of TiN. Surfaces coated at a pressure of 0.67 Pa, which has a lower peak Y_{ee} but a higher outgassing rate compared with those coated at a pressure of 0.2 Pa, are used for the SNS ring (Sec. IV.D.1). Figure courtesy P. He, N. Hilleret, H. Hseuh, and R. Todd.

ring are designed also to be used as clearing electrodes, capable of applying a voltage of up to ± 1 kV. Such a voltage overcomes the energy gain due to the proton bunch [Eq. (45)]. A dedicated clearing electrode is implemented inside the stripping-foil assembly at the injection region.

Weak solenoids have been shown to effectively improve machine operation under the electron cloud at KEKB and PEP-II. In a short test section at the PSR, a weak solenoid was found to suppress the electron flux (f_e) by a factor of about 50. For future high-intensity synchrotrons, such solenoids could also be used in straight sections, like the collimation section, to suppress electron generation (Wei and Macek, 2002).

Present studies indicate that with preventive measures adopted to suppress electron generation and to enhance Landau damping, the impact of electron cloud can be minimized in the operation of next-generation high-intensity accelerators like the SNS ring.

E. Intrabeam scattering

Intrabeam scattering refers to two-body Coulomb scattering processes occurring between particles within the same bunch (Bjorken and Mtingwa, 1983; Martini, 1984; Piwinski, 1984; Parzen, 1987). Energy exchange and increases in temperature in the beam’s rest frame manifest themselves as variations in the beam’s emittance and momentum spread in the laboratory frame (Wei, 1999). The rates of emittance exchange and growth are linearly proportional to the number of particles N_0 in the beam, are strongly dependent

TABLE VIII. Examples of beam dynamics simulation codes and their functions used for the design of high-intensity circular accelerators (Sec. IV.F). Courtesy N. Malitsky.

Functions	UAL	ORBIT	FTPOT	MAD	MARYLIE	ACCSIM	SIMPSONS
Interface	PERL API	SuperCode	FTPOT	MAD	MARYLIE	ACCSIM	SIMPSONS
MAD elements	Yes	Yes	Yes	Yes	Yes	Yes	Yes
Errors	Yes	No	Yes	Yes	No	No	Yes
Tracking	Thin lenses	Matrices + nodes	Thin lenses	Lie algebra	Lie algebra	Matrices + nodes	Thin lenses
Mapping	Any order	Second order	Second order	Third order	Third order	Linear order	No
H Painting	Yes	Yes	No	No	No	Yes	Yes
Fringe Field	Yes (Maps)	No	No	No	Yes	No	No
Space Charge	3D	3D	No	No	No	2.5D	2D & 3D
Analysis (twiss ...)	Yes	No	Yes	Yes	Yes	No	No
Optimization (lattice ...)	No	No	No	Yes	Yes	No	No
Correction (orbit ...)	Yes	No	Yes	Yes	Some	No	No
Impedance	Yes	Yes	No	No	No	No	No
Collimator	Yes	Yes	No	No	No	Yes	No
Integration of lattices	Yes	No	No	No	No	No	No

($\sim q^4/A^2$) on the charge state of the particles, and are approximately inversely proportional to the six-dimensional phase-space area. Changes due to intra-beam scattering usually occur over a much longer time scale than the synchrotron's oscillation period. Therefore the effect is often negligible in a synchrotron of high repetition rate. Formulas in this section may be used for an order-of-magnitude estimate.

The rate of emittance and momentum variation is given by

$$\begin{bmatrix} \frac{1}{\sigma_p} \frac{d\sigma_p}{dt} \\ \frac{1}{\sigma_x} \frac{d\sigma_x}{dt} \\ \frac{1}{\sigma_y} \frac{d\sigma_y}{dt} \end{bmatrix} = \frac{q^4 N_0}{A^2} \frac{r_0^2 m_0 c^2 \mathcal{L}_c}{8 \gamma \epsilon_{Nx} \epsilon_{Ny} S_{rms}} F_i(\chi) \begin{bmatrix} n_b(1-d_i^2) \\ -a_i^2/2 + d_i^2 \\ -b_i^2/2 \end{bmatrix}, \quad (49)$$

where $\mathcal{L}_C \approx 20$ is the Coulomb logarithm, $\epsilon_{Nx,y} = \beta \gamma \sigma_{x,y}^2 / \beta_{x,y}$ is the normalized rms transverse emittance, $S_{rms} = \pi m_0 c^2 \beta \gamma \sigma_s \sigma_p / cA$ is the rms longitudinal bunch area in phase space, $\chi = (a_i^2 + b_i^2)/2$, $d_i = D \sigma_p / (\sigma_x^2 + D^2 \sigma_p^2)^{1/2}$, $a_i = \beta_x d_i / D \gamma$, $b_i = (\beta_y \sigma_x / \beta_x \sigma_y) a_i$, n_b is equal to 1 if the beam is azimuthally bunched and is equal to 2 if it is not. For azimuthally bunched beams, σ_s is the rms bunch length and N is the number of particles per bunch; for unbunched beams, N_0 is the total number of particles and $\sigma_s = \sqrt{\pi} R_0$. In Eq. (49), $F_i(\chi)$ is an analytic function given by

$$F_i(\chi) = \frac{-3 + (1 + 2\chi)I_i(\chi)}{1 - \chi}, \quad (50)$$

where

$$I_i(\chi) = \begin{cases} \frac{1}{\sqrt{\chi(\chi-1)}} \text{Arth} \sqrt{\frac{\chi-1}{\chi}} & \chi \geq 1 \\ \frac{1}{\sqrt{\chi(1-\chi)}} \arctan \sqrt{\frac{1-\chi}{\chi}} & \chi < 1. \end{cases} \quad (51)$$

F. Computer simulation codes

Computer simulation provides useful tools for designing synchrotrons. As the unknown regime of high beam intensity continues to be explored, simulation often is the only tool that provides insights into various collective mechanisms. Table VIII lists a collection of such design and simulation programs and their main functions: UAL (Unified Accelerator Libraries; Malitsky *et al.*, 1999); ORBIT (Galambos *et al.*, 1999), TEAPOT (Schachinger and Talman, 1987); MAD (Grote and Iselin, 1990); MARYLIE (Dragt *et al.*, 1999) ACCSIM (Jones *et al.*, 1990); and SIMPSONS (Machida, 1991).

The availability of large computing power using parallel processing and fast CPU's has facilitated the investigation of complicated, combined effects that are difficult or impossible to handle analytically (Fig. 51). Examples are 3D space-charge modeling in combination with longitudinal and transverse coupling impedance, and modeling electron clouds and electron-proton instability. Efforts are being made to validate these models experimentally (Galambos *et al.*, 2000).

V. FUTURE APPLICATIONS AND DEVELOPMENTS

Table IX lists some high-intensity applications, including spallation-neutron sources, neutrino-factory proton

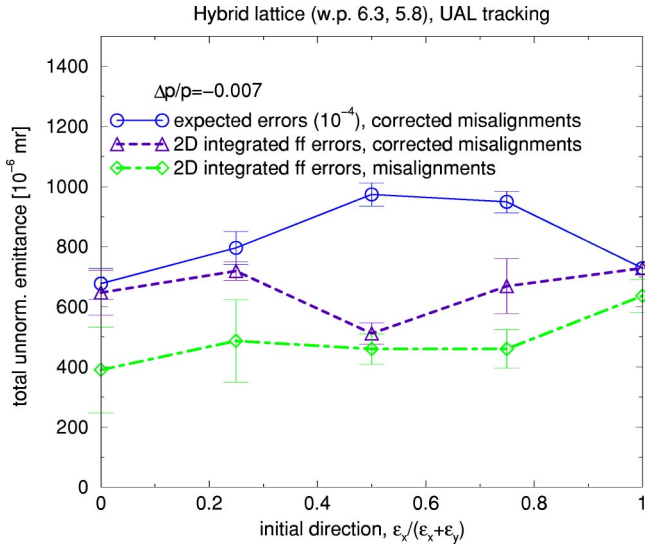


FIG. 51. (Color in online edition) Dynamic aperture obtained from 6-D UAL element-by-element computer tracking for the SNS accumulator ring at the nominal working point. Each data point gives the mean and standard deviation obtained using 10 random seeds. The beam momentum spread is $\pm 0.7\%$. Effects of magnetic errors, misalignments, and limiting physical apertures are considered (Sec. IV.F).

drivers (NFPD), muon-collider drivers, nuclear transmutation, and energy amplifiers (EA), as discussed in many review papers (Weng, 1997; Lee, 1998; FNAL PD, 2000; Hirata *et al.*, 2000; Chou and Wei, 2001). For pulsed applications, the accumulator ring (AR) scenario is advantageous because loss is minimized (no main-magnet ramping, better magnet-field quality, and shorter storage time available for developing instability). On the other hand, rapid-cycling synchrotrons (RCS) are economical for energy and power upgrades (multiring cluster, multipurpose), and realizing a short bunch length is easier. Figure 3 shows the beam energy, current, and power of some of the world’s high-intensity proton synchrotrons. In addition, proton synchrotrons are also used for medical applications (Coutrakon *et al.*, 1999; Peggs *et al.*, 2001) and for accelerating polarized beams for spin-physics studies (Khoe *et al.*, 1975; Roser, 1995) Fixed-field alternating-gradient (FFAG) synchrotrons are identified as promising candidates for high-duty-factor acceleration (Kerst *et al.*, 1955; Symon, 1955; Cole *et al.*, 1957; Kolomensky *et al.*, 1957; Ohkawa, 1958; MURA, 1964; Aiba *et al.*, 2000).

VI. CONCLUSIONS AND DISCUSSION

With five decades of exploration and discovery, synchrotrons and accumulators have advanced to meet the

TABLE IX. Beam parameters of some existing and proposed proton accelerator facilities (Sec. V); RCS, rapid-cycling synchrotron; AR, accumulator ring; EA, energy amplifier; PD, proton driver; Linac, linear accelerator.

Machine	Intensity (10 ¹³ /pulse)	Rep. rate (Hz)	Flux ^a (10 ²⁰ /year)	Energy (GeV)	Power (MW)	Type
Existing:						
ISIS (RAL)	2.5	50	125	0.8	0.16	RCS
AGS (BNL)	7	0.5	3.5	24	0.13	RCS
PSR (LANL)	2.5	20	50	0.8	0.064	AR
MiniBooNE (FNAL) ^b	0.5	7.5	3.8	8	0.05	RCS
NuMI (FNAL)	3	0.5	1.5	120	0.3	RCS
CNGS (CERN)	4.8	0.17	0.8	400	0.5	RCS
Under construction:						
SNS	14	60	840	1	1.4	AR
J-PARC 3 GeV	8	25	200	3	1	RCS
J-PARC 50 GeV	32	0.3	10	50	0.75	RCS
Proposed:						
ESS	46.8	50	2340	1.334	5	AR (2 ring)
CONCERT	234	50	12000	1.334	25	AR (2 ring)
AAA (LANL)		cw	62500	1	100	Linac
AHF (LANL)	3	0.04	0.03	50	0.003	RCS
EA (CERN)		cw	12500	1	20	Cyclotron
PD (FNAL) I	3	15	45	16	1.2	RCS
PD (FNAL) II	10	15	150	16	4	RCS
PD (BNL) I	10	2.5	25	24	1	RCS
PD (BNL) II	20	5	100	24	4	RCS
PD/SPL (CERN)	23	50	1100	2.2	4	AR (2 ring)
PD (RAL) 15 GeV	6.6	25	165	15	4	RCS (2 ring)
PD (RAL) 5 GeV	10	50	500	5	4	RCS (2 ring)

^a1 year is taken to be 10⁷ s.

^bIncluding planned improvements.

challenge of the next-generation applications. Difficulties encountered in progress demand state-of-the-art knowledge and technology from the physics community and the industry. Accelerator physics and technologies developed at the high-intensity frontier in turn stimulate the evolution of modern accelerators.

A key challenge in achieving a high-intensity performance is to minimize uncontrolled beam loss. Beam losses are attributed to single-particle and multiparticle phenomena. Leading single-particle phenomena include injection-related losses, magnetic nonlinearities, and resonance crossing. Leading multiparticle phenomena include space-charge effects, instabilities due to coupling impedances, and electron-cloud effects.

Rapid-cycling synchrotrons have lower injection energy and fewer accumulated particles. On the other hand, fixed-energy accumulators do not accelerate beam in the ring, and the beam duration time is short. In designing a new high-intensity synchrotron, some basic questions must be answered: (1) Is it preferable to use a rapid-cycling synchrotron, or a fixed-energy accumulator? (2) Should there be two rings to reach a high combined power, or one ring of larger circumference? (3) Will the beam be injected at a dispersive region, or a nondispersive region? (4) What is the superperiodicity of the ring's lattice, and how are injection, rf, collimation, and extraction to be arranged? (5) What is the ramping scheme for a rapid-cycling synchrotron? Answers to these questions are closely related to considerations of beam loss. Above all, having a large transverse vacuum-pipe aperture and long, uninterrupted straight sections are the two most important aspects that must be considered from the very beginning.

The most distinctive features of the newer high-intensity rings, like the SNS accumulator and the J-PARC RCS ring, are a large vacuum-pipe aperture and long straight sections. Based on an optimized accelerator layout, accelerator physics and technological challenges must be met to achieve high-intensity, high-beam-power operations. The following problems are among a long list of important accelerator-physics topics that needs to be explored: (1) time structure and resonance behavior of beam loss; (2) beam-halo dynamics, diagnostics, and collimation; (3) calculation, measurement, and minimization of coupling impedance; (4) combined instability behavior of space charge and other coupling impedances; (5) electron-cloud generation and instability development; (6) resonance excitation and correction of magnetic nonlinearities; and, (7) development of large-capacity computer simulation that incorporates lattice nonlinearities, space charge, coupling impedances, injection schemes, collimation, electron-cloud effects, and energy ramping.

Technological challenges are primarily associated with rapid-cycling synchrotrons: (1) rf cavities of high acceleration gradient (near 50 MV/m at a frequency range of 1–20 MHz); (2) laminated magnets with water-cooled, stranded coils to accommodate a high repetition rate (up to 50 Hz) and a high field (up to 1.5 T); (3) vacuum pipe and thin shielding that possess high impedance to eddy

currents but low impedance to the beam; (4) dual-frequency resonant power supplies or fast-switching, programmable power supplies for the magnets; and, (5) magnetic-field tracking at a level better than 10^{-3} between the dipole and quadrupole magnets. Other challenges that are common to both rapid-cycling synchrotrons and accumulator rings are the following: (6) long-lifetime, heat- and stress-resistant stripping foils; (7) foil-free injection schemes based on resonance lasers; (8) kickers and their pulse-forming networks, with a fast rise time and field uniformity; (9) electron collection and suppression using TiN coating and surface treatments, guiding magnetic field, clearing electrodes, and solenoids; (10) feedback systems with a wide frequency bandwidth and power; (11) heat and radiation resistance of devices located in high-beam-loss region; and, (12) diagnostics and machine-protection systems that are sensitive to the dynamics of the beam and have a fast response to beam-loss detection.

In this paper, the author has reviewed the design and operational experience of existing and proposed proton facilities and summarized physical and engineering issues limiting the efficiency of high-intensity synchrotrons and accumulators. The topics covered include lattice design, geometric and momentum acceptance, beam-halo cleaning, injection, acceleration, extraction, magnet system, power supplies, rf system, transport lines, and machine protection and diagnostics. Beam dynamics pertaining to high-intensity performance, including tune shift and resonance control, beam-loss models, space-charge control, collective effects, and electron-cloud effects, have also been reviewed. Detailed discussions of each can be found in the corresponding references.

At a time when new accelerator projects at the high-energy frontier are experiencing increasing difficulties in gaining financial support, it is interesting to note that projects at the high-intensity frontier are flourishing around the world. Demands for such accelerators extend to spallation-neutron production, waste transmutation, energy generation, neutrino physics, and muon physics. The research, development, and construction of the Spallation Neutron Source (SNS) in the United States and the Proton Accelerator Research Complex (J-PARC) in Japan are paving the way towards future projects of high-intensity synchrotrons and accumulators.

ACKNOWLEDGMENTS

It would not have been possible to complete this article without generous help from the author's colleagues and friends. In particular, the author would like to thank G. Arduini, R. Baartman, A. Browman, R. Capi, M. Chanel, W. Chou, A. Fedotov, M. Furman, C. Gardner, I. Gardner, R. Garoby, O. Gröbner, I. Hofmann, Y. Irie, S. Ivanov, M. Kinsho, T. Linnecar, H. Ludewig, R. Macek, S. Machida, Y. Mori, M. Pivi, M. Plum, C. Prior, G. Rees, T. Roser, F. Ruggiero, H. Schönauer, E. Shaposhnikova, K. Takayama, P. Thieberger, P. Wan-

derer, C.M. Warsop, R. Webber, and the SNS team for generously providing information. The author also would like to thank J. Galambos, H. Hahn, S. Koscielniak, T. Linnekar, R. Ma, Y. Papaphilippou, C. Prior, G. Rees, A. M. Sessler, A. Woodhead, and B. Zotter for carefully reading and correcting the manuscript, and thank A. Aleksandrov, J. Beebe-Wang, M. Blaskiewicz, J. Brodowski, P. Cameron, N. Catalan-Lasheras, A. Chao, E. D. Courant, S. Cousineau, G. Danby, V. Danilov, D. Davino, A. Fedotov, D. Finley, R. Gluckstern, M. Hemmer, S. Henderson, J. Holmes, H. Hseuh, J. Jackson, A. Jain, S. Kim, R. Lambiase, Y. Y. Lee, D. Lowenstein, N. Malitsky, W. Meng, J. Mi, G. Parzen, S. Peggs, D. Raparia, J. Sandberg, K. Schindl, R. Siemann, N. Simos, R. Talman, S. Tepikian, D. Trbojevic, N. Tsoupas, J. Tuozzolo, W. T. Weng, S. Y. Zhang, and F. Zimmermann for many useful discussions. This work was performed under the auspices of the U.S. Department of Energy. The Spallation Neutron Source Project is managed by UT-Battelle, LLC, under Contract No. DE-AC05-00OR22725 for the U.S. Department of Energy. SNS is a partnership of six national laboratories: Argonne, Brookhaven, Jefferson, Lawrence Berkeley, Los Alamos, and Oak Ridge.

ABBREVIATIONS AND ACRONYMS

AAA	Advanced Accelerator Applications, LANL		
AGS	Alternating Gradient Synchrotron		
AHF	Advanced Hydrotest Facility, LANL		
ANL	Argonne National Laboratory		
ANSYS	Computer program for mechanical engineering simulations		
AR	accumulator ring		
BEPC	Beijing Electron Positron Collider		
BIG	beam-in-gap		
BNL	Brookhaven National Laboratory		
BPM	beam position monitor		
CERN	European Organization for Nuclear Research		
CNGS	CERN Neutrinos to Gran Sasso		
CONCERT	Combined Neutron Center for European Research and Technology		
CPU	central processing unit		
DOE	Department of Energy, U.S.		
DTL	drift-tube linac		
EA	energy amplifier		
EM	electromagnetic		
<i>e-p</i>	electron-proton		
EPS-IGA	European Physical Society Interdivisional Group on Accelerators		
ESRF	European Synchrotron Radiation Facility, France		
ESS	European Spallation Source		
FFAG	fixed-field alternating-focusing		
FNAL	Fermi National Accelerator Laboratory		
FODO	focusing/defocusing lattice structure with drift sections		
FWHM	full width at half maximum		
H	horizontal		
H ⁻	hydrogen ion with a negative charge		
H ⁺	hydrogen ion with a positive charge		
H ⁰	neutral hydrogen		
HEBT	high-energy beam transport		
Hz	Hertz		
IBS	intrabeam scattering		
IEEE	Institute of Electrical and Electronics Engineers, Inc.		
IGBT	insulated-gate bipolar transistor		
IPM	ionization-profile monitor		
IPNS	Intense Pulsed Neutron Source (ANL)		
ISIS	spallation neutron facility at RAL		
ISR	Intersecting Storage Ring, CERN		
JAERI	Japan Atomic Energy Research Institute		
JHF	Japan Hadron Facility		
J-PARC	Japan Proton Accelerator Research Complex		
KAON	Kaon, Antiproton, Other Hadron Neutrino Factory		
KEK	High Energy Accelerator Research Organization (Japan)		
KEKB	KEK <i>B</i> -factory facility		
L	longitudinal		
LANL	Los Alamos National Laboratory		
LBNL	Lawrence Berkeley National Laboratory		
LHC	Large Hadron Collider		
linac	linear accelerator		
MARS	computer program for particle-transport and collimation calculation		
MCNP	Monte Carlo N-Particle, computer program for particle-transport calculation		
MI	Main Injector (Fermilab)		
mrad	milliradian		
ms	10 ⁻³ second		
mSv/hour	10 ⁻³ sievert per hour		
MURA	Midwest University Research Association, Madison, Wisconsin		
NEG	nonevaporable getter		
OPERA	computer program for magnetic-fields calculation		
ORNL	Oak Ridge National Laboratory		
PD	proton driver		
PEP-II	SLAC <i>B</i> -factory facility		
PF	photon factory		
PFN	pulse-forming network		
PIC	particle in cell		
ppp	particles per pulse		
PS	Proton Synchrotron (CERN)		
PSR	Proton Storage Ring, Los Alamos National Laboratory		
RAL	Rutherford-Appleton Laboratory		
RCS	rapid-cycling synchrotron		
rf	radio frequency		
RFQ	radio-frequency quadrupole		
RHIC	Relativistic Heavy Ion Collider		
rms	root-mean-squared		
RTBT	ring-to-target beam transport		
SEY	secondary-emission yield		
SI	Système International, based on meter, kilogram, second, ampere (MKSA)		

SLAC	Stanford Linear Accelerator Center	L_c	FODO cell length
SNS	Spallation Neutron Source	\mathcal{L}_c	intrabeam scattering Coulomb logarithm
SPL	Superconducting Proton Linac (CERN)	m, n	integers
SPS	Super Proton Synchrotron (CERN)	m_0	rest mass of proton
SSC	Superconducting Super Collider	m_e	rest mass of electron
Sv	sievert; 100 rem	M	number of lattice superperiods
V	vertical	N_0	number of protons per bunch
Ω	ohm	P	pressure
LIST OF SYMBOLS			
Roman letters			
a	average beam radius	q	electric-charge number
a_2	skew quadrupole strength	r_0	classical radius of proton; $e^2/4\pi\epsilon_0 m_0 c^2$
a_i, b_i, d_i	intrabeam scattering geometric factors	r_e	classical radius of electron; $e^2/4\pi\epsilon_0 m_e c^2$
a_n	$n=0,1,2,\dots$; magnetic-field skew-multipole coefficient	R_0	ring circumference divided by 2π
A_{im}	Laslett tune-shift factor	s	azimuthal displacement along ring
A_{s1}, A_{s2}	Lorentz stripping coefficients	S	longitudinal phase-space area of the bunch
b	average radius of vacuum pipe	s_b	center-to-center distance between subsequent bunches
b_n	$n=0,1,2,\dots$; magnetic-field normal-multipole coefficient	S_{rms}	rms longitudinal bunch area
B	magnetic-field amplitude	t	time in laboratory frame
\tilde{B}	magnetic-field (frequency domain)	T_c	characteristic transition-crossing time
\dot{B}	rate of change of magnetic field	T_{mw}	duration time of microwave instability near transition
B_0	nominal guiding magnetic field	T_{nl}	chromatic nonlinear time near transition
$B_{0\rho}$	rigidity of a particle	V_{rf}	rf peak voltage
B_f	ratio of average and peak proton density; $B_f \leq 1$	w_r	width of a resistive loop
B_x	horizontal component of magnetic field	x	horizontal displacement
B_y	vertical component of magnetic field	x'	dx/ds
c	speed of light	x_{sep}	transverse displacement at the septum
C_n	$n=1,2,\dots$; multipole tune-shift coefficients	X	normalized horizontal displacement, $X \equiv x/\sqrt{\beta_x}$
C_l	envelope-oscillation coefficient	X'	$dX/d\mu = (\alpha x + \beta x')/\sqrt{\beta_x}$
d_w	thickness of vacuum pipe wall	y	vertical displacement
D	lattice dispersion function	y'	dy/ds
D_x or D_H	horizontal dispersion function	Y	normalized vertical displacement, $Y \equiv y/\sqrt{\beta_y}$
D_y or D_V	vertical dispersion function	Y'	$dY/d\mu = (\alpha y + \beta y')/\sqrt{\beta_y}$
D^+	maximum dispersion	Y_{ee}	electron secondary-emission yield upon electron impact
dP_r/ds	power generated in a resistive loop	Y_{ep}	electron secondary-emission yield upon proton impact
e	unit electric charge	Y_{ep}^{max}	maximum electron secondary-emission yield upon proton impact
\vec{E}	electric field (frequency domain)	z	longitudinal displacement
E_s	synchronous energy of the beam	Z_{\parallel}	longitudinal coupling impedance
E_s^{max}	proton energy corresponding to maximum secondary emission of electrons	Z_{\perp}	transverse coupling impedance
f_{sc}	space-charge form factor	Z_0	$(\epsilon_0 c)^{-1} = 377$ (ohms)
g	gap height of dipole magnet	$Z_{\parallel}^{\text{rw}}, Z_{\perp}^{\text{rw}}$	coupling impedances due to resistive wall
g_0	space-charge geometric factor	$Z_{\parallel}^{\text{sc}}, Z_{\perp}^{\text{sc}}$	coupling impedances due to space charge
h	rf harmonic number	Greek letters and other symbols:	
h_r	height of a resistive loop	$ $	absolute value
I	average beam current in ring	$\langle \rangle$	average value
\hat{I}	peak beam current	α_0	momentum compaction factor, $\alpha_0 = \gamma_T^2$
\tilde{I}	beam current in frequency domain	α_1	first-order nonlinear momentum compaction factor
j	$\sqrt{-1}$	α_{\perp}	transverse α lattice function
k	excited resonance harmonics	α_e	electron survival rate in the bunch gap
K_{\perp}	transverse-focusing strength	α_x	horizontal lattice function
ΔK_{\perp}	deviation in transverse-focusing strength	$\alpha_{x,i}$	horizontal lattice function of injecting beam
$K_{\perp}^{(l)}$	strength of $2l$ th pole error	β	relativistic factor; βc is beam velocity
l	resonance order		

β'	$d\beta/ds$	ν_x	horizontal tune
β_{\perp}	transverse amplitude function	ν_y	vertical tune
β_{\perp}^+	maximum transverse amplitude function in FODO cell	$\nu_{x,0}, \nu_{y,0}$	unperturbed horizontal or vertical tune
β_{\perp}^-	minimum transverse amplitude function in FODO cell	ξ_{\perp}	transverse chromaticity of the ring
β_e	electron relativistic factor; $\beta_e c$ is the electron velocity	ρ_m	molecular density
β_{kick}	transverse amplitude function at the kicker	ρ_r	volume resistivity
β_{sep}	transverse amplitude function at the septum	σ_p	rms spread in relative momentum deviation $\Delta p/p$
β_x or β_H	horizontal amplitude function	σ_{ion}	ionization cross section
$\beta_{x,i}$	horizontal amplitude function of injecting beam	σ_{ϕ}	rms spread in rf phase
β_y or β_V	vertical amplitude function	ϕ	rf phase
γ	relativistic factor; $\gamma = (1 - \beta^2)^{-1/2}$	ϕ_c	bending angle per FODO cell
$\dot{\gamma}$	rate of γ variation in time	ϕ_s	synchronous rf phase
γ_T	relativistic factor corresponding to the transition energy	ψ_x	horizontal betatron-oscillation phase
$\dot{\gamma}_T$	rate of γ_T variation in time during transition jump	ψ_y	vertical betatron-oscillation phase
$\gamma_{x,y}$	horizontal and vertical lattice functions	ω_e	electron bounce frequency
ΔE_e	energy gained by electron	ω_s	synchronous angular-revolution frequency
δ_s	skin depth		
$\Delta p/p$	relative momentum deviation		
ΔS	change in longitudinal phase-space area of the bunch		
$\Delta x'_0$	change of x' due to main magnetic field		
$\Delta x'_{fr}$	change of x' due to fringe field		
$\Delta\mu$	betatron phase advance		
$\Delta\nu$	transverse tune shift		
$\Delta\nu^{(m,n)}$	stopband width		
$\Delta\nu_{sc}$	transverse incoherent space-charge tune shift		
$\Delta\nu_{x,y}$	horizontal or vertical tune shift		
$\Delta\nu_{\text{coh}}$	coherent tune shift		
ϵ_{\perp}	transverse unnormalized (or geometric) emittance		
ϵ_{rms}	rms transverse emittance		
ϵ_x	horizontal unnormalized (or geometric) emittance		
$\epsilon_{x,i}$	horizontal unnormalized (or geometric) emittance of injecting beam		
ζ_m	multibunch electron-cloud multipacting parameter		
ζ_s	single-bunch electron-cloud multipacting parameter		
η	phase-slip factor		
η_e	electron-neutralization factor		
η_x	horizontal dispersion function		
η_y	vertical dispersion function		
θ_g	grazing angle		
θ_{kick}	transverse momentum deflection from the kicker		
κ	resonance strength		
λ_e	electron line density		
λ_s	mean decay length due to Lorentz stripping		
μ	permeability		
μ_0	permeability in vacuum		
μ_c	betatron phase advance per FODO cell		
ν_0	unperturbed transverse tune		

REFERENCES

Note: Many of the Proceedings listed here are also posted on the Joint Accelerator Conference Website (JACoW), <http://accelconf.web.cern.ch/AccelConf/top-page.html>

- Abell, D., Y. Y. Lee, and W. Meng, 2000, in *Proceedings of the 7th European Particle Accelerator Conference*, Vienna, edited by J.-L. Laclare *et al.* (Austrian Academy of Science Press, Vienna), p. 2107.
- Aiba, M., *et al.*, 2000, in *Proceedings of the 7th European Particle Accelerator Conference*, Vienna, edited by J.-L. Laclare *et al.* (Austrian Academy of Science Press, Vienna), p. 581.
- Alessi, R., and K. Prelec, 1991, in *Conference Record of the 1991 IEEE Particle Accelerator Conference, Accelerator Science and Technology*, San Francisco, edited by the IEEE staff (IEEE, New York), Vol. 3, p. 1913.
- Allan, M., and S. F. Wong, 1978, *Phys. Rev. Lett.* **41**, 1795.
- ANSYS, Web site: <http://www.ansys.com/> (ANSYS Inc. Corporate, USA).
- Arduini, G., *et al.*, 2000, in *Proceedings of the 7th European Particle Accelerator Conference*, Vienna, edited by J.-L. Laclare *et al.* (Austrian Academy of Science Press, Vienna), p. 1611.
- Arduini, G., K. Cornelis, W. Hoefle, G. Rumolo, and F. Zimmermann, 2001, in *Proceedings of the 2001 Particle Accelerator Conference*, Chicago, edited by P. Lucas and S. Webber (IEEE, Piscataway, NJ), p. 1883.
- Baartman, R., 1998, in *Workshop on Space Charge Physics in High-Intensity Hadron Rings*, AIP Conf. Proc. No. 448, edited by A. U. Luccio and W. T. Weng (AIP, Melville, NY), p. 56.
- Bardeen, J., L. N. Cooper, and R. Schrieffer, 1957, *Phys. Rev.* **108**, 1175.
- Beebe-Wang, J., Y. Y. Lee, D. Raparia, J. Wei, C. R. Prior, and S. Machida, 2000, in *Proceedings of the 7th European Particle Accelerator Conference*, Vienna, edited by J.-L. Laclare *et al.* (Austrian Academy of Science Press, Vienna), p. 1465.
- Benvenuti, C., P. Chigiato, P. Costa Pinto, A. Escudeiro Santana, T. Hedley, A. Mongelluzzo, V. Ruzinov, and I. Wevers, 2001, *Vacuum* **60**, 57.

- Biryukov, V., V. I. Kotov, and Yu. A. Chesnokov, 1997, *Crystal Channeling and its Applications at High Energy Accelerators* (Springer, Heidelberg/New York).
- Bjorken, J., and S. Mtingwa, 1983, Part. Accel. **13**, 115.
- Blaskiewicz, M., 1998, Phys. Rev. ST Accel. Beams **1**, 044201.
- Blaskiewicz, M., 2000, in *Proceedings of the 7th European Particle Accelerator Conference*, Vienna, edited by J.-L. Laclare et al. (Austrian Academy of Science Press, Vienna), Vol. 4, p. 1110.
- Blaskiewicz, M., et al., 1999, in *Proceedings of the 1999 Particle Accelerator Conference*, New York, edited by A. Luccio and W. MacKay (IEEE, Piscataway, NJ), Vol. 4, p. 2280.
- Blumburg, L. N., and Y. Y. Lee, 1996, BNL Technical note SNS/3.
- Boardman, B., 1982, Ed., *Spallation Neutron Source: Description of Accelerator and Target*, Rutherford Appleton Laboratory Report RL 82-006.
- Boine-Frankenheim, O., and I. Hofmann, 2000, Phys. Rev. ST Accel. Beams **3**, 104202.
- Borovsky, J. E., D. J. McComas, and B. L. Barraclough, 1988, Nucl. Instrum. Methods Phys. Res. B **30**, 191.
- Boussard, D., 1975, CERN Report Lab II/RF/Int./75-2.
- Boussard, D., 1998, in *Handbook of Accelerator Physics and Engineering: A Compilation of Formulae and Data*, edited by A. Chao and M. Tigner (World Scientific, Singapore), p. 108.
- Brennan, J. M., et al., 1994, in *Proceedings of the 4th European Particle Accelerator Conference*, London, edited by V. P. Suller and Ch. Petit-Jean-Genaz (World Scientific, Singapore), p. 1897.
- Brodowski, J., 2000, private communication.
- Brodowski, J., 2002, private communication.
- Bryant, P. J., and K. Johnsen, 1993, *The Principles of Circular Accelerators and Storage Rings* (Cambridge University Press, Cambridge, UK).
- Bryant, P. J., and E. Klein, 1992, CERN Report SL/92-40 (AP).
- Burtin, G., J. Camas, G. Ferioli, R. Jung, J. Koopman, R. Perret, A. Variola, and J. M. Vouillot, 2000, in *Proceedings of the 7th European Particle Accelerator Conference*, Vienna, edited by J.-L. Laclare et al. (Austrian Academy of Science Press, Vienna), p. 256.
- Carrigan, R. A., Jr., 1987, in *Relativistic Channeling*, edited by R. Carrigan and J. Ellison (Plenum, New York).
- Caspers, F., et al., 2000, in *Proceedings of the 7th European Particle Accelerator Conference*, Vienna, edited by J.-L. Laclare et al. (Austrian Academy of Science Press, Vienna), p. 376.
- Catalan-Lasheras, N., J. Galambos, N. Holtkamp, D. Raparia, R. Shafer, J. Staples, J. Stovall, E. Tanke, T. Wangler, and J. Wei, 2001, ORNL Technical Note SNS/AP/7.
- Catalan-Lasheras, N., Y. Y. Lee, H. Ludewig, N. Simos, and J. Wei, 2001, Phys. Rev. ST Accel. Beams **4**, 010101.
- Chao, A., 1993, *Physics of Collective Beam Instabilities in High Energy Accelerators* (Wiley, New York).
- Chao, A., and M. Tigner, 1998, Eds., *Handbook of Accelerator Physics and Engineering: A Compilation of Formulae and Data* (World Scientific, Singapore).
- Cho, Y., et al., 1996, in *Proceedings of the 5th European Particle Accelerator Conference*, Sitges, Spain, edited by S. Myers, A. Pachaco, R. Pascual, and Ch. Petit-Jean Genex (Institute of Physics, Bristol), p. 521.
- Chou, W., and J. Wei, 2001, in *Proceedings of Snowmass 2001, The Future of Particle Physics*, edited by N. Graf (Stanford Linear Accelerator Center, Stanford, CA), p. M6001.
- Christofilos, N. C., 1950, unpublished.
- Christofilos, N. C., et al., 1964, Rev. Sci. Instrum. **35**, 886.
- Cole, F. T., et al., 1957, Rev. Sci. Instrum. **28**, 403.
- CONCERT, 2001, *Intermediate Report on the Feasibility Study of CONCERT*, CEA Saclay Report.
- Connolly, R., P. Cameron, T. J. Shea, and R. Witkover, 1999, BNL Technical Note SNS/59.
- Courant, E. D., A. A. Garren, and U. Wienands, 1991, in *Conference Record of the 1991 IEEE Particle Accelerator Conference, Accelerator Science and Technology*, San Francisco, edited by the IEEE staff (IEEE, New York), Vol. 5, p. 2829.
- Courant, E. D., M. S. Livingston, and H. S. Snyder, 1952, Phys. Rev. **88**, 1190.
- Courant, E. D., and H. S. Snyder, 1958, Ann. Phys. (N.Y.) **3**, 1.
- Cousineau, S., J. A. Holmes, and N. Catalan-Lasheras, 2001, in *Proceedings of the 2001 Particle Accelerator Conference*, Chicago, edited by P. Lucas and S. Webber (IEEE, Piscataway, NJ), Vol. 3, p. 1723.
- Coutrakon, G., J. M. Slater, and A. Ghebremedhin, 1999, in *Proceedings of the 1999 Particle Accelerator Conference*, New York, edited by A. Luccio and W. MacKay (IEEE, Piscataway, NJ), Vol. 1, p. 11.
- Danby, G., J. Jackson, and C. Spataro, 1999, in *Proceedings of the 1999 Particle Accelerator Conference*, New York, edited by A. Luccio and W. MacKay (IEEE, Piscataway, NJ), Vol. 5, p. 3333.
- Danilov, V., A. Aleksandrov, J. D. Galambos, D. Jeon, J. A. Holmes, and D. K. Olsen, 1999, in *Workshop on Instabilities of High-Intensity Hadron Beams in Rings*, AIP Conf. Proc. No. 496, edited by T. Roser and S. Y. Zhang (AIP, Melville, NY), p. 315.
- Danilov, V., A. Aleksandrov, J. Wei, and M. Blaskiewicz, 2001, in *Proceedings of the 2001 Particle Accelerator Conference*, Chicago, edited by P. Lucas and S. Webber (IEEE, Piscataway, NJ), Vol. 3, p. 1749.
- Danilov, V., S. Henderson, J. A. Holmes, and A. Burov, 2001, Phys. Rev. ST Accel. Beams **4**, 120101.
- Davidson, R. C., H. Qin, and P. J. Channell, 1999, Phys. Rev. ST Accel. Beams **2**, 074401.
- Davino, P., H. Hahn, and Y. Y. Lee, 2002, in *Proceedings of European Particle Accelerator Conference*, Paris, edited by T. Garvey et al. (EPS-IGA and CERN, Geneva), p. 1467.
- DeLuca, W. H., 1969, IEEE Trans. Nucl. Sci. **NS-16**, 813.
- Dragt, A. J., D. R. Douglas, E. Forest, F. Neri, L. M. Healy, P. Schütt, and J. van Zeijts, 1999, *MARYLIE 3.0 User's Manual* (University of Maryland, Physics Department Report).
- Edwards, D. A., and M. J. Syphers, 1993, *An Introduction to the Physics of High Energy Accelerators* (Wiley, New York).
- Edwards, D. A., and L. C. Teng, 1973, IEEE Trans. Nucl. Sci. **NS-20**, 885.
- ESS, 2002, *The European Spallation Source Project Technical Report* Web site: <http://essnts.ess.kfa-juelich.de/The ESS Project> (ESS Council).
- Fedotov, A. V., D. T. Abell, Y. Y. Lee, N. Malitsky, Y. Papa-philippou, and J. Wei, 2000, in *Proceedings of the 7th European Particle Accelerator Conference*, Vienna, edited by J.-L. Laclare et al. (Austrian Academy of Science Press, Vienna), p. 1492.
- Fedotov, A. V., M. Blaskiewicz, J. Wei, V. V. Danilov, J. A. Holmes, and A. Shishlo, 2002, in *Proceedings of the 8th European Particle Accelerator Conference*, Paris, edited by T. Garvey et al. (EPS-IGA and CERN, Geneva), p. 1350.

- Fedotov, A. V., R. L. Gluckstern, and J. Wei, 2001, in *Proceedings of the 2001 Particle Accelerator Conference*, Chicago, edited by P. Lucas and S. Webber (IEEE, Piscataway, NJ), p. 2851.
- Fedotov, A. V., and I. Hofmann, 2002, *Phys. Rev. ST Accel. Beams* **5**, 024202.
- FNAL PD, 2000, *The Proton Driver Design Study* Fermilab-TM-2136 (Fermilab, Batavia, IL).
- Forest, E., 1998, *Beam Dynamics, A New Attitude and Framework* (Harwood Academic, Chur, Switzerland).
- Franchetti, G., and I. Hofmann, 2000, in *Proceedings of the 7th European Particle Accelerator Conference*, Vienna, edited by J.-L. Laclare *et al.* (Austrian Academy of Science Press, Vienna), p. 1292.
- Fujieda, M., *et al.*, 1999, in *Proceedings of the 1999 Particle Accelerator Conference*, New York, edited by A. Luccio and W. MacKay (IEEE, Piscataway, NJ), Vol. 2, p. 857.
- Funakoshi, Y., *et al.*, 2000, in *Proceedings of the 7th European Particle Accelerator Conference*, Vienna, edited by J.-L. Laclare *et al.* (Austrian Academy of Science Press, Vienna), Vol. 1, p. 28.
- Furman, M., 1998, in *Handbook of Accelerator Physics and Engineering: A Compilation of Formulae and Data*, edited by A. Chao and M. Tigner (World Scientific, Singapore), p. 438.
- Furman, M. A., and G. R. Lambertson, 1997, *KEK Proceedings 97-17*, edited by Y. H. Chin (KEK, Japan), p. 170.
- Galambos, J., V. Danilov, D. Jeon, J. A. Holmes, D. K. Olsen, F. Neri, and M. Plum, 2000, *Phys. Rev. ST Accel. Beams* **3**, 034201.
- Galambos, J. D., J. A. Holmes, D. K. Olsen, A. U. Luccio, and J. Beebe-Wang, 1999, *ORBIT User's Manual* (Oak Ridge National Laboratory, Oak Ridge, TN).
- Gardner, C., G. Danby, J. W. Glenn, J. Jackson, A. Soukas, W. van Asselt, C. Whalen, and Y. Shoji, 1994, in *Proceedings of the 4th European Particle Accelerator Conference*, London, edited by V. P. Suller and Ch. Petit-Jean Genaz (World Scientific, Singapore), p. 979.
- Garoby, R., 1998, in *Handbook of Accelerator Physics and Engineering: A Compilation of Formulae and Data*, edited by A. Chao and M. Tigner (World Scientific, Singapore), p. 284.
- Gluckstern, R. L., 1970, in *Proceedings of the 1970 Linear Accelerator Conference*, edited by M. R. Tracy (Fermilab, Batavia, IL), p. 811.
- Griffin, J., J. MacLachlan, A. G. Ruggiero, and K. Takayama, 1983, *IEEE Trans. Nucl. Sci.* **NS-30**, 2630.
- Gröbner, A., 1977, in *Proceedings of the 1977 International Conference on High Energy Accelerators*, Protvino, edited by Yu. M. Ado, A. G. Afonin, V. I. Gridasov, A. F. Dunaitsev, E. A. Mjae, and A. A. Naumov (Institute of High Energy Physics, Protvino, USSR), p. 277.
- Gröbner, A., 1997, in *Proceedings of the 1997 Particle Accelerator Conference*, Vancouver, B. C., edited by M. Comyn, M. K. Craddock, M. Reiser, and J. Thomson (IEEE, Piscataway, NJ), p. 3589.
- Gröbner, A., and R. Calder, 1973, *IEEE Trans. Nucl. Sci.* **NS-20**, 760.
- Grote, H., and F. C. Iselin, 1990 CERN Report CERN/SL/90-13.
- Guignard, G., 1975, CERN Report CERN ISR-MA/75-23; ISR-MA/75-35.
- Guo, Z. Y., *et al.*, 1998, in *Proceedings of the 1st Asian Particle Accelerator Conference*, Tsukuba (KEK, Tsukuba, Ibaraki, Japan), p. 432.
- Gupta, R. C., J. I. M. Botman, and M. K. Craddock, 1985, *IEEE Trans. Nucl. Sci.* **NS-32**, 2308.
- Halbach, K., 1998, in *Handbook of Accelerator Physics and Engineering: A Compilation of Formulae and Data*, edited by A. Chao and M. Tigner (World Scientific, Singapore), p. 445.
- Hardt, W., and D. Möhl, 1969, CERN ISR-300/GS/69-16.
- He, P., H. C. Hseuh, M. Mapes, R. Todd, D. Weiss, and D. Wilson, 2003, unpublished.
- Henderson, S., 1998, in *Handbook of Accelerator Physics and Engineering: A Compilation of Formulae and Data*, edited by A. Chao and M. Tigner (World Scientific, Singapore), p. 396.
- Hereward, H., 1971, CERN Report 71-15.
- Hershcovitch, A., 1995, *J. Appl. Phys.* **78**, 5283.
- Hirata, K., J. M. Jowett, W. Chou, S. Ivanov, H. Mais, J. Wei, D. H. Whittum, and C. Zhang, 2000, Eds., *ICFA Beam Dynamics Newsletter* **21**.
- Hiskes, J. R., A. Karo, and M. Gardner, 1976, *J. Appl. Phys.* **47**, 3888.
- Hofmann, A., and S. Myers, 1980, in *Proceedings of the 11th International Conference on High Energy Accelerators*, Geneva, edited by W. S. Newman (Birkhäuser, Basel), p. 610.
- Hofmann, I., 1985, *Laser Part. Beams* **3**, 1.
- Hofmann, I., 1998, *Phys. Rev. E* **57**, 4713.
- Hofmann, I., and O. Boine-Frankenheim, 1999, in *Workshop on Instabilities of High-Intensity Hadron Beams in Rings*, AIP Conf. Proc. No. 496, edited by T. Roser and S. Y. Zhang (AIP, Melville, NY), p. 85.
- Holmes, J. A., J. D. Galambos, D. Jeon, V. Danilov, and D. K. Olsen, 1999, *Phys. Rev. ST Accel. Beams* **2**, 114202.
- Iliev, A., and R. Servranckx, 1993, TRIUMF Report TRI-DN-93-K229.
- IPNS, 1995, *The IPNS Upgrade* (Argonne National Laboratory, Argonne, IL).
- Izawa, M., Y. Sato, and T. Toyomasu, 1995, *Phys. Rev. Lett.* **74**, 5044.
- Jason, A. J., B. Blind, P. J. Channell, and T.-S. F. Wang, 1994, in *Proceedings of the 4th Particle Accelerator Conference*, London, edited by V. P. Suller and Ch. Petit-Jean Genaz (World Scientific, Singapore), p. 1219.
- Jimenez, J. M., 2001, CERN Report CERN-SL-2001-003-DI.
- Johnsen, K., 1956, in *CERN Symposium on High-Energy Accelerators*, Geneva, edited by E. Regenstreif (CERN, Geneva), Vol. 1, p. 106.
- Jones, F. W., G. H. Mackenzie, and H. Schönauer, 1990, *Part. Accel.* **31**, 199.
- J-PARC (Japan Atomic Energy Research Institute, JAERI, and High Energy Accelerator Research Organization, KEK), 2002, *Accelerator Technical Design Report for High-Intensity Proton Accelerator Facility Project*.
- Kaltchev, D. I., M. K. Craddock, R. V. Servranckx, and J. B. Jeanneret, 1997, in *Proceedings of the 1997 Particle Accelerator Conference*, Vancouver, B. C., edited by M. Comyn, M. K. Craddock, M. Reiser, and J. Thomson (IEEE, Piscataway, NJ), p. 153.
- KAON, 1990, *Kaon Factory Study, Accelerator Design Report* (TRIUMF, Vancouver).
- Kapchinskii, I. M., and V. A. Teplyakov, 1970, *Prib. Tekh. Eksp.* **119**, 19.
- Keil, E., and W. Schnell, 1969, CERN Report TH-RF/69-48.
- Keil, E., and B. Zotter, 1971, CERN Report CERN-ISR-TH-71-58.

- Kersevan, R., 2002, in *Proceedings of European Particle Accelerator Conference*, Paris, edited by T. Garvey *et al.* (EPS-IGA and CERN, Geneva), p. 2565.
- Kerst, D. W., *et al.*, 1955, *Phys. Rev.* **98**, 1153A.
- Khoe, T. L., *et al.*, 1975, *Part. Accel.* **6**, 213.
- Kinsho, M., D. Nishizawa, Y. Saito, H. Suzuki, and H. Yokomizo, 2002, *J. Vac. Sci. Technol. A* **20**, 829.
- Koba, D. W., *et al.*, 1999, *Rev. Sci. Instrum.* **79**, 2988.
- Kolomensky, A. A., V. A. Petukhov, and M. S. Rabinovich, 1957, *J. Exp. Theor. Phys.* **33**, 298.
- Koscielniak, S., 1999, in *Workshop on Instabilities of High-Intensity Hadron Beams in Rings*, AIP Conf. Proc. No. 496, edited by T. Roser and S. Y. Zhang (AIP, Melville, NY), p. 391.
- Landau, L. D., 1946, *J. Phys. (USSR)* **10**, 25.
- Laslett, L. J., 1963, Brookhaven National Laboratory Report 7534, p. 324.
- Laslett, L. J., V. K. Neil, and A. M. Sessler, 1961, *Rev. Sci. Instrum.* **32**, 276.
- Laslett, L. J., A. M. Sessler, and D. Möhl, 1974, *Nucl. Instrum. Methods* **121**, 517.
- Lee, S. Y., and J. Wei, 1988, in *Proceedings of the 1st European Particle Accelerator Conference*, Rome, edited by S. Tazzari (World Scientific, Singapore), p. 764.
- Lee, W. W., and L. C. Teng, 1971, *IEEE Trans. Nucl. Sci.* **NS-18**, 1057.
- Lee, Y. Y., 1998, *J. Korean Phys. Soc.* **8**, 16.
- Lee, Y. Y., 2002, private communication.
- Leung, K. N., 1998, in *Handbook of Accelerator Physics and Engineering: A Compilation of Formulae and Data*, edited by A. Chao and M. Tigner (World Scientific, Singapore), p. 428.
- LHC, 1995, *The LHC Conceptual Design Report CERN/AC/95-05(LHC)* (CERN, Geneva).
- Liaw, C. J., Y. Y. Lee, and J. Tuozzolo, 2001, in *Proceedings of the 2001 Particle Accelerator Conference*, Chicago, edited by P. Lucas and S. Webber (IEEE, Piscataway, NJ), 1538.
- Livingston, M. S., and J. P. Blewett, 1962, *Particle Accelerators* (McGraw-Hill, New York).
- Loulergue, A., A. Mosnier, and J. Payet, 2001, private communication.
- Ludwig, H., N. Catalan-Lasheras, N. Simos, J. Walker, A. Mallen, J. Wei, and M. Todosow, 2000, in *Proceedings of the 7th European Particle Accelerator Conference*, Vienna, edited by J.-L. Laclare *et al.* (Austrian Academy of Science Press, Vienna), p. 2438.
- Ludwig, H., N. Simos, J. Walker, P. Thieberger, A. Aronson, and J. Wei, 1999, in *Proceedings of the 1999 Particle Accelerator Conference*, New York, edited by A. Luccio and W. MacKay (IEEE, Piscataway, NJ), Vol. 1, p. 548.
- Macek, R., 1999, in *Workshop on Two-Stream Instabilities in Accelerators and Storage Ring*, Santa Fe, edited by K. Hackay and R. Macek, www.aps.anl.gov/conferences/icfa/two-stream.html
- Macek, R., *et al.*, 2001, in *Proceedings of the 2001 Particle Accelerator Conference*, Chicago, edited by P. Lucas and S. Webber (IEEE, Piscataway, NJ), p. 688.
- Machida, S., 1991, *Nucl. Instrum. Methods Phys. Res. A* **309**, 43.
- Machida, S., 1999, private communication.
- Makino, K., and M. Berz, 1999, *Nucl. Instrum. Methods Phys. Res. A* **427**, 338.
- Malitsky, N., *et al.*, 1999, in *Proceedings of the 1999 Particle Accelerator Conference*, New York, edited by A. Luccio and W. MacKay (IEEE, Piscataway, NJ), Vol. 4, p. 2713.
- Martini, M., 1984, CERN PS/84-9 (AA).
- Maslov, M. A., N. V. Mokhov, and I. A. Yazynin, 1991, *Superconducting Super Collider Laboratory, Report SSCL-484*.
- McMillan, E. M., 1945, *Phys. Rev. Lett.* **68**, 1434.
- MCNP, Web site: <http://epicws.epm.ornl.gov/rsic.html> (Radiation Safety Information Computational Center, Oak Ridge National Laboratory, USA).
- Mètral, E., R. Cappi, M. Giovannozzi, G. Mètral, and F. Zimmermann, 2001, in *Proceedings of the 2001 Particle Accelerator Conference*, Chicago, edited by P. Lucas and S. Webber (IEEE, Piscataway, NJ), p. 682.
- Mills, F. E., 1998, in *Handbook of Accelerator Physics and Engineering: A Compilation of Formulae and Data*, edited by A. Chao and M. Tigner (World Scientific, Singapore), p. 439.
- Mokhov, N. V., 1995, *The MARS Code System User's Guide* FNAL Report FN-628, Web site: <http://www-ap.fnal.gov/MARS> (FNAL, Batavia, IL).
- Mokhov, N. V., and W. Chou, 1999, Eds., *Workshop on Beam Halo and Scraping*, Lake Como, Wisconsin (FNAL, Batavia, IL).
- Mori, H., *et al.*, 1998, in *Proceedings of the 6th European Particle Accelerator Conference*, Stockholm, edited by S. Myers and J. Poole (Institute of Physics, Bristol), p. 301.
- MURA (Midwest University Research Association), 1964, *Rev. Sci. Instrum.* **35**, 1393.
- Nassibian, G., and F. Sacherer, 1979, *Nucl. Instrum. Methods* **159**, 21.
- Neil, V. K., and A. M. Sessler, 1965, *Rev. Sci. Instrum.* **36**, 429.
- Neuffer, D., 1992, *Nucl. Instrum. Methods Phys. Res. A* **321**, 1.
- Ng, K. Y., D. Wildman, M. Popovic, A. Browman, D. Fitzgerald, R. Macek, M. Plum, and T. Spickermann, 2001, in *Proceedings of the 2001 Particle Accelerator Conference*, Chicago, edited by P. Lucas and S. Webber (IEEE, Piscataway, NJ), p. 2890.
- Ng, K. Y., and B. Zotter, 2001, in *Proceedings of the 2001 Particle Accelerator Conference*, Chicago, edited by P. Lucas and S. Webber (IEEE, Piscataway, NJ), p. 2887.
- Nielson, C. E., A. M. Sessler, and K. R. Symon, 1959, in *Proceedings of the International Conference on High-Energy Accelerators and Instruments*, Geneva, edited by L. Kowarski (CERN, Geneva), p. 239.
- Ohkawa, T., 1958, *Rev. Sci. Instrum.* **29**, 108.
- Ohmi, K., 1995, *Phys. Rev. Lett.* **75**, 1526.
- Ohmi, K., *et al.*, 2001, in *Proceedings of the International Conference on High Energy Accelerators*, Tsukuba (KEK, Tsukuba, Ibaraki, Japan).
- Ohmi, K., and F. Zimmermann, 2001, *Phys. Rev. Lett.* **85**, 3821.
- Ohmi, K., F. Zimmermann, and E. Perevedentsev, 2002, *Phys. Rev. E* **65**, 016502.
- Ohmori, C., *et al.*, 1999, in *Proceedings of the 1999 Particle Accelerator Conference*, New York, edited by A. Luccio and W. MacKay (IEEE, Piscataway, NJ), Vol. 1, p. 413.
- Oliphant, M. L., 1943, Classified memo submitted to the British Directorate of Atomic Energy (University of Birmingham Archive, UK).
- Oliphant, M. L., J. S. Gooden, and G. S. Hide, 1947, *Proc. Phys. Soc. London* **59**, 666.
- OPERA (Vector Fields, Ltd, Oxford England).
- Papaphilippou, Y., 2001, in *Proceedings of the 2001 Particle Accelerator Conference*, Chicago, edited by P. Lucas and S. Webber (IEEE, Piscataway, NJ), p. 462.

- Papaphilippou, Y., and D. T. Abell, 2000, in *Proceedings of the 7th European Particle Accelerator Conference*, Vienna, edited by J.-L. Laclare *et al.* (Austrian Academy of Science Press, Vienna), p. 1453.
- Papaphilippou, Y., Y. Y. Lee, and W. Meng, 2001, in *Proceedings of the 2001 Particle Accelerator Conference*, Chicago, edited by P. Lucas and S. Webber (IEEE, Piscataway, NJ), p. 1667.
- Papaphilippou, Y., J. Wei, and R. Talman, 2003, *Phys. Rev. E* **67**, 046502.
- Parzen, G., 1987, *Nucl. Instrum. Methods Phys. Res. A* **256**, 231.
- Pedersen, F., 1975, *IEEE Trans. Nucl. Sci.* **NS-22**, 1906.
- Peggs, S., 1983, *IEEE Trans. Nucl. Sci.* **NS-30**, 2460.
- Peggs, S., J. Cardona, J. M. Brennan, J. Kewisch, G. McIntyre, N. Tsoupas, M. Schillo, A. Todd, B. Ludewig, and N. Lockyer, 2001, in *Proceedings of the 2001 Particle Accelerator Conference*, Chicago, edited by P. Lucas and S. Webber (IEEE, Piscataway, NJ), p. 2482.
- Peggs, S., S. Tepikian, and D. Trbojevic, 1993, in *Proceedings of the 1993 Particle Accelerator Conference*, Washington, D.C., edited by the IEEE staff (IEEE, New York), p. 168.
- Piwinski, A., 1977, *IEEE Trans. Nucl. Sci.* **NS-24**, 1364.
- Pivi, M., 2002, CERN Report CERN-2002-001.
- Piwinski, A., 1984, in *Proceedings of the CERN Accelerator School*, Gif-sur-Yvette, edited by S. Turner (CERN, Geneva), p. 226.
- Plum, M. A., 1995, in *Proceedings of the 1995 Particle Accelerator Conference*, Dallas, TX, edited by the IEEE staff (IEEE, New York), p. 3403.
- Plum, M. A., *et al.*, 1999, *Phys. Rev. ST Accel. Beams* **2**, 064201.
- Prelec, K., 1989, in *Proceedings of the 1989 IEEE Particle Accelerator Conference: Accelerator Science and Technology*, Chicago, edited by F. Bennett and J. Kopta (IEEE, New York), Vol. 1, p. 340.
- Prior, C. R., and G. Rees, 1998, *Nucl. Instrum. Methods Phys. Res. A* **415**, 357.
- Proch, D., 1998, in *Handbook of Accelerator Physics and Engineering: A Compilation of Formulae and Data*, edited by A. Chao and M. Tigner (World Scientific, Singapore), p. 526.
- Raparia, D., J. Alessi, Y. Y. Lee, and W. T. Weng, 1998, Brookhaven National Laboratory, Technical note SNS/52.
- Raparia, D., and A. Hershcovitch 2002, Brookhaven National Laboratory, Technical note SNS/108.
- Raubenheimer, T. O., and F. Zimmerman, 1995, *Phys. Rev. E* **52**, 5487.
- Rees, G., 1994, in *Proceedings of the 4th European Particle Accelerator Conference*, London, edited by V. P. Suller and Ch. Petit-Jean Genaz (World Scientific, Singapore), p. 241.
- Rees, G., 1998, in *Handbook of Accelerator Physics and Engineering: A Compilation of Formulae and Data*, edited by A. Chao and M. Tigner (World Scientific, Singapore), p. 497.
- Rice, D., 1998, in *Handbook of Accelerator Physics and Engineering: A Compilation of Formulae and Data*, edited by A. Chao and M. Tigner (World Scientific, Singapore), p. 263.
- Risselada, T., 1990, CERN PS/90-15.
- Rose, M. E., 1938, *Phys. Rev.* **53**, 715.
- Rosenberg, S., and K. Harkay, 2000, *Nucl. Instrum. Methods Phys. Res. A* **453**, 507.
- Roser, T., 1995, in *Proceedings of the 1995 Particle Accelerator Conference*, Dallas, TX, edited by the IEEE staff (IEEE, New York), p. 3154.
- Roser, T., 2001, in *Proceedings of the 2001 Particle Accelerator Conference*, Chicago, edited by P. Lucas and S. Webber (IEEE, Piscataway, NJ), p. 714.
- Ruggiero, F., G. Rumolo, and F. Zimmermann, 2001, *Phys. Rev. ST Accel. Beams* **4**, 012801; **4**, 029901(E).
- Ruggiero, A. G., and V. G. Vaccaro, 1968, CERN Report ISR-TH/68-33.
- Rumolo, G., I. Hofmann, G. Miano, and U. Oeftiger, 1998, *Nucl. Instrum. Methods Phys. Res. A* **415**, 411.
- Sacherer, F., 1968, Lawrence Radiation Laboratory Report UCRL-18454 (Ph.D. thesis, University of California at Berkeley).
- Sacherer, F., 1977, CERN Report 77-13, p. 198.
- Sasaki, H., 1987, in *International Workshop on Hadron Facility Technology*, Santa Fe, Los Alamos National Laboratory, Report No. LA-11310-C, Los Alamos, NM.
- Schachinger, L., and R. Talman, 1987, *Part. Accel.* **22**, 35.
- Schindl, K., 1979, *IEEE Trans. Nucl. Sci.* **NS-26**, 3562.
- Schoch, A., 1958, CERN Report CERN 57-23.
- Seiler, H., 1983, *J. Appl. Phys.* **54**, R1.
- Servranckx, Y., *et al.* 1989, in *Proceedings of the 1989 IEEE Particle Accelerator Conference: Accelerator Science and Technology*, Chicago, edited by F. Bennett and J. Kopta (IEEE, New York), Vol. 2, p. 1355.
- Sessler, A. M., and V. G. Vaccaro, 1967, CERN Report ISR-RF/67-2.
- Shaw, S., R. I. Cutler, A. D. Herr, Y. Y. Lee, C. J. Liaw, and C. S. Feigerle, 2003, in *Proceedings of the 2003 IEEE Particle Accelerator Conference*, Chicago (IEEE, Piscataway, NJ, in press).
- Shou, J., 1980, *Phys. Rev. B* **27**, 2141.
- Simos, N., N. Catalan-Lasheras, S. Crivello, and H. Ludewig, 2001, in *Proceedings of the 2001 Particle Accelerator Conference*, Chicago, edited by P. Lucas and S. Webber (IEEE, Piscataway, NJ), p. 1405.
- Sluyters, T. J., 1990, in *Proceedings of the 14th International Conference on High-Energy Accelerators*, Tsukuba (Science Council of Japan Phys. Soc./IUPAP, UK); [Part Accel. **26**, 247].
- Smith, L., 1963, in *Proceedings of the International Conference on High-Energy Accelerators*, Dubna, Russia, p. 1232.
- Sørenssen, A., 1967, in *Proceedings of the 6th International Conference on High-Energy Accelerators*, Cambridge, MA, edited by R. A. Mack (MIT and Harvard University, Cambridge, MA), p. 474.
- Sørenssen, A., 1975, *Part. Accel.* **6**, 141.
- Suzuki, Y., 1999, in *Workshop on Injection and Extraction*, Abingdon, unpublished.
- Symon, K. R., 1955, *Phys. Rev.* **98**, 1152A.
- Tabata, T., R. Ito, and S. Okabe, 1971, *Nucl. Instrum. Methods* **94**, 509.
- Takayama, K., 1984, *Part. Accel.* **14**, 201.
- Takayama, K., and J. Kishiro, 2000, *Nucl. Instrum. Methods Phys. Res. A* **451**, 304.
- Teng, L. C., 1969, FNAL Report FN-196/0400.
- Teng, L. C., 1972, *Part. Accel.* **4**, 81.
- Thieberger, P., A. L. Hanson, D. B. Steski, V. Zajic, S. Y. Zhang, and H. Ludewig, 1999, *Phys. Rev. A* **61**, 042901.
- Trenkler, L. C., 1992, CERN Report SL/92-50 (EA).
- Trbojevic, D., D. Finley, R. Gerig, and S. Holmes, 1990, in *Proceedings of the European Particle Accelerator Conference*, Nice, France, edited by P. Marin and P. Mandrillon (Editions Frontières, Gif-sur-Yvette, France), p. 1536.

- Tsoupas, N., M. Blaskiewicz, Y. Y. Lee, J. Mi, A. Soukas, J. G. Wang, J. Wei, and S. Y. Zhang, 2000, in *Proceedings of the 7th European Particle Accelerator Conference*, Vienna, edited by J.-L. Laclare *et al.* (Austrian Academy of Science Press, Vienna), p. 2270.
- Tsoupas, N., C. Gardner, Y. Y. Lee, Y. Papaphilippou, and J. Wei, 2000, in *Proceedings of the 7th European Particle Accelerator Conference*, Vienna, edited by J.-L. Laclare *et al.* (Austrian Academy of Science Press, Vienna), p. 1581.
- Veksler, V., 1945, *J. Phys. (USSR)* **9**, 153.
- Wait, G. D., 1997, in *Proceedings of the 1997 Particle Accelerator Conference*, Vancouver, B.C., edited by M. Comyn, M. K. Craddock, M. Reiser, and J. Thomson (IEEE, Piscataway, NJ), Vol. 1, p. 1328.
- Walstrom, P. L., and E. G. Cook, 2001, in *Proceedings of the 2001 Particle Accelerator Conference*, Chicago, edited by P. Lucas and S. Webber (IEEE, Piscataway, NJ), p. 3735.
- Wan, W., 1999, in *Proceedings of the 1999 Particle Accelerator Conference*, New York, edited by A. Luccio and W. MacKay (IEEE, Piscataway, NJ), Vol. 1, p. 395.
- Wanderer, P., J. Jackson, A. Jain, Y. Y. Lee, W. Meng, I. Papaphilippou, C. Spataro, S. Tepikian, N. Tsoupas, and J. Wei, 2002, in *Proceedings of the 8th European Particle Accelerator Conference*, Paris, edited by T. Garvel *et al.* (EPS-IGA/CERN, Geneva, 2002), p. 1317.
- Wang, J. G., and S. Y. Zhang, 2000, in *Proceedings of the 7th European Particle Accelerator Conference*, Vienna, edited by J.-L. Laclare *et al.* (Austrian Academy of Science Press, Vienna), p. 972.
- Wang, J. M., and C. Pellegrini, 1980, in *Proceedings of the 11th International Conference on High-Energy Accelerators*, Geneva, edited by W. S. Newman (Birkhäuser Verlag, Basel), p. 554.
- Wang, L. F., H. Fukuma, K. Ohmi, and Y. Suetsugu, 2001, in *Proceedings of the 2001 Particle Accelerator Conference*, Chicago, edited by P. Lucas and S. Webber (IEEE, Piscataway, NJ), Vol. 1, p. 701.
- Wang, T. S., P. J. Channell, R. Macek, and R. C. Davidson, 2001, in *Proceedings of the 2001 Particle Accelerator Conference*, Chicago, edited by P. Lucas and S. Webber (IEEE, Piscataway, NJ), Vol. 1, p. 704.
- Wangler, T. P., 1998, *Principles of RF Linear Accelerators* (Wiley, New York).
- Warsop, C. M., 1998, in *Workshop on Space Charge Physics in High Intensity Hadron Rings*, AIP Conf. Proc. No. 448, edited by A. U. Luccio and W. T. Weng (AIP, Melville, NY), p. 104.
- Wei, J., 1990, *Longitudinal Dynamics of the Non-Adiabatic Regime in the Alternating-Gradient Synchrotrons*, Ph.D. dissertation, revised 1994 (SUNY, Stony Brook).
- Wei, J., 1992, in *Proceedings of the 3rd European Particle Accelerator Conference*, Berlin, edited by H. Henke, Ch. Petit-Jean Genaz, and Homeyer (Éditions Frontières, Gif-sur-Yvette, France), Vol. 1, p. 833.
- Wei, J., 1998, in *Handbook of Accelerator Physics and Engineering: A Compilation of Formulae and Data*, edited by A. Chao and M. Tigner (World Scientific, Singapore), p. 281.
- Wei, J., 1999, in *Workshop on Instabilities of High-Intensity Hadron Beams in Rings*, AIP Conf. Proc. No. 496, edited by T. Roser and S. Y. Zhang (AIP, Melville, NY), p. 197.
- Wei, J., D. T. Abell, *et al.*, 2000, *Phys. Rev. ST Accel. Beams* **3**, 080101.
- Wei, J., J. Beebe-Wang, *et al.*, 2000, in *Proceedings of the 7th European Particle Accelerator Conference*, Vienna, edited by J.-L. Laclare *et al.* (Austrian Academy of Science Press, Vienna), p. 981.
- Wei, J., J. Beebe-Wang, *et al.*, 2001, in *Proceedings of the 2001 Particle Accelerator Conference*, Chicago, edited by P. Lucas and S. Webber (IEEE, Piscataway, NJ), Vol. 4, p. 2560.
- Wei, J., J. M. Brennan, *et al.*, 1995, in *Proceedings of the 1995 Particle Accelerator Conference*, Dallas, TX, edited by the IEEE staff (IEEE, New York), Vol. 5, p. 3334.
- Wei, J., A. V. Fedotov, and Y. Papaphilippou, 2001, *Physics and Design of High-Intensity Circular Accelerators*, Lectures at the 2001 U.S. Particle Accelerator School, unpublished.
- Wei, J., and M. Harrison, 1992, in *Proceedings of the XVth International Conference on High-Energy Accelerators*, Hamburg, edited by J. Rossbach (World Scientific, Singapore), p. 1031.
- Wei, J., and R. Macek, 2002, CERN Report CERN-2002-001.
- Wei, J., and R. Talman, 1996, *Part. Accel.* **55**, 339.
- Weiland, T., 1998, in *Handbook of Accelerator Physics and Engineering: A Compilation of Formulae and Data*, edited by A. Chao and M. Tigner (World Scientific, Singapore), p. 199.
- Weng, W., 1990, in *Proceedings of the 14th International Conference on High-Energy Accelerators*, Tsukuba (Science Council of Japan Phys. Soc./IUPAP, UK); also published in *Part. Accel.* **26**, 259.
- Weng, W., 1997, in *Proceedings of the 1997 Particle Accelerator Conference*, Vancouver, B. C., edited by M. Comyn, M. K. Craddock, M. Reiser, and J. Thomson (IEEE, Piscataway, NJ), Vol. 1, p. 42.
- Wilson, P., 1974, in *Proceedings of the IXth International Conference on High-Energy Particle Accelerators*, SLAC, edited by R. B. Neal (SLAC, Stanford, CA), p. 57.
- Witcover, R. L., P. R. Cameron, T. J. Shea, R. C. Connolly, and M. Kesselman, 1999, in *Proceedings of the 1999 Particle Accelerator Conference*, edited by A. Luccio and W. MacKay (IEEE, Piscataway, NJ), Vol. 3, p. 2250.
- Woody, K., J. A. Holmes, V. Danilov, and J. D. Galambos, 2001, in *Proceedings of the 2001 Particle Accelerator Conference*, Chicago, edited by P. Lucas and S. Webber (IEEE, Piscataway, NJ), Vol. 3, p. 2057.
- Yamane, I., 1998, *Phys. Rev. ST Accel. Beams* **1**, 053501.
- Zeller, A., 1998, in *Handbook of Accelerator Physics and Engineering: A Compilation of Formulae and Data*, edited by A. Chao and M. Tigner (World Scientific, Singapore), p. 456.
- Zenkevich, P. R., and D. G. Koshkarev, 1972, *Part. Accel.* **3**, 1.
- Zhang, S. Y., 2002, private communication.
- Zimmermann, R., 1997, LHC Project-Report 95, and SLAC-PUB-7425.
- Zimmermann, R., 2001, in *Proceedings of the 2001 Particle Accelerator Conference*, Chicago, edited by P. Lucas and S. Webber (IEEE, Piscataway, NJ), Vol. 1, p. 666.
- Zotter, B., 1999, in *Workshop on Two-Stream Instabilities in Accelerators and Storage Rings*, Santa Fe, edited by K. Harkay and R. Macek, www.aps.anl.gov/conferences/icfa/two-stream.html
- Zotter, B., and S. Kheifets, 1998, *Impedances and Wakes in High-Energy Particle Accelerators* (World Scientific, Singapore).